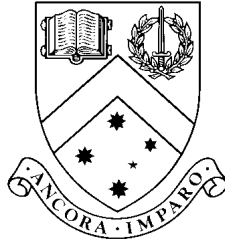


Solar Oscillations in Magnetic Regions



A thesis submitted for the degree of:

Doctor of Philosophy

by

Christoper Smedley Hanson

BSc (Hons),

Supervisor: Prof. Paul S. Cally

Associate Supervisor: Dr. Alina C. Donea

Monash Centre for Astrophysics

School of Mathematical Sciences

Monash University, Australia

October, 2014

Copyright Notices

Notice 1

Under the Copyright Act 1968, this thesis must be used only under the normal conditions of scholarly fair dealing. In particular no results or conclusions should be extracted from it, nor should it be copied or closely paraphrased in whole or in part without the written consent of the author. Proper written acknowledgement should be made for any assistance obtained from this thesis.

Notice 2

I certify that I have made all reasonable efforts to secure copyright permissions for third-party content included in this thesis and have not knowingly added copyright content to my work without the owner's permission.

Contents

1	Introduction	1
1.1	Helioseismology	2
1.2	Magneto-seismology of Active Regions	4
1.3	Wave Propagation In Solar Atmospheres	6
1.4	An Analytical Approach to thin flux tube interactions	8
1.4.1	Unstratified Media	8
1.4.2	Stratified Media	10
1.5	Morphology of Acoustic Power Halos	14
1.5.1	Seismic Emission within Acoustic Power Halos	14
1.5.2	Computational Helioseismic Holography	15
1.6	Basis for this Research	19
2	An Analytical Approach to the Scattering Between Two Thin Magnetic Flux Tubes in a Stratified Atmosphere	25
2.1	Introduction	26
2.2	Mathematical Formalism	28
2.2.1	Wave propagation in the Polytrope	28
2.2.2	Thin Flux Tubes	30
2.2.3	Tube Oscillations	31
2.2.4	The Scattered Wave Field	31
2.2.5	The Interaction Between flux tubes through the Scattered Wave Field	34
2.3	The Importance of the Coordinate Origin	38
2.4	Results	41
2.5	Discussion and Conclusions	45
3	The Scattering of Acoustic Waves from Ensembles of Thin Magnetic Flux Tubes	51
3.1	Introduction	52
3.2	Ensemble Scattering Formalism	53
3.2.1	The Interaction of Higher Order m Modes within Ensembles	54
3.3	Results	55

3.3.1	Symmetry Studies	55
3.3.2	Random Ensembles	58
3.3.3	Case Study: Magnetic Flux	64
3.4	Discussion and conclusions	65
4	Using SDO Data to Examine the Seismic Emissions Surrounding Complex Active Regions	73
4.1	Instrumentation: SDO	74
4.2	Data Processing	76
4.2.1	Data Selection	76
4.2.2	Data Reduction	77
4.2.3	The Use of SHARPs and Full-disk Vector Magnetograms	78
4.2.4	Mapping of the Magnetic Field Vectors	79
4.2.5	Statistical Precautions	81
4.3	Results	83
4.3.1	Active Region Enhanced Power Morphology	84
4.3.2	Correlations Magnetic Fields and Acoustic Power Halos	97
4.3.3	Seismic Glories	105
4.3.4	The Seismic Plateau	106
4.3.5	Spatial Correlations: Seismic versus Local Acoustic Power	109
4.4	Discussion and Conclusions	110
5	Summary and Future Prospects	117
5.1	The Behaviour of Flux Tube Bundles	118
5.2	Enhanced Seismic Sources	120
A	Statistical Precautions	123
B	Power as a Function of B and γ	127
C	Seismic and Local Acoustic Power maps at all Frequencies	133
6	Bibliography	137

Acknowledgements

First and foremost, I extend my thanks to my supervisors Paul Cally and Alina Donea, who have supported, encouraged and guided me from day one. It has been a privilege to work with such passionate professionals in the field, without whom Solar physics in Australia would not exist.

I extend my thanks to a number of people both inside and outside of Monash who I've had the privilege of working with and learning from. Hamed Moradi, who is always an encouragement in keeping a level head; Charles Lindsey, without whom Helioseismic Holography would be a difficult concept to understand; K.D Leka, whose insights and knowledge have greatly helped in understanding the technical aspects of observational data.

Finally, I dedicate this work to my loving and supportive wife Natalie and our beautiful daughter Morgan who have provided love, support and encouragement throughout these past few years.

Abstract

In the 50 years of helioseismology, we have gained an extensive understanding into the physical processes present within our sun. With the aid of high resolution observations and increased computational power, the current body of understanding is rapidly growing. However, there are still many questions left answered today. In this thesis, we will address two phenomena in order to shed light on their related open questions. In the first part, we will examine the scattering regimes that exist within bundles of thin magnetic flux tubes. In particular, we will address the question of how magnetic plage can absorb large amounts of wave energy and whether the resultant scattered wave field can be used to infer the magnetic field structure. The second phenomenon concerns the seismic sources that are situated within acoustic power halos and what role of the magnetic field has in enhancing these sources.

In addressing the multiple scattering regime, a semi-analytical model was developed in order to model the scattering between numerous thin flux tubes situated within a stratified atmosphere. We have used a method originally designed for oceanic wave scattering, and applied it to a solar context. While to some extent this has been done in the past, we further develop the model to include the scattering of all possible modes between thin magnetic flux tubes. In doing so, we outline and address a mathematical error in the original formalism, that was not apparent until previous results were compared to recent numerical studies. Numerous case studies are then examined, ranging from the simple case of two interacting tubes, to large numbers of closely packed tubes. Various parameters are explored and the effect these have on the scattering regime is reported. Our results compare quite well with numerical and observational studies, and this model presents a significant step forward in understanding how the scattered wave field can be used to infer the internal constitution of a slender magnetic field structure.

On addressing the second phenomenon, we employ the helioseismic holog-

raphy technique to examine the enhanced seismic sources that are situated within the acoustic power halo that surrounds complex active regions. We examine three active regions using SDO data and apply strict statistical precautions in our analysis. The relationship between the seismic sources and the magnetic field is explored, with a strong correlation found between seismic enhancement and quasi-horizontal fields of intermediate strength. Additionally, the most intense seismic emitters (acoustic glories) were found to be located within fields very close to horizontal. The relationship between the seismic source halos and the commonly used local acoustic power maps is also explored, with large similarities reported. We found that the greatest difference between the two types of halos occurs within the high frequency (9 mHz) regime. The results of this observational study agree with other recent studies, however this study presents a significant advancement on previous holography studies.

PART A: General Declaration

Monash University

Declaration for thesis based or partially based on conjointly published or unpublished work

General Declaration

In accordance with Monash University Doctorate Regulation 17.2 Doctor of Philosophy and Research Master's regulations the following declarations are made:

I hereby declare that this thesis contains no material which has been accepted for the award of any other degree or diploma at any university or equivalent institution and that, to the best of my knowledge and belief, this thesis contains no material previously published or written by another person, except where due reference is made in the text of the thesis.

This thesis includes 3 original papers published in peer reviewed journals and 1 unpublished publications. The core theme of the thesis is Solar Magneto-seismology. The ideas, development and writing up of all the papers in the thesis were the principal responsibility of myself, the candidate, working within the School of Mathematical Sciences under the supervision of Prof. Paul S. Cally and Dr. Alina C. Donea.

The inclusion of co-authors reflects the fact that the work came from active collaboration between researchers and acknowledges input into team-based research.

In the case of chapters 2-4 my contribution to the work involved the following:

Thesis chapter	Publication title	Publication status	Nature and extent of candidate's contribution
2	An Analytical Approach to Scattering between Two Thin Magnetic Flux Tubes in a Stratified Atmosphere	Published, 2014 ApJ, 781, 125H	Key ideas, development of code, modelling, produced all results, writing of the paper.
3	The Scattering of f- and p-modes from Ensembles of Thin Magnetic Flux Tubes: An Analytical Approach	Published, 2014 ApJ, 791, 129H	Key ideas, development of code, modelling, produced all results, writing of the paper.
4	Enhanced sources of Acoustic power Surrounding AR 11429	Published, 2013 JPhC, 440a, 2028D	Results, produced some figures, contributed to discussion
4	The Morphology of Power Halos Surrounding the Complex Active Region AR11429	In Preparation	Key ideas, analysis, development of codes, results, data reduction, writing of entire paper.

I have renumbered sections of submitted or published papers in order to generate a consistent presentation within the thesis.

Signed:



Date: 13/10/2014

Chapter 1

Introduction

This chapter has a dual purpose. Firstly, the current body of work concerning wave interactions within collections of thin flux tubes will be summarized. Concurrently, the gaps in this knowledge will be outlined with particular attention to the lack of thorough analytical models. Following this discussion, an outline of the phenomenon known as acoustic power halos will be given, with particular attention given to the findings of previous studies. Additionally, a review of helioseismic holography will be given, in order to understand the application of this technique in this study. I point out that this thesis has theoretical and observational aspects, related by the fact they both investigate the seismology around magnetic field concentrations.

This chapter begins with a general overview of the importance of helioseismology around active regions (section 1.1), with a particular focus on the magneto-seismology of active regions (section 1.2). Sections 1.3 and 1.4 will examine the current theoretical background to wave propagation and scattering within the sun. Section 1.5 will revise the current body of knowledge regarding the acoustic halos and the helioseismic holography tools used to examine such phenomena. Finally, the basis for this research will be outlined in the context of the previously stated background knowledge.

1.1 Helioseismology

The inability to directly observe the internal constitution of the sun requires the use of seismology techniques to probe its subsurface structures. The tools to achieve this fall under the field of Helioseismology and generally use observable surface oscillations generated by internally propagating waves to probe the subsurface. Helioseismology can be divided into two parts, global and local helioseismology. As the name suggests, global helioseismology concerns itself with the seismology of the entire sun. This field uses surface motion induced by global standing modes and the general normal mode theory of non-radial stellar oscillations (Unno et al. 1989), to infer the internal structure of the sun. While global analysis is useful for the study of large scale structures, the comparatively younger field of local helioseismology concerns itself with local perturbations of the solar surface. In particular, local studies are interested in the propagation of waves around surface magnetic features (e.g. sunspots) and the effect these features have on acoustic waves. This thesis is focused on the effect of magnetic fields on local oscillations, with the particulars outlined further in this chapter. A comprehensive outline of Local Helioseismology is given in Gizon and Birch (2005).

Solar acoustic waves are generated by turbulent convection (Goldreich and Keeley 1977) and then propagate, interfere and reflect within the solar interior. These waves are defined as either an acoustic (p -mode), fundamental (f -mode) or gravity wave (g -mode). The f -mode is a surface gravity mode that propagates horizontally across the solar surface, while p -modes are not confined to the surface and are considered acoustic due to pressure being the dominant restoring force. In contrast to acoustic waves, the restoring force of the g -mode is buoyancy, and it is therefore in the radiative core, or in the thin subadiabatic layer near the solar surface. We shall not consider g -modes further. The most well known manifestations are the 5-minute oscillations first observed by Leighton et al. (1962) and Evans and Michard (1962). Typically an acoustic mode generated at the surface will travel inward, experiencing an increase in sound speed. Due to this increase the wave will begin to refract, eventually reaching its turning point and returning to the surface creating further observable oscillations (see Figure 1.1). By mapping these waves across the solar surface, or some patches on it, and comparing them to theoretical models, the goal of understanding the subsurface of the sun can be addressed.

In terms of modelling the behaviour of these p -modes, the radial displacements (δr) are generally represented in terms of spherical harmonics (Y_l^m)

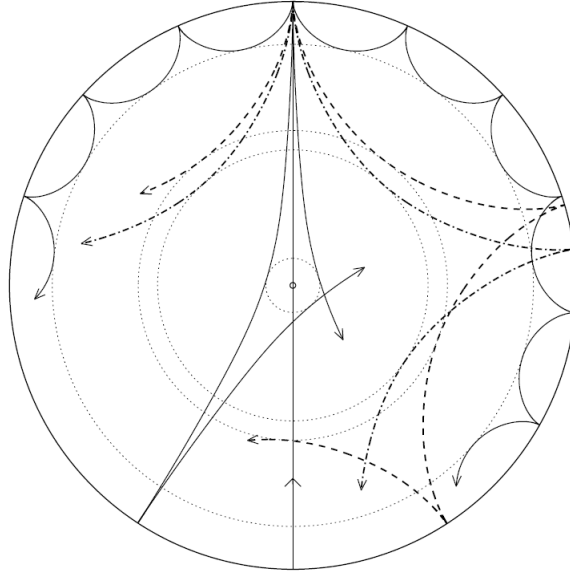


Figure 1.1: An illustration of the propagation of acoustic waves within the solar interior. Depending on the l of the spherical wave the modes may travel deeper before reaching the turning point (dotted line), refracting and returning towards the surface again. Image from Cristensen-Dalsgaard “Stellar Oscillations” Lecture Notes.

and radial order n ,

$$\delta r(r, \theta, \phi, t) = \sum_{n,l} \sum_{m=-l}^l a_{nlm} \xi_{nl}(r) Y_l^m(\theta, \phi) e^{i\omega_{nlm}t}, \quad (1.1)$$

where l is the spherical order and m is the azimuthal order. Here a_{nlm} is the complex amplitude of the acoustic wave with an angular frequency of ω_{nlm} . By taking a power spectrum of the surface oscillations, and averaging the m modes, discrete ridges that correspond to different n order waves will arise. An example of these ridges is seen in Figure 1.2 where the bottom ridge corresponds to the f -mode ($n = 0$) and all higher ridges correspond to p_n -modes of increasing order $n = 1, 2, 3, \dots$. Generally high ω and low l waves propagate deeper into the sun, with the turning point of these waves obtained through the simple ray-theory relation,

$$\frac{c_s^2(r_t)}{r_t^2} = \frac{\omega^2}{l(l+1)} \quad (1.2)$$

where r_t is the radial distance from the solar centre to the turning point and c_s is the sound speed. Typically acoustic modes are trapped between this turning point and a reflection point near the solar surface. However, Figure 1.2

shows that above ≈ 5.3 mHz the ridges that indicate the trapped modes are less defined. This frequency is known as the acoustic cut-off frequency (ν_{ac}), where modes greater than ν_{ac} propagate through the chromosphere to the base of the corona. Though the accepted value of ν_{ac} is 5.3 mHz, this value is only an approximation as the cut-off frequency is dependent on factors such as the solar cycle (e.g. Jiménez et al. 2011).

1.2 Magneto-seismology of Active Regions

If the sun were devoid of magnetic fields, then its physical processes could be understood through the application of classical hydrodynamics. However, the sun is a magnetic star with complex magnetic fields that influence the propagation of acoustic waves within the interior and atmosphere. These magnetic fields are generated through the solar dynamo process, whereby a combination of convection and differential rotation within the sun induces the electric currents needed to generate and sustain these fields (see Weiss and Tobias 2000; Tobias 2002). During the sun's 11 year cycle the magnetic fields are wound up, eventually erupting through the surface creating small and large scale magnetic features. The study of the propagation and creation of acoustic waves involved with the magnetic features present in the solar surface is known as *Solar Magneto-seismology*.

A rudimentary magnetic feature present in the solar surface is known as a magnetic pore. The inhibition of convection, due to magnetic fields within these pores, results in the appearance of a dark cool region on the solar surface. Pores can be viewed as a tightly packed group of magnetic flux tubes that emerge through the photosphere forming a small umbra region, of radius on the order of a few Mm (see Zwaan 1978). Upon emergence, these pores can coalesce into large-scale magnetic features, such as sunspots (McIntosh 1981, etc), for which vortex attraction has been suggested as the responsible mechanism (Kitiashvili et al. 2010).

A sunspot is a large magnetic feature of a single magnetic polarity. The magnetic nature of sunspots was first proposed by Hale (1908), who examined the Hydrogen alpha line ($H\alpha$) using the Zeeman effect to establish the presence of magnetic field lines. The magnetic fields create a surface structure consisting of two major parts, the umbra and penumbra. The umbral region contains a near vertical field with peak strengths between 2000-3700 G (see Solanki 2003). The light intensity of this region is around 25% of the surrounding region, with an effective temperature of 4500 K. However, the

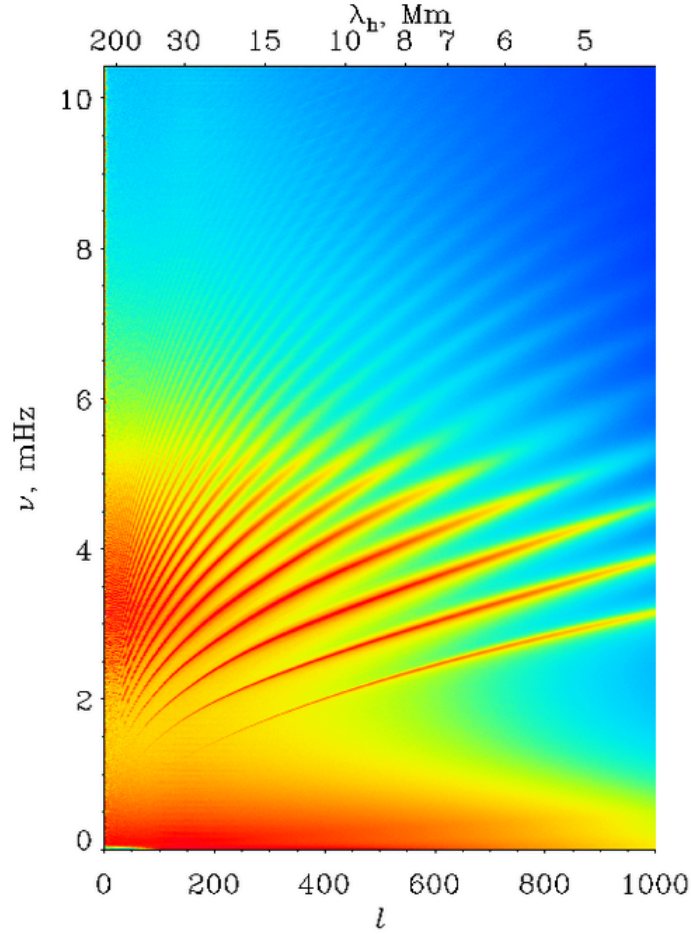


Figure 1.2: An l - ν diagram from MDI Dopplergrams. The image was produced by A. Kosovichev and is available on the <http://sun.stanford.edu/sasha/>. This m -averaged power spectrum illustrates the n -mode ridges with the lowest ridge corresponding to the f -mode, with the p_n modes following on.

surrounding penumbral region contains highly inclined magnetic fields, with a light intensity of 50% and an effective temperature of 5500 K. Sunspots always occur within active regions, usually leading the other smaller structures of an active region; pores, smaller opposite polarity follower sunspots. One such feature within active regions is magnetic plage (French for ‘beach’), and is typically observed as bright regions in CaII emission of the chromosphere. These bright features were first related to magnetic fields by Leighton (1959), and can be considered as collection of individual magnetic flux tubes (as opposed to the closely packed pores) situated within the plasma surrounding large-scale magnetic features in active regions.

It is well established (Braun et al. 1988; Bogdan et al. 1993, etc.) that solar f - and p -modes interact strongly with sunspots, with up to 70% of the incident power being absorbed and substantial phase shifts being observed in the remnant outgoing waves. Plage also absorbs, although to lesser extent (around 20%; Braun 1995). Although Braun (1995) failed to identify any significant phase shift due to plage, later work (Chen et al. 1998; Braun and Birch 2008) found measurable time travel shifts of order 10 seconds, still considerably less than those observed within the penumbra and umbra regions (of order 20 and 40 seconds respectively).

1.3 Wave Propagation In Solar Atmospheres

In order to understand the interaction of acoustic waves within and around active regions, it is necessary that theoretical models agree with observable parameters. There is a large amount of literature on the mathematics of wave propagation in the sun (e.g. Goedbloed and Poedts 2004) and in this section, a brief overview will be given in order to understand the formalism in later chapters.

The solar atmosphere can be considered as ionized gas with a local pressure $p(\mathbf{r}, t)$, density $\rho(\mathbf{r}, t)$ and velocity $\mathbf{v}(\mathbf{r}, t)$ in the presence of the magnetic field \mathbf{B} . By assuming that the plasma is in a stationary ($\mathbf{v}_0 = 0$) equilibrium state ($\nabla p_0 = \mathbf{J}_0 \times \mathbf{B}_0 + \rho_0 \mathbf{g}$), wave propagation within the magnetized plasma can then be understood through the Linearized Magnetohydrody-

namic (MHD) equations,

$$\frac{\partial \rho_1}{\partial t} + \nabla \cdot (\rho_0 \mathbf{v}_1) = 0, \quad (\text{Continuity}) \quad (1.3)$$

$$\rho_0 \frac{\partial \mathbf{v}_1}{\partial t} = -\nabla p_1 + \mathbf{J}_0 \times \mathbf{B}_1 + \mathbf{J}_1 \times \mathbf{B}_0 + \rho_0 \mathbf{g}, \quad (\text{Momentum}) \quad (1.4)$$

$$\frac{\partial p_1}{\partial t} = -\mathbf{v}_1 \cdot \nabla \cdot p_0 - \Gamma \nabla \cdot (p_0 \mathbf{v}_1), \quad (\text{Internal Energy}) \quad (1.5)$$

$$\frac{\partial \mathbf{B}_1}{\partial t} = \nabla \times (\mathbf{v}_1 \times \mathbf{B}_0), \quad (\text{Induction}) \quad (1.6)$$

where $\nabla \cdot \mathbf{B}_1 = 0$, $\mu_0 \mathbf{J}_0 = \nabla \times \mathbf{B}_0$, $\mu_0 \mathbf{J}_1 = \nabla \times \mathbf{B}_1$, Γ is the ratio of specific heats and the subscripts 0 and 1 represent the parameter's background and perturbations, respectively. In the absence of magnetic fields (quiet sun) and gravity, the above equations reduce to the standard hydrodynamic equations for an adiabatic gas, reducing to the common wave equation:

$$\frac{\partial^2 \rho_1}{\partial t^2} = c_s^2 \nabla^2 \rho_1, \quad (1.7)$$

where the sound speed of the acoustic waves depends upon the pressure and density of the atmosphere,

$$c_s^2 = \Gamma \frac{p_0}{\rho_0}, \quad (1.8)$$

The solution describing the motion of a purely acoustic wave is

$$\rho_1 = A e^{i(\mathbf{k} \cdot \mathbf{r} - \omega t)}, \quad (1.9)$$

where \mathbf{k} and ω are the wave vector and angular frequency, respectively, related through the dispersion relation:

$$\omega^2 = c_s^2 |\mathbf{k}|^2. \quad (1.10)$$

The above equations describe the propagation of an acoustic wave through a uniform non-magnetized medium. But if there was a magnetic feature within the medium, such as a sunspot or a slender flux tube, then the acoustic wave will interact with the magnetic fields and in turn will generate what is known as *magneto-acoustic waves*. These waves are classified as Alfvén, fast and flow magneto-acoustic waves. In short, the Alfvén wave is an incompressible magnetic wave that propagates along a magnetic field inducing transverse motion of the field. The fast and slow waves have magnetic and acoustic properties and propagate with both longitudinal and transverse motion of the gas in general. Considering the aim of magneto-seismology is

to probe the internal constitution of large scale magnetic features, it is important to develop sound theoretical models to describe how propagating acoustic waves can induce motion within magnetic structures and vice-versa. Gravity also greatly complicates the picture, and will be addressed in detail.

1.4 An Analytical Approach to thin flux tube interactions

In local helioseismology, there has been growing interest in the interaction between distinct thin magnetic flux tubes, in particular, the mechanisms that govern the way one tube can induce motion in close neighbouring tubes through the scattering of incident waves. This section outlines the previous research into such interactions and serves as a literature review for the research presented in Chapters 2 and 3

Presently all studies attempting to model the behaviour of waves and magnetic features can be classified as stratified or unstratified studies. When an atmosphere is stratified, it is situated within a (to good approximation) constant gravitational field ($\mathbf{g} = -g\hat{\mathbf{z}}$). However, the earliest scattering studies were primarily unstratified due to the complex nature of the mathematical formalisms that gravity creates. In these cases the pressure and density terms are constant with height, and hence the wave eigenfunctions can be described as a plane waves (Equation 1.9).

1.4.1 Unstratified Media

Observational studies by Leighton (1963) and Simon and Leighton (1964) were the first to show that the solar surface is ubiquitously threaded by thin magnetic flux tubes, with a width of a few hundred kilometres and field strength around 1-2 kG. These results challenged the assumption that solar wave propagation should be considered in large scale magnetic fields alone (e.g. Chandrasekhar and Lebovitz 1962). Instead the interaction of waves with discrete magnetic filaments must also be modelled. This discovery instigated a series of studies into the behaviour of ensembles of thin magnetic filaments that were situated within a unstratified medium. The overall goal of these studies was to examine whether subsurface structures could be inferred from the observable wave field that is altered by the presence of magnetic fields.

Bogdan and Zweibel (1985) were the first to model the interaction of ‘*p*-modes’ with a flux tube bundle, by considering a model atmosphere with no gravitational force. This study showed that as a plane wave propagates through an infinite medium filled with slender tubes, the frequency would shift proportionally to the half-space filling factor (i.e. +0.3% frequency shift of the 5 minute mode for a 1% filling factor). Later, Bogdan and Zweibel (1987) then attempted to characterize a scattering regime within an ensemble of magnetic flux tubes (compared to diffuse medium), finding that an incident wave’s energy would cascade to smaller scales the further a wave propagated into a fibril medium. Bogdan (1987a) expanded on this study by finding a finite width region of tubes behaves more like a diffuse slab in comparison to an infinite half-space region of tubes. Furthermore, Bogdan (1987b) noted the presence of compressive modes with a phase-speed less than the sound speed, that resulted from energy deposition upon the tube. Other fibril region studies include Ryutova and Priest (1993a,b) who examined the effects of various parameters (field, densities, inclination and filling factor) on wave propagation within a fibril region, finding the most important parameters are the filling factor and tube’s spatial positions. Additionally, these studies showed that a random distribution of flux tubes will create certain resonance conditions, where energy input is more efficient depending upon the nature of the tubes within the small region.

Motivated by the goal of ascertaining the subsurface structures of magnetic regions, Bogdan and Fox (1991) and Keppens et al. (1994) examined the possibility of whether the internal structure of an ensemble could be deduced indirectly from the scattered wave field. Specifically, could the nature of a sunspot (monolithic flux tube or spaghetti like ensemble) be determined from the scattered wave field. Bogdan and Fox (1991) investigated the behaviour of a pair of tubes and found the existence of three scattering regimes; incoherent, coherent and the multiple scattering regime. In the incoherent scattering regime, the tubes are separated by large distances ($d \gg \lambda$, where λ is the wavelength) and thus the total scattering cross section is the addition of the two tube’s individual scatter. The coherent scattering regime involves intermediate separation distances ($d \approx \lambda$), where the scattering cross section is significantly altered when compared to the incoherent scheme. Finally, the multiple scattering regime occurs when the tubes are very close and the scattering effects of one tube is altered by the presence of the other, and vice versa. This in turn significantly alters the scattering cross section of the system. In fact, Keppens et al. (1994) showed that, due to the multiple scattering regime, the absorption of a closely packed ensemble differed

1.4. AN ANALYTICAL APPROACH TO THIN FLUX TUBE INTERACTIONS

significantly from an equivalently large monolithic tube. The cause of this enhanced absorption was attributed to the wave scattering between tubes, which increased the overall absorption of each tube. Additionally, it was found that a bundle of non-uniform fibrils would have increased absorption due to scattering resonances, similar to Ryutova and Priest (1993a,b).

The absence of gravity in theoretical models is attractive for mathematical simplicity. However, if the waves were allowed to propagate downward into the solar interior (due to gravitational effects) would these resonances persist? Hasan and Bogdan (1996) and Hasan (1997) suggested that gravitational stratification of the atmosphere removes the resonances that could occur within a single tube. However, Tirry (2000) demonstrated that it is not the stratification per se of the atmosphere that removes the resonances; rather it is the presence of a mechanism that allows downward energy loss. This was shown in an unstratified model that allowed the wave energy to effectively escape through a ‘hole’ at the bottom of the tube. Furthermore, Tirry (2000) showed that in a bundle of tubes, scattering resonances were eliminated by allowing tube waves to escape through the bottom of the box.

While these early models were restricted to unstratified media, they nevertheless demonstrated interesting characteristics of ensemble behaviour that could be used for determining subsurface structures, such as flux tube bundles. The inclusion of gravity will change the way the multiple scattering regime is understood within the solar surface.

1.4.2 Stratified Media

Having discussed the implications and findings of unstratified studies, this section will present the current body of work concerning stratified atmospheres and the significance of the multiple scattering regime. We will begin by briefly outlining the mathematics of stratified atmospheres to specify the nature of the atmosphere below the photosphere. Additionally, the implications of gravity on wave solutions will be discussed. Finally, the results of previous studies and in light of these results, the aim of this research will be outlined.

For stratified atmospheres, most models have an upper boundary that coincides with the $\tau_{5000} = 1$ level (see Maltby et al. 1986), where the τ_{5000} level is the optical depth of the solar surface. Typically, studies into wave propagation in stratified atmospheres (e.g. Hanasoge and Cally 2009; Hindman and Jain 2012) follow the mathematical formalism outlined in Bogdan et al. (1996). Here the atmosphere is under a constant gravitational force

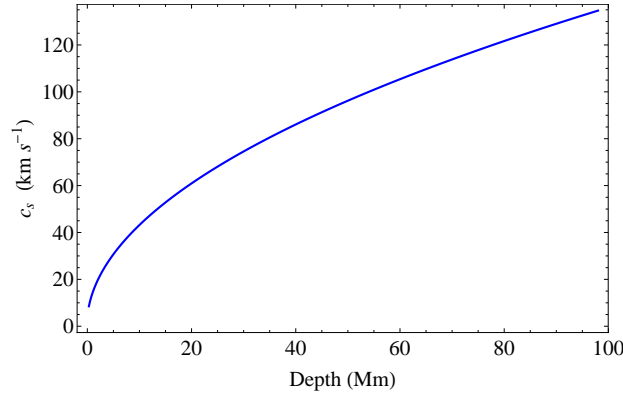


Figure 1.3: The adiabatic sound speed of an acoustic wave within a non-magnetized medium outlined in Bogdan et al. (1996). The sound speed is calculated from Equation (1.8)

($\mathbf{g} = -g\hat{\mathbf{z}}$) and pressure and density vary with depth below a reference height z_0 ,

$$p(z) = \frac{\rho_0 g z_0}{m_p + 1} \left(-\frac{z}{z_0} \right)^{m_p + 1} = p_0 \left(-\frac{z}{z_0} \right)^{m_p + 1}, \quad (1.11)$$

$$\rho(z) = \rho_0 \left(-\frac{z}{z_0} \right)^{m_p} \quad (1.12)$$

where $m_p = 1/(\Gamma - 1)$ is the adiabatic polytropic index. Herein, ρ_0 is the reference density and p_0 the reference pressure, at z_0 . With a stratified atmosphere the sound speed of acoustic waves depends upon the depth into the solar interior (Equation 1.8). Figure 1.3 shows the adiabatic sound speed for the most commonly used stratified atmosphere model (Bogdan et al. 1996). Typically shallow depths below the photosphere have a sound speed of around 10 km s^{-1} and increase with depth proportional to \sqrt{z} .

Within gravitationally stratified media, magnetic flux tubes exhibit both discrete and continuous spectra of oscillation, the former related to the f - and p -modes of the external medium, and the latter deriving from the acoustic jacket (Bogdan and Cally 1995; Cally 2013) of horizontally bound (‘near field’) slow waves that propagate vertically on the tube and take energy away. These waves play an important role in the multiple scattering regime (Hanasoge and Cally 2009). Since stratification requires the inclusion of the near-field modes and removes resonances, it then falls to the near-field multiple scattering regime to explain the observed scattering and absorption.

When examining the interaction between thin magnetic flux tubes, there are three main mechanisms to describe. Firstly, an incident propagating wave

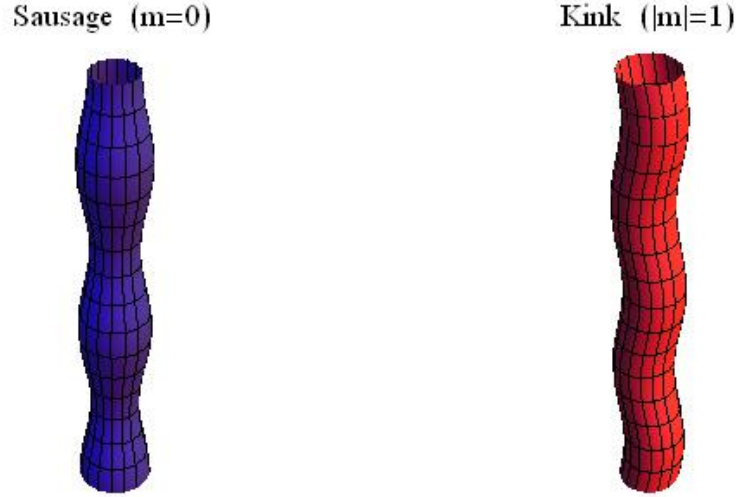


Figure 1.4: An illustration of a thin flux tube moving due to sausage (left) and kink motion (right).

interacts with a single flux tube, depositing some of its energy, which then manifests as tube motion. Secondly, the remainder of the incident wave is scattered into the surrounding medium (with the same frequency). Finally, the scattered wave field then interacts with neighbouring tubes, depositing more energy onto these tubes causing further scatter. These interactions then change the overall scattering properties of each tube within the bundle, which is the nature of the multiple scattering regime.

Bogdan et al. (1996) was the first to describe the motion induced in a flux tube by an incident wave. It was shown that an incident wave upon a flux tube could produce two types of motions, called the kink and sausage motion. Figure 1.4 is a sketch illustrating the nature of a slender flux tube undergoing kink or sausage motion. The mathematical description of these modes will be addressed in Chapter 2. It is generally thought that these two modes are separate motions and this assumption is used in most studies (both unstratified and stratified). However, recent work by Goossens et al. (2014) has shown the kink motion of a flux tube will decay into azimuthal motion (sausage) given enough time.

The work of Bogdan et al. (1996) inspired numerous studies into the nature of the scattered wave field of a single tube. With regards to the kink

motion of a flux tube, Hanasoge et al. (2008) showed that the dominant mode, scattered from a single tube, was the f -mode with an absorption of 1.17% and phase-shift of 50° . It was also shown that these scattering properties increased with the frequency of the incident wave and whether the tube had a magnetic pressure dominance. With regards to the sausage mode Hindman and Jain (2012) and Andries and Cally (2011) both showed that this mode had a small absorption with relatively large phase shifts (up to 15°) for an incident f -mode. While these studies outline and demonstrate the scattering behaviour of a single tube, it is then logical to extend these studies to investigate bundles of tubes.

Jain et al. (2009, 2011a,b) modelled ensembles within a stratified atmosphere, but neglected any scattering regimes and thus addressed the ensemble as a collective of individual non-interacting tubes. It was shown that the absorption of a tube ensemble (interacting purely through sausage motion) depended significantly on the magnetic pressure of the tubes and the distribution of these pressures across the ensemble. In fact, an ensemble with a narrow distribution of plasma β and a mean value between 0.5 and 1 closely matched observational results. While these studies ignored the effect of the jacket modes, and hence the multiple scattering regime, they are nevertheless informative about the effect of frequency and plasma- β distributions on ensemble absorption. Hanasoge and Cally (2009) were the first to outline the significance of the multiple scattering regime between pairs of tubes by utilizing the analytical methods of Kagemoto and Yue (1986). They showed that the horizontally evanescent near-field plays a significant role in altering the scattered wave field coefficients when the tubes are in close proximity. For the purpose of conciseness, we will discuss this study further in chapter 2 but we will note Hanasoge and Cally (2009) focused upon two tubes interacting purely through the kink modes.

So far no analytical study has examined multiple scattering of both the sausage and kink motion within a stratified medium. However, a growing body of numerical studies have begun to shed light on the significance of this regime. Felipe et al. (2013) showed that the multiple scattering regime significantly impacts absorption coefficients, as well as generally decreasing the phase shift of the outgoing wave. Also, it was noted that absorption generally increases with the number of tubes. Daiffallah et al. (2011) found that tube radius play an important role in the generation of kink and sausage motion. They demonstrated that the kink motion is dominant in small radius tubes (compared to wavelength), while sausage and kink motion occurred in intermediate radius tubes and numerous modes (including high $|m| > 1$)

occurred in large radius tubes. Additionally Daifallah (2014) investigated the surface velocity profiles created by an ensemble of closely packed thin tubes, showing that relative tube position and separation plays a significant role in the resultant vertical velocity profiles.

1.5 Morphology of Acoustic Power Halos

While mathematical modelling has its merits, it is meaningless without observational constraints. The purpose of this section is to provide a brief introduction into the phenomenon known as enhanced acoustic power halos that surround active regions. This knowledge is required to understand the observational research performed in this thesis. Following this, an outline of Helioseismic Holography will be given. Holography is one of the many local helioseismology tools used in understanding solar magneto-seismology and power halos.

1.5.1 Seismic Emission within Acoustic Power Halos

The enhanced acoustic power surrounding active regions has been the focus of many recent observational and numerical studies. These enhanced regions are commonly referred to as *acoustic halos* and typically have a local power that exceeds that of the quiet sun by 40-60% (Hindman and Brown 1998, etc). These halos were first observed near the photosphere by Brown et al. (1992) and have since been observed at chromospheric heights (Braun et al. 1992; Toner and Labonte 1993). Thus far, the mechanisms responsible for this phenomenon are not well understood. With regards to the morphology, Khomenko and Collados (2009) provide a concise summary, and the key points are:

- i) a disproportionate enhancement of acoustic power occurs in the 5.5 – 7.5 mHz frequency range;
- ii) the halos occur in low to intermediate field strength (50-250G) (Hindman and Brown 1998), and diminish rapidly with greater field magnitudes;
- iii) enhancement is aided by regions of near-horizontal field inclination, in particular between locations of opposite polarity (Schunker and Braun 2011; Rajaguru et al. 2013).

Numerous theories have suggested possible mechanisms responsible for the halo phenomenon. In simulations, Jacoutot et al. (2008) showed that

high frequency turbulent convective motions, in the presence of moderate magnetic fields, may enhance the local acoustic emission. Another study by Khomenko and Collados (2009) proposed that the refraction of fast mode waves in the higher atmosphere could deposit additional energy into the photospheric regions of intermediate field strength. Also, Kuridze et al. (2008) suggested that high order azimuthal modes may become trapped under the magnetic canopy, enhancing the observable vertical velocity power. Meanwhile Hanasoge (2008, 2009) argued that enhanced acoustic oscillations may be the result of MHD mode mixing (scattering). While these theories all propose different mechanisms, further observational statistics are required in order to test and examine their validity.

Typically in observational studies, the acoustic power is determined from the local Doppler signature at a given point on the solar surface. It is then a standard procedure to use these Doppler images to generate and interpret power maps at frequencies between 2-10 mHz. In these local Doppler power maps, the acoustic waves (*p*-modes) generated by convective motions, as well any additional seismic source mechanisms will be seen. In order to differentiate the additional seismic sources, apart from the background oscillations, the computational seismic holography technique is applied (Lindsey and Braun 1997). These holography power maps show the possible seismic sources that generate outgoing waves, which reemerge some distance away.

While there is a large degree of similarity between the local acoustic power maps and the seismic source maps, a study of the relationship between the power distribution of seismic emission and local oscillatory power, within their respective halos, has not been done. In the latter part of this thesis, we will examine both the local oscillation power (referred to herein as *local acoustic power*) and the seismic power that is emitted from a point and resurfaces some distance away (referred herein as *seismic emission power*). We will compare these with other observational images of an active region, such as vector magnetograms, in order to further understand the acoustic morphology of complex active regions.

1.5.2 Computational Helioseismic Holography

In this section the background knowledge of Helioseismic Holography will be given. This is done so that the reader can understand the underlying physics and limitations needed for and imposed by holography, and to explain the differences between the two types of enhanced power halos.

Helioseismic holography is a computational procedure that reconstructs

the solar acoustic wave field at some arbitrary depth within the solar interior. The concept was first developed for application on SOHO and GONG data in the 1990's by Lindsey and Braun (1990), Braun et al. (1992) and Lindsey and Braun (1997). Chang et al. (1997) developed a similar technique which was used on Taiwan Oscillation Network (TON) data. In terms of solar acoustics, holography is used to regress an observed surface wave field backwards in time to a chosen focal depth. In doing so, a three-dimensional acoustic field can be computed and any acoustic sources/sinks examined (see Figure 1.5). The technique is called 'holography' because it is similar to the reconstruction of a three dimensional image through the use of lasers by phase-coherent reconstruction of the monochromatic radiation recorded on two dimensional photographic 'holograms'.

Helioseismic holography was fashioned expressly as a local discriminator of helioseismic anomalies, such as sunspots and plages (Braun and Lindsey 2000a,b), seismic transients of flares from the near solar hemisphere (Lindsey and Donea 2008), active regions in the Sun's far hemisphere (Lindsey and Braun 2000b; Braun and Lindsey 2001), or magnetic anomalies submerged in the solar interior (Lindsey and Braun 1997; Braun et al. 1992).

The formalism relies on the convolution of a Green's function (G_{\pm}) to time reverse an observed acoustic wave field $\psi(\mathbf{r}', t')$ to a location and time (\mathbf{r}, z, t) . This in turn renders a regressed acoustic wave field at a chosen depth z ,

$$H_{\pm}(z, \mathbf{r}, t) = \int dt' \int_{a < |\mathbf{r} - \mathbf{r}'| < b} d^2\mathbf{r}' G_{\pm}(z, \mathbf{r}', t', \mathbf{r}, t) \psi(\mathbf{r}', t'). \quad (1.13)$$

Here H_+ is the *egression* and H_- is the *ingression*, where the \pm subscript indicates whether the the point being examined is the source or destination of the computed wave field, respectively. These computations are typically performed over an annular region, referred herein as the *pupil*, with an inner radius of a and outer radius b . Generally the inner radius size determines the resolution of the egression power maps, while a large outer radius samples a broader range of wavelengths, hence more power is calculated. By centring the pupil at a particular point on the solar surface, any wave field observed within the surrounding annular region is then regressed through time to their origin/destination at the pupil centre. In doing so, the emission of acoustic waves that then re-emerge at the surface can be examined.

In terms of depth diagnostics, Holography has the capability to examine both deep and near-surface sources/sinks, by simply pushing the focal plane

to the desired depth. The technique for examining the sources emitted from the near surface and re-emerging some distance away is known as ‘Subjacent Vantage Holography’ and is illustrated in Figure 1.6. In contrast ‘Superjacent Vantage Holography’ works on the basis that the source is emitted deep within the surface and travels upwards emerging at the surface. The former is usually the preferred technique when examining active regions, as the latter’s computed wave field can be confused with perturbations within the active region.

It must be kept in mind that helioseismic holography does have its limitations. Similar to electromagnetic holography and lens optics, helioseismic holography is subject to the effects of interference and diffraction (see review paper by Lindsey and Braun 2000a). This ultimately means that a computed wave field may be subject to the affects of sinks/sources just above or below the focal plane. Similar to a microscope, as the focal plane approaches an object it will appear to the observer that the object is in the focal plane, though out of focus. This in turn creates an incoherent representation of locally generated noise, to which the actual wave-field is superimposed. The appearance of this out of focus noise is known as *stalactites* and *stalagmites*, depending on whether the object is above or below the focal plane respectively. While some studies are not concerned with depth diagnostics (such as this thesis), this limitation must be kept in mind as it is conceivable that half of the computed egression/ingression power is incoherent noise.

Applications to Power Halos

Since its development Helioseismic holography has been used extensively to examine (and discover) numerous physical phenomena within the solar interior. It is well established that the strong interaction of p -modes with active regions (Braun et al. 1987, etc) results in strong absorption and phase-shifts. The absorption of p -modes can be seen as a power deficit with the egression power $|H_+|^2$, where the strong magnetic fields act as a wave-field sink. Braun et al. (1998) and Lindsey and Braun (1998b) calculated 3 mHz egression power maps (seismic emission) showing that similar to Hankel analysis, a strong compact power deficit (no sources) is associated with sunspots and surrounding magnetic plage. However, these studies also reveal a significant power deficit extending from the active region, referred herein as an *acoustic moat*. When the focal plane was submerged into the solar surface, Lindsey and Braun (1998a) and Braun and Lindsey (1999) showed that a seismic deficit (associated with the sunspot) could persist to depth of 10 Mm. How-

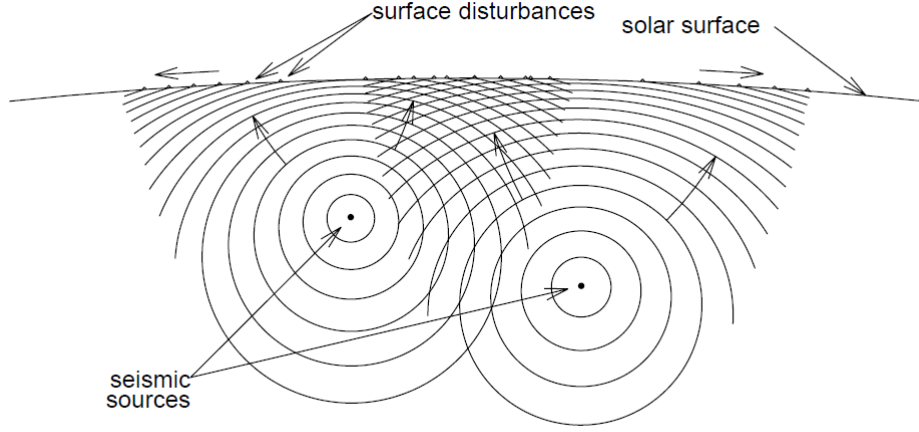


Figure 1.5: Submerged seismic sources propagate to the surface to create the observed surface acoustic wave field. Helioseismic holography can approximate the position of these point sources. Image from Lindsey and Braun (2000a).

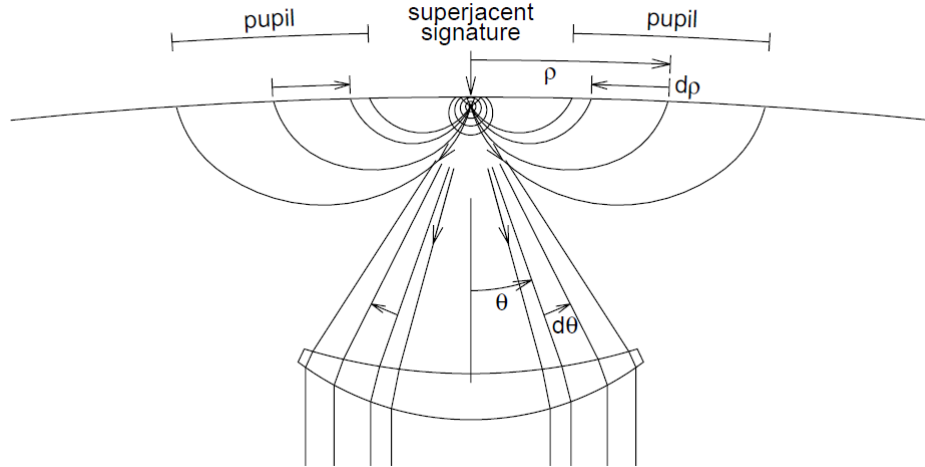


Figure 1.6: An example of an acoustic wave field sampled within the pupil, that originates from a point located at some depth below the centre of the annular region. Image from Lindsey and Braun (2000a).

ever, the concept that efficient acoustic absorption could occur below 5 Mm is problematic (see Lindsey et al. 1996; Lindsey and Braun 1998a) and it was suggested that such computed wave fields are affected by scattering (thermal or Doppler perturbations) of the power deficit located at the surface.

While an acoustic moat is present at low frequencies (at 3 mHz), at higher frequencies (> 4.5 mHz) a conspicuously enhanced region of acoustic power is present. When investigating AR 081799, Braun and Lindsey (1999) called this enhanced region the *acoustic glory*. This glory surrounded a multi-polar region and was found to be seismically intense with an average power of $\sim 115\%$ quiet sun values. In contrast, a circular sunspot in the same active region possessed no glory, suggesting that these halos are associated with multi-polar regions. Braun and Lindsey (1999) further found that the halo contained small-scale intense seismic emitters ($\sim 150\%$ quiet sun values), that were associated with the magnetic neutral line of the active region.

When investigating the same active region (AR081799) and the relationship between intense seismic emitters and magnetic fields, Donea et al. (2000) confirmed that these emitters were generally located in quiet sun regions. It was shown that the most intense emitters were aligned along the magnetic neutral line, while others were also present on the boundary of weak magnetic fields. Donea et al. (2000) also found that acoustic emission, both in the magnetic peripheries and in the quiet Sun, appears to maintain a temporal character no more episodic than random Gaussian noise. In a similar study of other active regions, Donea and Newington (2011) found the acoustic glories associated with multi-polar active regions (AR08996 and AR08179) were generally weak, diffuse and lacked any bead like structures as found by the aforementioned study. But it was suggested that the seismic emitters could contaminate the surrounding quiet sun regions, creating an acoustic glory (halo).

1.6 Basis for this Research

In the past few decades, high resolution observations have revealed a plethora of acoustic phenomena occurring within and around solar magnetic features. As previously discussed in this chapter, there is a number of open questions regarding the relationship between magnetic fields and acoustic waves within the solar surface.

This thesis will address some of these questions through a detailed analysis of the behaviour of acoustic waves with magnetic fields. I aim to address

the pertinent questions through: (i) the development of a semi-analytical model to address the nature of the multiple scattering regime within a flux tube bundle, between constituent tubes, that are situated within a stratified atmosphere, (ii) by undertaking a comprehensive study of seismic emission surrounding complex active regions, in order to identify a relationship with magnetic fields, and to compare these seismic sources with the local acoustic oscillations.

The key research questions I set out to address in this thesis are as follows:

1. How to successfully model the interaction between a pair of thin flux tubes, utilizing the solutions of both the kink and sausage motion of the tube.
2. How to settle a disparity between semi-analytical and numerical studies, with regards to the symmetry of $\pm m$ waves.
3. What parameters (frequency, magnetic pressure, etc.) change the observable absorption and phase-shift?
4. How to model a large ensemble that is able to interact with high order modes ($|m| > 1$).
5. What is the relationship between the magnetic field and seismic emission, and are there any similarities with the relationship between local acoustic oscillations and magnetic fields?
6. What is the morphology of the seismic halo, and what properties of the active region affect this?
7. Is there a relationship between intense seismic emitters and the surrounding magnetic field configuration?

To address questions (1)-(4), the development of a mathematical model is required to describe the interaction of a wave with a single tube, and how the resultant scattered wave field effects nearby tubes and vice versa. The main aim of Chapter 2 is to outline the formalism of the model and to investigate the case of two tubes interacting through the multiple scattering regime. As outlined in section 1.4.2 previous studies have examined the kink and sausage motion of a single tube separately. This formalism will include descriptions of both motions, in order to obtain a more complete description of a thin flux tube within an ensemble. Then an outline of the formalism for the behaviour of a pair of flux tubes, including the powerful near-field scattering, will be

given. Numerous parameters will then be examined in order to identify their role in the multiple scattering regime. This model is the first step in describing the multiple scattering regime in large ensembles, and highlights the importance of this regime on overall absorption and phase-shifts.

The next step is to extend the model outlined in Chapter 2, to a large ensemble of flux tubes and this is achieved in Chapter 3. Continuing with the goal of comparisons to observational studies, we further develop the formalism to include high order fluting modes. We then examine collective behaviour through the study of various ensemble types. The ensembles examined include symmetric identical tube ensembles, randomly positioned identical tube ensembles, and random non-identical ensembles. It is the aim of this study to illustrate how the observed absorption and phase-shift can change due to the nature of the ensemble. Additionally, it is examined if the ensembles were replaced with single tubes of the same flux, whether the behaviour is similar or different.

With the semi-analytical study examined in Chapters 2 and 3, the focus of the thesis then shifts to addressing questions (5)-(7) in Chapter 4, with an observational study of the seismic emission surrounding complex active regions. Utilizing the data available from the SDO mission, in particular HMI and AIA data, we present detailed findings of three complex active regions that have enhanced seismic emission halos of varying extents. These halos are examined through the computation of egression power maps and are compared to the commonly examined local acoustic power halo. The active regions are of differing sizes and magnetic configurations, which result in different enhanced seismic emission. While recent studies by Schunker and Braun (2011) and Rajaguru et al. (2013) have examined the relationship between local acoustic power and the magnetic field, none has yet investigated the relationship with seismic source enhancement. Additionally, the similarities between these two types of halos have not yet been extensively examined. In this chapter, I present to the reader a comparison of three active regions, a study of the halo morphology, and a comparison of seismic emission and local acoustic power. This study takes strict statistical precautions in examining and comparing the magnetic field with the seismic emission. Finally, this chapter will compare the results in a qualitative fashion with the data from the AIA instrument, in order to speculate on the role of magnetic canopies with seismic enhancement.

This thesis shall then conclude with Chapter 5, where I will summarize the major findings of the thesis and discuss future research prospects. I acknowledge that this thesis is based on 3 published journal articles and one

unpublished paper. These papers were collaborations between myself and the co-authors. However, the majority of the work (initiation, data analysis, programming, modelling, discussions and write-up) was performed by myself.

Monash University

Declaration for Thesis Chapter 2: An Analytical Approach to the Scattering Between Two Thin Magnetic Flux Tubes in a Stratified Atmosphere

Declaration by candidate

In the case of Chapter 2, the nature and extent of my contribution to the work was the following:

Nature of contribution	Extent of contribution (%)
Key ideas, development of code, changes to formalism, modelling, production of results, writing of paper.	80

The following co-authors contributed to the work. If co-authors are students at Monash University, the extent of their contribution in percentage terms must be stated:

Name	Nature of contribution	Extent of contribution (%) for student co-authors only
Paul Cally	Supervision and guidance	

The undersigned hereby certify that the above declaration correctly reflects the nature and extent of the candidate's and co-authors' contributions to this work*.

Candidate's Signature		Date 13/10/2014
-----------------------	--	--------------------

Main Supervisor's Signature		Date 13/10/2014
-----------------------------	---	--------------------

*Note: Where the responsible author is not the candidate's main supervisor, the main supervisor should consult with the responsible author to agree on the respective contributions of the authors.

Chapter 2

An Analytical Approach to the Scattering Between Two Thin Magnetic Flux Tubes in a Stratified Atmosphere

This chapter outlines the formalism for the semi-analytical approach to the scattering between thin magnetic flux tubes, extending the work of Hanasoge and Cally (2009) with the inclusion of axisymmetric scattering. The formalism also modifies the theory of Hanasoge and Cally (2009) and the original formalism of Kagemoto and Yue (1986) to correct an unphysical symmetry breaking identified independently by Hanson and Cally (2014) and Felipe et al. (2012). The disparity is resolved within this chapter, and is found to be the result of an incorrect description of the near-field. A simple case of two thin flux tubes is examined, with results compared to other similar studies.

2.1 Introduction

Magnetic features ranging from ensembles of slender tubes to large monolithic or spaghetti-like structures, are ubiquitous on the solar surface. Thin magnetic flux tubes, like those found in plage, interact strongly with the Sun's acoustic p -modes, both absorbing and scattering incident waves (Braun et al. 1990). Whilst the mechanism for the observed absorption and scattering by large monolithic sunspots is fairly well understood, the similar (albeit smaller) observed effects of magnetic plage are not. Mechanisms operating within large structures are unlikely to be responsible for the absorption in smaller fibril structures like plage. Lately there has been a growing interest in developing a sound theoretical framework to model the collective behaviour of adjacent flux tubes.

The absorption and scattering observed in plage is thought to be the result of a scattering regime between thin flux tubes present within the ensemble. Upon encountering a single magnetic flux tube, a p -mode will lose some of its energy, which is deposited upon the tube, with the remaining energy scattered into the surrounding medium. The absorbed energy is then converted into a vertically propagating slow wave (Cally and Bogdan 1993; Bogdan et al. 1996) manifesting itself as kink or sausage like motion of the thin tube. Generally, the scattered energy propagates away with a different phase. Within the ensemble, the scattered wave field will then interact with nearby tubes and scatter again. This cascade of energy, as the waves scatter between tubes is the multiple scattering regime (Bogdan and Fox 1991). Initial attempts to model the multiple scattering regime were restricted to non-stratified media, due to the mathematical complexity that gravity introduces (Bogdan and Zweibel 1987; Keppens et al. 1994, etc). Bogdan and Zweibel (1987) were the first who attempted to characterize the multiple scattering regime, concluding that an incident wave's energy cascaded to smaller scales the further the wave travels into a fibril medium. Bogdan and Fox (1991) further shed light on the regime, finding that the scattered wave field from a pair of flux tubes will differ greatly from that of a single tube when the pair are within close proximity. Consequently, the nature (monolithic or spaghetti) of the scatterer could then be discerned from the scattered wave field (Keppens et al. 1994). However, neglecting gravity cuts out powerful near-field oscillations that can strengthen collective behaviour.

In the absence of gravity, the far field eigenfunctions suffice when matching internal and external wave fields. However, in a stratified atmosphere the downward propagating slow wave is also known to be an acoustic source,

manifesting as a near-field acoustic jacket around the tube (Bogdan and Cally 1995). When considering compact acoustic sources, the jacket modes heal the surface velocity signature by removing the singularity present at $r = 0$ (for axisymmetric cases) (Cally 2013). The jacket modes form an infinite continuum, are radially evanescent, and propagate up and down the tube. As a result, any neighbouring tube will experience both the far- and near-field generated by a flux tube, and in turn respond to it, contributing its own scatter to the external medium. The scatter contributions of all other tubes are no longer restricted to a discrete basis of far field modes, but rather consist of a combination of discrete far-field modes and a continuum of near-field modes. The description of the acoustic jacket and its continuous spectrum in analytical models is challenging, and few scattering studies have included it. In the case of an isolated thin tube, the mathematical formalism has previously been developed for the dipole ($m = \pm 1$), or kink (Hanasoge et al. 2008), and monopole ($m = 0$), or sausage (Hindman and Jain 2012; Andries and Cally 2011). Higher order fluting modes ($m \geq 2$) are not consistent with the thin flux tube approximation and will be ignored.

Scatter from an isolated tube is solely the product of the incident wave, and is restricted to the incident wave's azimuthal order (m). However, in the presence of nearby tubes, the scatter from all tubes must be calculated simultaneously as each tube will contribute to its neighbour's scatter. To add to this challenge, the scatter is no longer bound to the m mode of the incident wave and can now scatter into other m modes. Basing their theory on Kagemoto and Yue (1986), Hanasoge and Cally (2009) were the first to analytically describe the interaction between a pair of thin flux tubes in a stratified atmosphere. They focused on the interaction of the kink mode oscillations $m = \pm 1$, ignoring the sausage mode ($m = 0$) due to unsatisfactory boundary conditions, and concluded that the scatter properties of the pair changed dramatically when in close proximity. It was also concluded that the near-field's contribution to the altered scatter properties was significant, as it created a symmetry break between the $m = \pm 1$ scatter coefficients, even when the tubes were aligned along x . The near-field also altered the phase of the outgoing wave, demonstrating bizarre and unpredictable changes as the tubes were separated. Recently, a numerical study by Felipe et al. (2013) examined the interaction between thick flux tubes, finding the absorption of m modes between the tubes to be effective in the multiple scattering regime. In contrast to Hanasoge and Cally (2009), they found that the multiple scattering regime can generate coherent phase change with separation distance, as well as a lack of symmetry breaking between the ± 1 modes in the near-field.

The aim of this chapter is to incorporate the sausage mode into the semi-analytical model of Hanasoge and Cally (2009), to investigate the interactions between the kink and sausage modes, and to settle the disparity with the numerical results of Felipe et al. (2013). This formalism is based on Hanasoge and Cally (2009), and uses the arguments presented by Hindman and Jain (2012) and Andries and Cally (2011) to implement the sausage mode. We will then be able to compare our calculations with seismic analyses of absorption and scattering by plage on the Sun (e.g., Braun 1995) to determine if the model captures the important characteristics of the interactions, and hopefully to draw conclusions about the nature of the constituent flux tubes.

Section 2.2 outlines the mathematical formalism for flux tube scattering, with Section 2.2.5 outlining the interaction with neighbouring tubes. Section 2.4 outlines the results, with the relevance and comparison to Hanasoge and Cally (2009) and Felipe et al. (2013) discussed in Section 2.5.

2.2 Mathematical Formalism

2.2.1 Wave propagation in the Polytrope

In this section we outline the interaction of flux tubes embedded in a stratified atmosphere of constant gravity. The field-free atmosphere is an adiabatically stratified ($\mathbf{g} = -2.775 \times 10^4 \text{ cm s}^{-2} \hat{\mathbf{z}}$) truncated polytrope of index $m_p = 1.5$. Following Hanasoge and Cally (2009) we use an atmosphere with boundaries at depths of 392 km (z_0) and 98 Mm below the photosphere. The pressure and density of the atmosphere were previously given in Equation 1.11 where $p_0 = 1.21 \times 10^5 \text{ g cm}^{-1} \text{ s}^{-2}$ and $\rho_0 = 2.78 \times 10^{-7} \text{ g cm}^{-3}$. Here we adopt a right-handed cylindrical coordinate system, where $\mathbf{x} = (r, \theta, z)$. From this point on the index m will denote the azimuthal order of the incident wave mode and m' the scattered.

Under constant gravity the velocity potential must then satisfy (Lamb 1945, p548):

$$\frac{\partial^2 \Phi}{\partial t^2} = c_s^2 \nabla^2 \Phi - g \frac{\partial \Phi}{\partial z}, \quad (2.1)$$

which has a solution of the form

$$\Phi(\mathbf{x}, t) = \mathcal{A}_n s^{-(1/2)-\mu} W_{\kappa_n, \mu} \left(\frac{s\nu^2}{\kappa_n} \right) \cos(k_n^p x - \omega t) \quad (2.2)$$

where $s = -z/z_0$ and

$$\mu = \frac{m_p - 1}{2}, \quad \nu^2 = \frac{m_p \omega^2 z_0}{g}, \quad k_n^p = \frac{\nu^2}{2\kappa_n^p z_0} \quad (2.3)$$

are the convenient variables.

As discussed in the previous section, to accurately model stratified atmospheres the waves must be allowed to propagate further downward into the solar interior. As such there is a requirement that as $z \rightarrow -\infty$ the wave field will approach zero. By allowing this to occur, energy is allowed to escape through the bottom of the model and thus removes any potential resonances. However, at the top boundary ($z = z_0$) the solution requires a stress-free boundary condition $\nabla \cdot \xi = 0$. The stress-free boundary condition ensures that the pressure perturbations vanish, but prevents any upward travelling waves from escaping.

In this model a propagating f - or p -mode, with a vertical displacement eigenfunction Ψ_{inc} , is given by (Gizon et al. 2006);

$$\Psi_{\text{inc}}(\mathbf{x}, t) = \sum_{n=0}^{n_p} \sum_{m=-\infty}^{\infty} i^m J_m(k_n^p r) \Phi_m(\kappa_n^p; s) e^{i(m\theta - \omega t)}, \quad (2.4)$$

where $J_m(z)$ is the Bessel function of the first kind of order m and argument z . The n th order far-field eigenfunction is described by

$$\Phi_p(\kappa_n^p; s) = s^{-1/2-\mu} N_n \left[C_n^p M_{\kappa_n^p, \mu} \left(\frac{s\nu^2}{\kappa_n^p} \right) + M_{\kappa_n^p, -\mu} \left(\frac{s\nu^2}{\kappa_n^p} \right) \right], \quad (2.5)$$

where $M_{\kappa, \mu}(z)$ is the Whittaker M function of order κ , μ and argument z , N_n is the normalization constant for any p_n mode. These convenient dimensionless constants are defined in section 1.4.2. The corresponding eigenvalues κ_n are obtained through the relations outlined in Appendix A of Hanasoge et al. (2008). Here $n = 0$ corresponds to the f -mode and $n \geq 1$ to the p_n -modes. Figure 2.1 shows the displacement eigenfunctions (Φ_n) for different n 's. The f -mode's motion is restricted to the surface, while increasing n results in displacement deeper within the polytrope. The inclusion of gravity invokes the need to include not only a discrete set of far-field modes but also a continuous infinite set of near-field modes (Bogdan and Cally 1995). The near-field eigenfunction differs from the afore mentioned propagating eigenfunction through having complex roots:

$$\zeta_p(\kappa_n^J; s) = s^{-1/2-\mu} \left[C_n^J M_{-i\kappa_n^J, \mu} \left(i \frac{s\nu^2}{\kappa_n^J} \right) + M_{-i\kappa_n^J, -\mu} \left(i \frac{s\nu^2}{\kappa_n^J} \right) \right]. \quad (2.6)$$

In truncating the polytrope, much like Barnes and Cally (2000), at 98 Mm we reduce this continuous spectrum of jacket modes to an unphysical discrete spectrum. This truncation is required in order to utilize the interaction

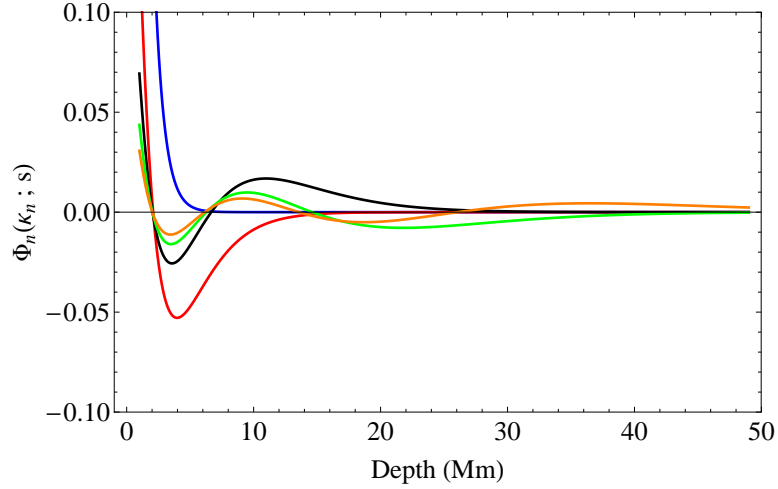


Figure 2.1: The vertical eigenfunctions (Equation 2.5) for an incident f -mode (blue), p_1 (red), p_2 (Black), p_3 (Green), p_4 (Orange). The f -mode is restricted to the surface, but with increasing n the plasma displacement becomes greater with depth. These modes interact with the magnetic flux tube inducing motion (Figure 2.2)

theory of Kagemoto and Yue (1986). By selecting a large enough discrete set of jacket modes, we mimic the true jacket spectrum and develop an understanding of the nature of near-field interactions. Selecting a larger set (1500) of jacket modes than the one we have used (1000), alters the results by less than a percent.

2.2.2 Thin Flux Tubes

The determination of the scattering matrix for a single tube is essential in trying to understand the interaction between nearby flux tubes. Consider a flux tube that is embedded in a field free atmosphere that responds to an incident f -mode. At depths below $s = 1$ the filament's radius is small when compared to the incident wavelength. The relatively small radius allows for the utilization of the thin flux tube approximation, as outlined by Bogdan et al. (1996). In this approximation, the longitudinal magnetic field b and the tube radius R are given by

$$b(z) \approx \sqrt{\frac{8\pi p(z)}{1 + \beta}}, \quad \text{and} \quad \pi R^2(z) \approx \frac{\Phi_f}{b(z)}, \quad (2.7)$$

where $\Phi_f = 3.88 \times 10^{17}$ Mx is adopted as the total magnetic flux per tube throughout this article. The parameter β is defined as the ratio of gas pres-

sure to magnetic pressure and is commonly referred to as plasma- β . Rapid expansion of the flux tubes above this height requires both the introduction of complex higher order fluting modes, as well as a variable plasma- β across the tubes' cross-sections. In the thin tube approximation their slender nature forces β to be constant throughout the tube, as it is in thermal and radiative equilibrium with the field free atmosphere. This is distinct from the thick tubes of Felipe et al. (2013), where β varies both along and across the tube.

2.2.3 Tube Oscillations

Thin magnetic flux tubes are only capable of two oscillating modes, the $m = 0$ and $m = \pm 1$, where $e^{im\theta}$ dependence is assumed. Incident waves, Ψ_{inc} , of these m mode orders generate horizontal and vertical displacement within the tube (Figure 2.2), resulting in the tube oscillating in a sausage ($m = 0$) or kink ($m = \pm 1$) like motion according to

$$\begin{aligned} \left[\omega^2(2m_p + \beta(m_p + 1)) + \frac{2gs}{z_0} \frac{\partial^2}{\partial s^2} + \frac{g(m_p + 1)}{z_0} \frac{\partial}{\partial s} \right] \xi_{\parallel} \\ = -\omega^2(m_p + 1)(\beta + 1) \frac{\partial \Psi_{\text{inc}}}{\partial s} \end{aligned} \quad (2.8)$$

and

$$\begin{aligned} \left[\omega^2 z_0 + \frac{2gs}{(1 + 2\beta)(m_p + 1)} \frac{\partial^2}{\partial s^2} + \frac{g}{1 + 2\beta} \frac{\partial}{\partial s} \right] \xi_{\perp} \\ = \frac{2(1 + \beta)}{1 + 2\beta} \omega^2 z_0 \frac{\partial \Psi_{\text{inc}}}{\partial x} \end{aligned} \quad (2.9)$$

respectively (Bogdan et al. 1996), where ω is the angular frequency of the incident wave. Here ξ_{\perp} and ξ_{\parallel} are the tube's displacements perpendicular and parallel to the z axis, respectively.

2.2.4 The Scattered Wave Field

In terms of the energy budget for the system, not all of the energy of an incident wave is transferred to vertically propagating slow waves. Some of the energy is scattered by the flux tube into the external medium. This scattered wave field is determined through the matching of the internal motion and the pressure to those of the external medium. Thus, upon responding to an

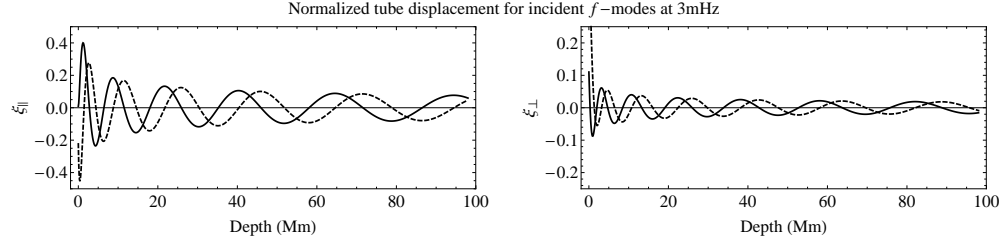


Figure 2.2: The real (solid) and imaginary (dashed) components of the normalized vertical and radial displacements (ξ/k_p) of a flux tube ($\beta = 1$), that is impinged upon by a 3 mHz f -mode of order $m = 0$ (left) and $m = 1$ (right). The motions are vertical and radial for the sausage and kink modes respectively. The slow magneto-acoustic waves travelling down the flux tube propagate into the solar interior, transporting energy absorbed from the incident wave.

incident wave, tube i 's scattered wave is:

$$\begin{aligned} \phi_i^S(r_i, \theta_i, s) = & - \sum_{m=-1}^1 \left[\sum_{n=0}^{n_p} S_{mn}^i \Phi_n(\kappa_n^p; s) H_m^{(1)}(k_n^p r_i) e^{im\theta_i} \right. \\ & \left. + \sum_{n=n_p}^N S_{mn}^i \zeta_n(\kappa_n^j; s) K_m(k_n^j r_i) e^{im\theta_i} \right], \end{aligned} \quad (2.10)$$

where $H_m^{(1)}(z)$ and $K_m(z)$ are the Hankel and K-Bessel functions of order m and argument z . The scattering matrix S_{mn}^i contains all the scattering coefficients of the propagating and evanescent modes. These coefficients are found through the mismatch between the internal and external wave fields.

Satisfactory boundary conditions must be maintained in the calculation of the scattering coefficients. This requires the pressure and horizontal displacement to match at the tube boundary. To leading order of tube radius R , as $R \rightarrow 0$, the pressure is of higher order (for all three wave fields: internal, scattered and incident) compared to that of the displacement for $|m| = 1$. The agreement at the tube boundary is then achieved, to leading order, through the matching of the horizontal displacement ξ_{\perp} alone:

$$S_{\pm 1 n}^i \xi_{\perp}^{\text{scat}} = \xi_{\perp}^{\text{int}} - \xi_{\perp}^{\text{inc}}, \quad (2.11)$$

where scat, int and inc are the scattered, internal and incident wave fields respectively. Whilst the matching of the kink modes is achieved relatively easily, the matching of the sausage modes has presented problems in the past. Unlike the kink mode matching, the pressure terms are not small, resulting in

both the pressure and displacement continuity needing to be maintained for all three wave field components. The complexity of matching all three terms in the thin tube approximation has restricted previous studies. However, the requirements and achievement of matching have recently been outlined by Hindman and Jain (2012) and Andries and Cally (2011) concurrently, through the comparison of small argument expansions (as $R(z) \ll \lambda$) of the Bessel functions. The internal and incident pressures can be matched to leading order R , since the scatter pressure terms are proportional to $\ln R$. Matching the internal and incident wave fields then maintains the pressure continuity. In turn, to leading order, the mismatch is then calculated through the matching of the internal normal displacement ($O(R)$), to that of the incident ($O(R)$) and scattered ($O(R^{-1})$) components. As long as the scatter terms are proportional to R^2 , the displacement continuity is maintained. Using these arguments, the scatter coefficients for the sausage mode are then calculated through

$$D_n S_{0n}^i \phi_n = \frac{R}{z_0^2} [N_{\text{inc},n}(\omega; z) - N_{\text{int},n}(\omega; z)], \quad (2.12)$$

where D_n is $-2i/\pi$ for $n \leq n_p$, and -1 for $n > n_p$ and $N = \tilde{\mathbf{n}} \cdot \nabla \Phi$ is the normal displacement (Hindman and Jain 2012).

The absorption and phase shift of waves encountering magnetic regions on the Sun's surface can be quantified through Hankel analysis (Braun 1995), whereby ingoing and outgoing waves in an annular pupil surrounding an active region or plage are compared. Plage in particular is made up of numerous flux tubes packed randomly but closely in an extended region. To make best use of Hankel data therefore requires the development of a multiple scattering theory including near-field effects. Although we only treat two tubes here, extension to many tubes will follow in Chapter 3. With these tools, we hope to be able to probe the nature of plage and its constituent flux tubes using observed absorption and phase shifts.

We define the absorption coefficient (α) of an (m, n) incident wave in the usual manner,

$$\alpha_{mn} = \frac{|A_{\text{in}}|^2 - |A_{\text{out}}|^2}{|A_{\text{in}}|^2}, \quad (2.13)$$

where A_{in} and A_{out} are the complex amplitudes of the incident and scattered waves respectively. The change in phase of the scattered wave is

$$\Delta\phi_{mn} = \arg \left\{ \frac{A_{\text{out}}}{A_{\text{in}}} \right\}. \quad (2.14)$$

The ‘absorption’ so defined includes both true absorption by the tubes, and scatter into other (m', n') outgoing waves. A single (circular) tube does not scatter in m , though it can in n . Multiple tubes will scatter in m as well. The energy scattered into these other modes is best quantified in terms of energy fractions. Generalizing the analysis of Hindman and Jain (2012, see their Eq. (27)), the fraction of the incident wave’s energy that is scattered to outgoing m' and n' is

$$\epsilon_{mn \rightarrow m'n'} = |\delta_{nn'}\delta_{mm'} + 2S_{m'n'}|^2, \quad (2.15)$$

where $S_{m'n'}$ are the scattering coefficients ($n \leq n_p$) of the outgoing (m', n') wave.

2.2.5 The Interaction Between flux tubes through the Scattered Wave Field

Having determined the scatter coefficients for a single tube i , we now build upon this matrix to include not only the incident wave but also the contribution of nearby tubes. Using the methodology of Kagemoto and Yue (1986), the scattered wave (Equation 2.10) from an isolated tube i is expressed in matrix notation as

$$\phi_i^S = \sum_n A_{in}^T \Psi_{in}^S, \quad (2.16)$$

where the summation is over all propagating and evanescent modes. In the summation the jacket modes follow on from n_p . Here A_{in} is a 3-element vector containing the scattering coefficients for the sausage and kink modes, whilst Ψ_{in} is a vector containing the scattered wave field from tube i . Specifically

$$A_{in} = - \begin{pmatrix} S_{-1n}^i & S_{0n}^i & S_{1n}^i \end{pmatrix}^T \quad (2.17)$$

$$(\Psi_{in}^S)_{cd} = H_{c-2}^{(1)}(k_n^p r_i) \Phi_n(\kappa_n^p; s_d) \quad (n \leq n_p) \quad (2.18)$$

$$(\Psi_{in}^S)_{cd} = K_{c-2}(k_n^p r_i) \zeta_n(\kappa_n^p; s_d) \quad (n > n_p), \quad (2.19)$$

where c ranges over $[1, 3]$, d over $[1, 250]$, and s_d is the d^{th} point along the s grid. Equation (2.16) describes only the zeroth order incident wave (ϕ_0) contribution. The scattered wave contribution from nearby tubes is then described as an incident wave upon tube i , and this is achieved through the *Transformation Matrix*. The transformation matrix \mathbf{T}_{il} relates the scattered wave field from tube i to an incident wave upon tube l , that has a radial separation of R_{il} and angular separation from the x axis of γ_{il} (Figure 2.3).

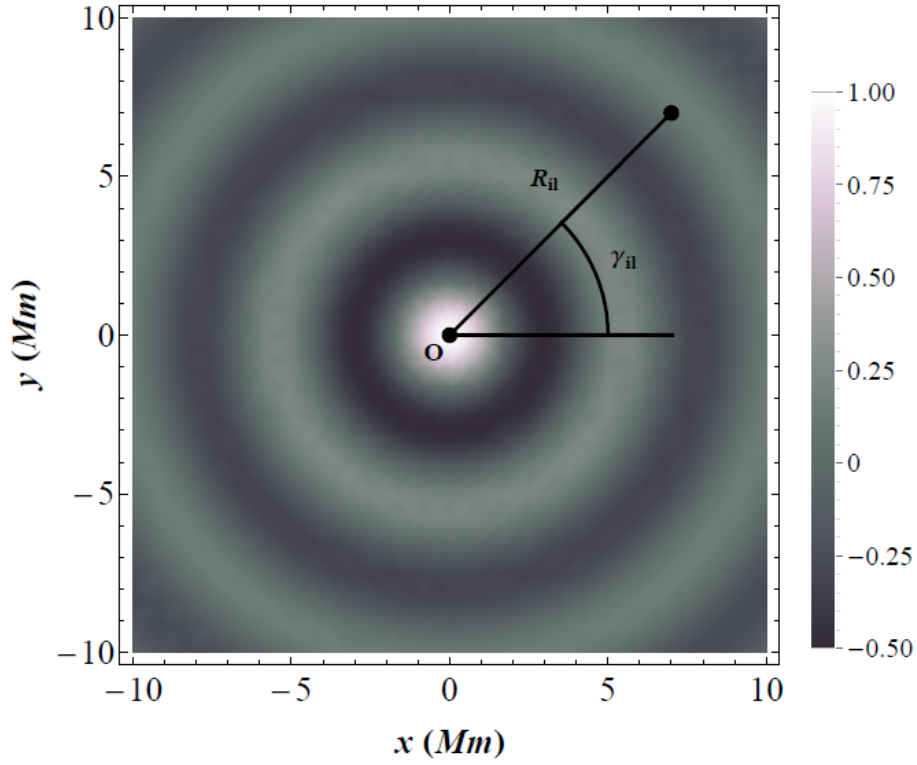


Figure 2.3: The orientation of a pair of flux tubes with variables graphically specified. The two tubes are separated by distance R_{il} , with the line at an angle of γ from the $+x$ axis. An incident sausage mode $J_0(k_p r)$ is centred upon one of the tubes, whilst the off-centre tube sees less of the incident wave the further away it is.

The elements of \mathbf{T}_{il} are derived from Graf's addition formula (Abramowitz and Stegun 1964):

$$H_m^{(1)}(k_n^p r_i) e^{im(\theta_i - \gamma_{il})} = \sum_{d=-\infty}^{\infty} H_{m+d}^{(1)}(k_n^p R_{il}) J_d(k_n^p r_l) e^{id(\pi - \theta_l + \gamma_{il})}, \quad (2.20)$$

$$K_m(k_n^j r_i) e^{im(\theta_i - \gamma_{il})} = \sum_{d=-\infty}^{\infty} K_{m+d}(k_n^j R_{il}) I_d(k_j^p r_l) e^{id(\pi - \theta_l + \gamma_{il})}. \quad (2.21)$$

By identifying the transformation components (Hankel and Bessel K) in Equations 2.20 and 2.21 that act upon the incident wave components (Bessel J and I), the individual elements that populate \mathbf{T}_{il} are then obtained. Specifically,

$$(\mathbf{T}_{il})_{pq} = e^{i(q-p)\alpha_{ij}} H_{q-p}^{(1)}(k_p R_{il}) \quad (n \leq n_p), \quad (2.22)$$

and

$$(\mathbf{T}_{il})_{pq} = (-1)^p e^{i(q-p)(-\pi/2 + \gamma_{ij})} K_{q-p}(k_j R_{il}) \quad (n > n_p) \quad (2.23)$$

where in this case $p = 3n + m' + 2$ and $q = 3n + m + 2$. Close inspection of the exponential in Equation (2.23) reveals that it is different from that of Kagemoto and Yue (1986) (as an $e^{-i\pi(q-p)/2}$ term is introduced), as well as Hanasoge and Cally (2009). This additional factor has been introduced because of the apparent break in symmetry between the $m = \pm 1$ in the near-field, and derives from representing the solution in terms of a Hankel function, instead of a Bessel K (see Abramowitz and Stegun 1964, Equation 9.6.4). Hanasoge and Cally (2009) concluded that jacket modes create a break in symmetry in the scattering coefficient between the $m = \pm 1$ modes, when the tubes are aligned along x . However, the only difference between the $m = \pm 1$ modes is the definition of the coordinate system. If the coordinate system were reflected around the x axis, the scattering coefficient should not change. Any tube located at the origin of the coordinate system should not be able to identify a difference in scatter between $m = \pm 1$ from the off-centre tube when it is on the x -axis. The apparent break in symmetry is significant in the near-field, but this is due to the chosen solution describing the jacket and incident wave fields described in Kagemoto and Yue (1986). We will further address the mathematics of this issue later on, once we have outlined the remaining matrices needed in the calculation of the scatter.

By using \mathbf{T}_{il} to define the scatter as an incident wave, Equation (2.10) can then be expressed as an incident wave (superscript I) on any neighbouring

tube l , located near tube i , as

$$\phi_l^I = \sum_n \left(\phi_0|_{ln} + \sum_{i=1, i \neq l}^N A_{in}^T \mathbf{T}_{il}^n \Psi_{ln}^I \right), \quad (2.24)$$

where the interior sum describes the contribution of all other tubes. To better understand the contribution of all other tubes, the scatter and incident waves must be related through the characteristics of the isolated tube (Kagemoto and Yue 1986). As such there exists diffraction transfer matrices, called here the \mathbf{B} matrix, that relates the incident and scattered wave field for tube l :

$$\mathbf{A}_l = \mathbf{B}_l \mathbf{a}_l, \quad (2.25)$$

where \mathbf{B} is populated through

$$(\mathbf{B})_{pq} = S_{mn}|_{n'}. \quad (2.26)$$

In this case $p = 3n' + m + 2$, $q = 3n + m + 2$, the vector \mathbf{a}_l contains the amplitude of the incident n wave upon tube l and \mathbf{A}_l contains the scatter terms into all n . The incident wave amplitudes (\mathbf{a}_l) are again derived from Graf's addition formula,

$$J_m(k_n^p r_i) e^{im(\theta_i - \gamma_{il})} = \sum_{d=-\infty}^{\infty} J_{m+d}(k_n^p R_{il}) J_d(k_n^p r_l) e^{id(\pi - \theta_l + \gamma_{il})}, \quad (2.27)$$

noting that an m incident wave will be seen as a combination of all other m by any tube that is not located at the origin. It is important to note that the axisymmetric flux tubes create a sparse \mathbf{B} , with no information pertaining to scatter into non incident m modes. Hence, all m - m' scatter is due to off-centre tubes experiencing the incident wave as a combination of m modes.

As with the \mathbf{T} matrix, the \mathbf{a} vector is constructed through Graf's addition formula, and therein lies the symmetry problem. The symmetry break arises due to the nature of the J_m , $H_m^{(1)}$ and K_m functions, of positive and negative m order. For odd m the Bessel J (as well as $H_m^{(1)}$) function behaves like $J_{-m} = -J_m$, and as a result through solving the linear algebra for \mathbf{A}_l no difference arises between $\pm m$. As the far-field components are described by J_m and $H_m^{(1)}$, the matrix procedure of Kagemoto and Yue (1986) then sees no difference in the scattered far-field $\pm m$ waves (when the tubes are aligned with x). However, the Bessel K function is invariant for $\pm m$, yet when multiplied by the variant J_m (which is present in \mathbf{a}_l), terms do not cancel

and thus a difference in the $\pm m$ scattering coefficient arises. By examining the definition of the Bessel K function (see Abramowitz and Stegun 1964, Equation 9.6.4) the exponential factor returns the symmetry of the ± 1 modes when the tubes are aligned along the x axis, whilst remaining an appropriate solution.

Expanding upon Equation (2.24), by utilizing Equation (2.25), completes the picture of the scattered wave field from a flux tube pair:

$$\mathbf{A}_l = \mathbf{B}_l \left(\mathbf{a}_l + \sum_{i=1, i \neq l}^N \mathbf{T}_{il}^T \mathbf{A}_i \right), \quad (2.28)$$

$$\mathbf{A}_1 = \mathbf{B}_1 (\mathbf{a}_1 + \mathbf{T}_{21}^T \mathbf{B}_2 [\mathbf{a}_2 + \mathbf{T}_{12}^T \mathbf{A}_1]), \quad (2.29)$$

$$\mathbf{A}_2 = \mathbf{B}_2 (\mathbf{a}_2 + \mathbf{T}_{12}^T \mathbf{B}_1 [\mathbf{a}_1 + \mathbf{T}_{21}^T \mathbf{A}_2]). \quad (2.30)$$

2.3 The Importance of the Coordinate Origin

The purpose of mathematical models is to emulate a physical system. Observational analysis can then test and judge their validity. In Hankel analysis the observed wave field is decomposed into ingoing and outgoing Hankel functions of order m . The advantage of the formalism outlined in this chapter is that a number of comparisons can be made with the results of such a technique. Hankel Analysis was first used by Braun et al. (1987) and describes the total observable wave field as a sum of ingoing waves ($H_m^{(1)}$) and outgoing waves ($H_m^{(2)}$),

$$\Psi_m(r, \theta, t) = e^{i(m\phi + \omega t)} [A_m(k, \omega) H_m^{(1)}(kr) + B_m(k, \omega) H_m^{(2)}(kr)],$$

where a cylindrical coordinate system (r, θ) is usually used, thereby ignoring the sun's curvature. By using a fully spherical calculation, Bogdan et al. (1993) justifies the use of the above cylindrical approximation by showing that results obtained in both systems are similar. Typically, the analysis of the wave field occurs within an annulus region surrounding the area of interest (i.e. sunspot) centred at a focal point. By comparing the amplitudes of the ingoing (A_m) and outgoing waves (B_m) within this sampling region, the scattering effects of the focal point can be determined.

However, the limitation with using this technique, and our formalism, is that the sampled wave field is assumed to be centred at the focal point or coordinate origin. As such, the amplitudes of both ingoing and outgoing waves may differ by simply moving the coordinate origin a few Mm away.

Figure 2.4 and Table 2.1 show the measured absorption and phase shift from a pair of identical flux tubes, that are moved to different positions around the coordinate origin. Irrespective of the coordinate origin, the degree of scattering between the pair will remain the same. As such, caution must be taken in interpreting the different observed absorption and phase shift as a change in the interaction between the tubes. Rather, the apparent changes in the scattering effects are due to how an m incident wave is interpreted (i.e. Graf's Addition Formula). For example, an incident $m = 0$ wave will not be interpreted as an $m = 0$ wave by a coordinate system centred elsewhere, and vice versa. By changing the focal point or coordinate origin the scattering affects remain the same, but the amplitude of the incident m wave (always centred at the origin) will be different depending upon the distance from the origin. This issue may not be a problem in observational studies as the amplitude of the ingoing waves may be assumed near homogeneous in the quiet sun due to the constant generation of p -modes by granulation across the entire surface. However, the outgoing waves are dependent on the magnetic structure at the focal point. In this formalism both the incident wave and outgoing waves are centred on the origin. Thus a tube will experience different amplitudes of an incident m wave depending on position, and in turn have a different absorption coefficient, despite absorbing the same proportion of m waves it experiences.

While this sensitivity to coordinate origin definition must be treated with caution, it does have its uses. Braun et al. (1990) used the different focal points in the Hankel analysis of an active region. In doing so, spatial maps of the p -mode absorption were built up of the region and the greatest absorption found to coincide with the largest spots of the active region. Absorption maps of plage surrounding these active regions showed smaller values of absorption. As mentioned in the introduction the extent of this observed plage absorption and the contribution of the multiple scattering regime will be addressed by this model.

2.3. THE IMPORTANCE OF THE COORDINATE ORIGIN

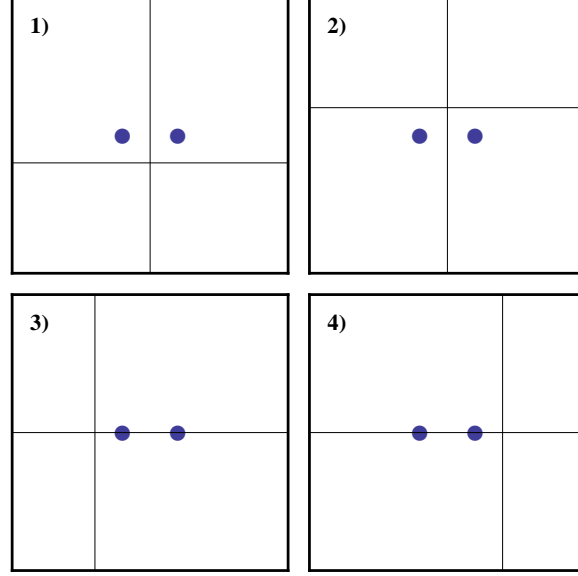


Figure 2.4: The coordinate axis relative to the flux tube pair in 4 cases. By moving the coordinate origin, the apparent scattering effects are changed (see Table 2.1). However, the difference in calculated absorption and phase-shift is the result of different amplitudes of the same incident wave reaching the tubes.

Table 2.1. The observed scattering effects from different coordinate origins (see Figure 2.4)

Case ($\alpha/\Delta\phi$)	$m = -1$	$m = 0$	$m = 1$
1 ($\alpha \times 10^{-2}$)	4.68	6.68	4.68
2 ($\alpha \times 10^{-2}$)	4.68	6.68	4.68
3 ($\alpha \times 10^{-2}$)	4.09	4.26	4.09
4 ($\alpha \times 10^{-2}$)	4.09	4.26	4.09
1 ($\Delta\phi$)	-0.42	-0.65	-0.42
2 ($\Delta\phi$)	-0.42	-0.65	-0.42
3 ($\Delta\phi$)	-0.39	-0.32	-0.39
4 ($\Delta\phi$)	-0.39	-0.32	-0.39

Table 2.2. The absorption coefficient for an isolated tube at the origin

$ m $	$\beta = 0.1$	$\beta = 1$	$\beta = 10$
0	2.16×10^{-4}	2.45×10^{-3}	6.34×10^{-3}
1	3.55×10^{-2}	1.15×10^{-2}	1.18×10^{-3}

2.4 Results

Let us consider the case of two identical tubes (same β and Φ_f), aligned along the x axis and interacting through the sausage and kink modes. For this study we concern ourselves only with the f - f scattering coefficients, as p_n scatter decreases rapidly with increasing n (Bogdan et al. 1996). Upon scattering an incident wave, each tube will also experience the scatter of the other tubes, and in turn produce further scatter. The resultant changes in absorption for the central tube are seen in Figure 2.5, for a mode (m) scattering into an outgoing mode (m). The greatest changes in absorption (on the order of 10^{-4}), for both modes, occur when the tubes are interacting through the near-field, typically on a length scale of half the horizontal wavelength (π/k_p). However, the kink modes demonstrate a sensitivity to the tube's plasma- β , with smaller β tubes readily absorbing more (a magnitude greater) than higher β tubes. Comparison of these changes with the isolated case (Table 2.2), demonstrates that the presence of the second tube alters the isolated absorption coefficient significantly.

Scattering into non-incident ($m' \neq m$) modes is the subject of Figure 2.6. The fraction of energy carried away by these m' modes is greatest when the tubes are close enough to interact through their near-fields. However, as they are separated the energy fraction decreases. The energy fraction also diminishes as the tube separation approaches zero, due to the system returning to an axisymmetric state.

In this model, we have applied a different solution for the jacket modes (Equation 2.21) in an attempt to restore symmetry between $\pm m$ modes. As a result the apparent symmetry breaking between $m = \pm 1$ (Hanasoge and Cally 2009), when the tubes are aligned along x , is absent. Scattering into their respective modes is identical for both the $+1$ and -1 modes (see two top panels of Figure 2.5). However, as the second tube is rotated around the origin, the symmetry is broken and a difference in absorption arises between

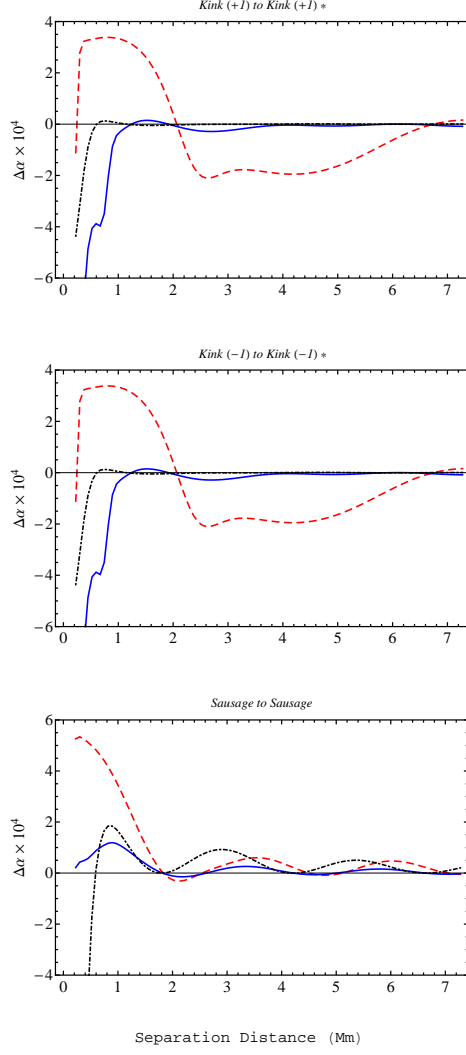


Figure 2.5: The change in absorption coefficient ($\Delta\alpha = \alpha - \alpha^{\text{isolated}}$) (of the central tube only) of an incident m wave due to the presence of a nearby tube for varying separation distances and β . The 3 mHz ($\lambda = 4.9$ Mm) f -mode interacts with an identical pair of flux tubes, aligned along the x -axis ($\beta = 0.1$: Dashed, $\beta = 1$: Solid, $\beta = 10$: Dot Dashed). Frames specified by * have the $\beta = 0.1$ absorption scaled down by factor 10 for clarity in near-field contribution. The absorption coefficients are calculated from Equation (2.13). In all panels the central tube's absorption is dramatically altered (compared with the single tube absorption listed in Table 2.2) when interacting with the nearby tube through the near-field.

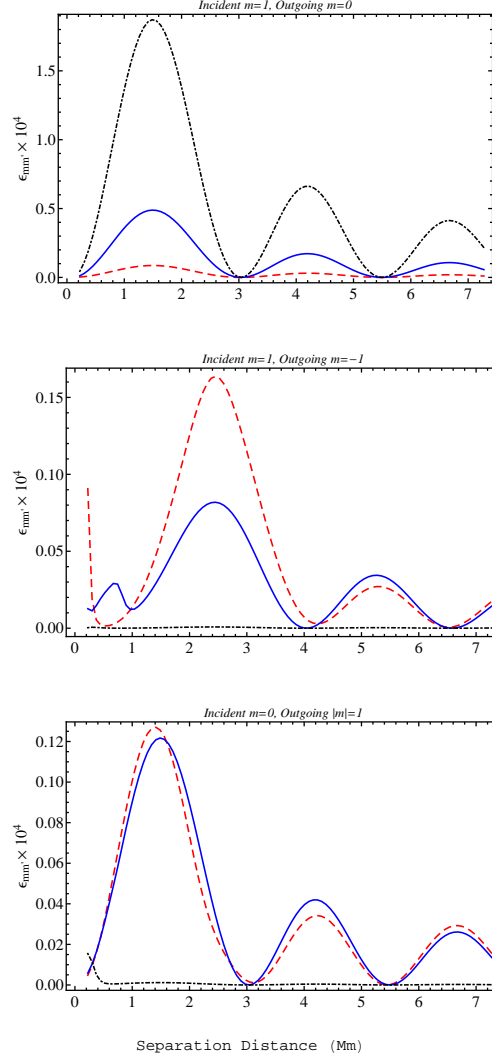


Figure 2.6: The fraction of energy ($\epsilon_{mm'}$) that is scattered into non-incident m' modes by a pair of identical tubes for varying separation distances and β . The 3mHz ($\lambda = 4.9\text{Mm}$) f -mode interacts with an identical pair of flux tubes, aligned along the x -axis ($\beta = 0.1$: Dashed, $\beta = 1$: Solid, $\beta = 10$: Dot Dashed). All $\beta = 0.1$ energy fractions are scaled down by factor 10 for clarity of the near-field contribution. Scattering into kink modes is strongest when the tubes have a small plasma- β . The energy fraction is calculated from Equation (2.15).

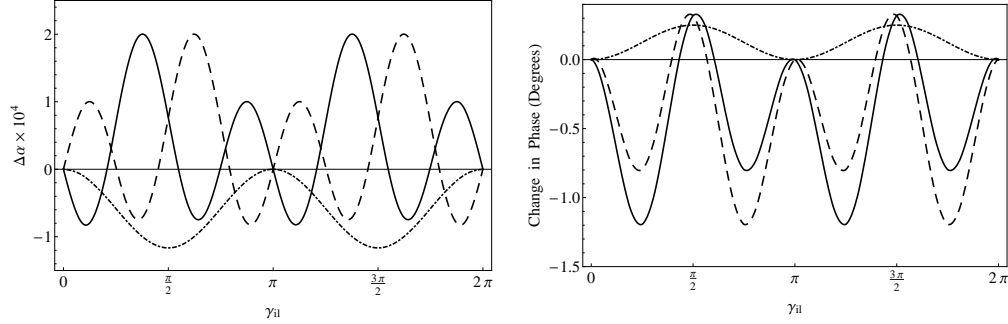


Figure 2.7: The change in absorption and phase of the central tube, as the second tube is rotated around the origin at a distance of 500 km. The incident m modes (solid: $+1$, dashed: -1 , dot-dashed: 0) scatter off the second tube producing a change in the central tube. Symmetry between the ± 1 modes is restored when the second tube is aligned on the x -axis ($\gamma_{il} = 0, \pi$). Whilst the $m = 0$ mode is axisymmetric a change occurs when the second tube is rotated about the origin, due to the kink mode scatter being absorbed as sausage mode components (see Equation 2.27).

the -1 and $+1$ modes (Figure 2.7). With regards to the sausage mode, this mode naturally has no preference between which kink mode to scatter into (see bottom panel of Figure 2.6).

Expanding our view to the complete scattered wave field, rather than that of the central tube, reveals the collective nature of a pair of flux tubes. Akin to the central tubes absorption (and Hanasoge and Cally (2009), despite the change to the jacket solution), the absorption of the flux tube pair varies greatly when allowed to interact through their respective near-fields (Figure 2.8). The changes in absorption are again significant when compared to the non-interacting tube's absorption coefficient (Table 2.2), returning to an isolated absorption coefficient when sufficiently far apart. Additionally, at higher frequencies incident waves are more readily absorbed by the tubes. However, due to a shorter wavelength the pair need to be closer (in comparison to lower frequencies), to interact through their respective near-fields. The affects of the proximity thus manifests itself in an altered absorption coefficient, and hence the tubes no longer absorb and scatter as two unique isolated tubes but rather as a collective scatterer. The impact of this collective behaviour is also evident in the phase of the outgoing scattered wave field (Figure 2.9). The sensitivity of the phase with tube separation (Hanasoge and Cally 2009) is not present here, with coherent changes in phase as the tubes are separated. The greatest changes in phase generally occur

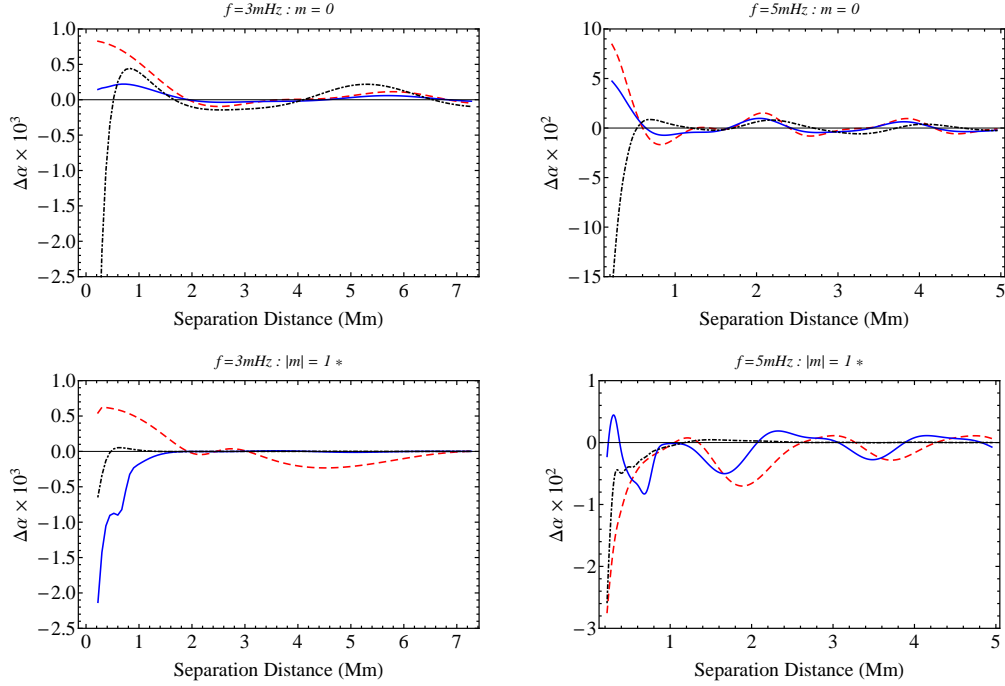


Figure 2.8: The change in absorption ($\alpha - \alpha^{\text{isolatedpair}}$) of an identical pair aligned along the x -axis. Absorption is generally enhanced within the near-field, slowly returning to isolated values as the tubes are separated. Left Panels: Comparison with Table 2.2 reveals the absorption of the pair is enhanced compared to that of the central tube. The pair behave collectively. Line types as in Figures 2.5 and 2.6.

in the kink modes with the higher frequency incident waves also aiding in an increased change in phase. The near-field interactions are the cause of the greatest phase changes, with the impact on travel times increasing with proximity.

2.5 Discussion and Conclusions

While the results presented here are informative about m mode interactions, we must first discuss limitations of the model before considering their significance. In truncating the polytrope, we reduce the number of jacket modes from a continuous spectrum to a discrete one. The nature of the finite-depth interaction theory of Kagemoto and Yue (1986), requires the use of this discrete spectrum, but how much does the scatter differ when the polytrope is allowed to extend to infinite depth? In numerical simulations the jacket modes appear naturally, but these simulations are restricted in spatial reso-

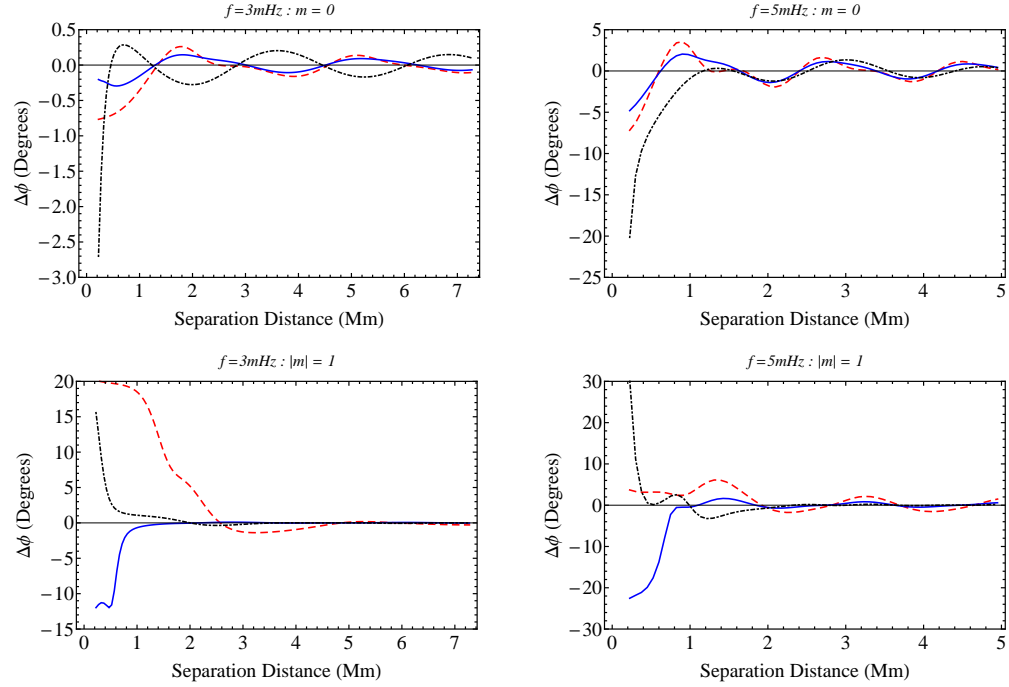


Figure 2.9: The change in phase of the scattered wave field from the pair, compared to that of two isolated tubes. Large phase changes are seen in the near-field, rapidly returning to isolated values as the tubes are separated beyond a wavelength of the incident mode. Kink mode scattering (bottom panels) produces the largest change in phase with high frequency also to the contributing the increased phase changes. Smooth changes in phase occur as the tubes are separated, contrasting the results of Hanasoge and Cally (2009). Line types as in Figure 2.5 and 2.6.

lution. By treating the jacket eigenfunctions analytically, we are not as easily restricted by spatial resolution, and can consider their impact. In taking a large enough subset of the jacket modes the eigenfunctions of the tube are mimicked. However, attributing results from a partial basis to a complete picture must be done cautiously. The second limitation is the use of the thin tube approximation. Whilst completely valid below z_0 , how much are we underestimating the degree of scatter from higher order fluting modes present above z_0 ? Felipe et al. (2013) performed numerical studies of thick interacting tubes (capable of $m \geq 2$ modes), showing that whilst the sausage and kink modes are the dominant modes for scatter, the contribution of higher modes is not negligible. Recognizing this, we note that this simplified model is not perfect in modelling realistic interactions between tubes that have a comparable thickness to the incident wavelength. Nevertheless, it is a helpful tool for parameter searches to characterize the multiple scattering regime.

Having stated these limitations let's consider our adjusted near-field solution. As discussed previously, the difference between $m = \pm 1$ modes is the definition of the coordinate system. The near-field solution of Kagemoto and Yue (1986) presents a symmetry problem for tubes interacting through $\pm m$ modes. Whilst the Bessel K solution for the scattered jacket modes is accurate, the invariant nature of K_m (in contrast to $H_m^{(1)}$ and J_m) between $\pm m$ leads to symmetry breaking in the calculation of Equation (2.29). Our Bessel K solution (Equation 2.21), which is a valid solution for the jacket modes, has restored the scatter symmetry when the tubes are aligned along x . This solution maintains the sensibility that $m = \pm 1$ modes differ only through a coordinate system definition, and not through their respective scatter. Consequently, without this new solution the interaction theory would stipulate that the $m = 0$ mode (being axisymmetric) would show preferential scatter into $\pm m$ modes. We also note that the incoherent phase changes as the tubes are separated, found by Hanasoge and Cally (2009), are absent in these results. This is again due to the previous near-field solution. Our results show coherent changes in phase as the tubes are separated, which is consistent with the changes in phase of Felipe et al. (2013).

Interestingly, by moving the off-centre tube to a position where $\gamma_{il} \neq 0$, the symmetry is no longer maintained (Figure 2.7). The $e^{im\theta}$ dependence of $m \neq 0$ waves creates a symmetry break between modes (when $\gamma_{il} \neq 0$), owing to unequal amounts of $\pm m$ waves at the second tube. Therefore, a difference in the scatter coefficient of the $m = \pm 1$ modes arises at the second tube, and in turn a difference at the centred tube also occurs. The sensitive nature of the scatter to the tube position, was also shown independently by

Felipe et al. (2013) and Daifallah (2014) in numerical studies for incident plane waves. This sensitivity outlines another parameter to consider in the determination of an ensemble's constitution. Changes in the sausage mode occur when the second tube is rotated around the origin, due to the second tube scattering kink modes. In turn the central tube absorbs $m = 0$ modes (as per Equation 2.27). The absorption of all modes is identical if the origin is relocated to the centre of the second tube (i.e. $\gamma_{il} = \pi$), and this serves as a reasonable check for the coordinate system definitions.

The inclusion of the sausage mode in this model highlights its importance in the multiple scattering regime. The change in absorption for the sausage mode is of the same magnitude as the kink modes for the 3 mHz case (Figure 2.5), owing to the fact that the off centre tube experiences any incident m wave as a combination of m modes, and in turn scatters significantly into both sausage and kink. However, in the higher frequency (5 mHz) case the absorption of the sausage mode is a magnitude larger than that of the kink modes when the tubes are in close proximity (see right panels of Figure 2.8). These results are consistent with Felipe et al. (2013), which illustrated that high frequency cases will produce larger absorption changes for the $m = 0$ modes than for the $|m| \geq 1$ modes. With respect to the phase shift of the individual m modes (Figure 2.9) the close proximity of tubes generally enhances the negative phase shift of the sausage mode (Hindman and Jain 2012), which results from shorter travel distances due to reflection from tube boundaries. Akin to the absorption, the phase shift of the sausage modes is enhanced by the higher frequency incident waves becoming comparable to the phase shift generated by kink modes. Figure 2.9 illustrates that close proximity and higher frequency incident waves may enable the phase shift produced by $m = 0$ waves to surpass that of the kink modes in some cases (such as thicker tubes), as anticipated by Felipe et al. (2013).

The desire to determine the properties of magnetic ensembles from the scattered wave field results from the inability to directly discern the internal constitution of magnetic features. Observational techniques to determine the amplitude and phase of scattered waves from small magnetic elements exist (see Duvall et al. (2006)), but which parameters govern the mechanisms that affect the scattered wave field? The multiple scattering regime is well known to alter the scattered wave field (Bogdan and Zweibel 1987; Keppens et al. 1994), and cannot be approximated by single scattering. Numerical studies have begun to characterize this regime (Felipe et al. 2013; Daifallah 2014), and we have presented here a more complete semi-analytical model to aid in the determination of these parameters. It has been demonstrated that

scattering effects are sensitive to both the proximity and relative position of nearby tubes. The inclusion of the sausage mode has also illustrated the significance of the scattering between m modes, especially within the near-field. In more detailed cases the model presented here can be used to address the scattering between thin tubes, like those present within plage. In the following chapter, we will apply the formalism developed here to address the interactions of multiple non-identical tubes in regular and random ensembles.

Monash University

Declaration for Thesis Chapter 3: The Scattering of Acoustic Waves From Ensembles of Thin Magnetic Flux Tubes

Declaration by candidate

In the case of Chapter 3, the nature and extent of my contribution to the work was the following:

Nature of contribution	Extent of contribution (%)
Key ideas, development of code, modelling, production of all results, writing of paper.	80

The following co-authors contributed to the work. If co-authors are students at Monash University, the extent of their contribution in percentage terms must be stated:

Name	Nature of contribution	Extent of contribution (%) for student co-authors only
Paul Cally	Supervision and guidance	

The undersigned hereby certify that the above declaration correctly reflects the nature and extent of the candidate's and co-authors' contributions to this work*.

Candidate's Signature		Date 13/10/2014
------------------------------	---	---------------------------

Main Supervisor's Signature		Date 13/10/2014
------------------------------------	---	---------------------------

*Note: Where the responsible author is not the candidate's main supervisor, the main supervisor should consult with the responsible author to agree on the respective contributions of the authors.

Chapter 3

The Scattering of Acoustic Waves from Ensembles of Thin Magnetic Flux Tubes

Motivated by the observational results of Braun (1995), we extend the model described in Chapter 2 to address the effect of multiple scattering of f and p -modes by an ensemble of thin vertical magnetic flux tubes in the surface layers of the Sun. As in Hankel analysis, we measure the scatter and phase shift from an incident cylindrical wave in a coordinate system roughly centred in the core of the ensemble. It is demonstrated that although thin flux tubes are unable to interact with high order fluting modes individually, they can indirectly absorb energy from these waves through the scatters of kink and sausage components. It is also shown how the distribution of absorption and phase shift across the azimuthal order m depends strongly on the tube position, as well as on the individual tube characteristics. This is the first analytical study into the multiple scattering regime of magnetic tube ensembles embedded within a stratified atmosphere.

3.1 Introduction

As discussed in the previous chapter, the solar surface is threaded with thin magnetic filaments that often appear at granule or supergranule boundaries, or more prominently as massive ensembles (plage) associated with active regions. These filaments may be modelled as isolated thin flux tubes embedded within a field free plasma, interacting strongly with the solar acoustic p -modes and the surface gravity f -mode, both absorbing and scattering wave energy. Their seismic signature is a powerful constraint on models of solar surface structure and magnetism.

So far no analytical study has examined multiple scattering within an ensemble with gravity. However, a growing body of numerical studies has begun to shed light on the significance of this regime. Felipe et al. (2013) showed that the multiple scattering regime significantly impacts absorption coefficients, as well as generally decreasing the phase shift of the outgoing wave. It was also noted that the absorption generally increases with the number of tubes. Daifallah (2014) recently investigated the surface velocity profiles created by closely packed thin tube ensembles, showing that relative tube position and separation plays a significant role in the resultant vertical velocity profiles.

In the previous chapter, we applied a slightly modified version of the Kagemoto and Yue (1986) formalism to the interactions of f modes with a pair of flux tubes (p -modes were included in the mathematical development, but were not investigated in detail because of their much weaker scattering). We restricted attention to the sausage and kink motions of the tube ($|m| \leq 1$), as the mathematical thin tube approximation does not support higher order fluting modes. In this paper we focus on the interactions between tubes that constitute a larger ensemble. In particular we are interested in the absorption and phase shift that can be determined from the outgoing cylindrical wave. Section 3.2 will outline the mathematical formalism important to this study, with Section 3.3 presenting the results. Discussion and conclusions are given in Section 3.4, with particular reference to the effect of the multiple scattering regime on measurable outgoing parameters. Higher order m modes are included because they do interact with extended ensembles.

3.2 Ensemble Scattering Formalism

In this section we outline the scattering of various azimuthal modes (characterized by integer m) from an ensemble of flux tubes. The formalism for the propagation of f -modes and their interaction with a pair of thin flux tubes is outlined in detail in Chapter 2. For the purpose of this study, we only mention the key parts of the formalism required to extend the model to an ensemble of arbitrarily positioned non-identical tubes.

Consider a random assortment of vertical flux tubes embedded within a field free atmosphere. Again, the atmosphere used here is a stratified adiabatic truncated polytrope (adiabatic index $\gamma = 5/3$), with constant gravity. In such an atmosphere, the complete acoustic wave field (Ψ) will consist of three components:

$$\Psi = \Psi_{\text{inc}} + \Psi_{\text{sca}} + \Psi_{\text{int}}, \quad (3.1)$$

where inc, sca and int specify the incident, scattered and internal wave fields, respectively. In the presence of magnetic filaments, an incoming f - or p -mode (Ψ_{inc}) will interact with each flux tube, and in turn be scattered back into the external medium (Ψ_{sca}). The fraction of energy that is scattered forms a wave field of radially propagating modes, while the remainder of the incident wave energy is transported vertically along the tube axis (Ψ_{int}). Being a stratified atmosphere, Ψ_{sca} describes both the scattered propagating and evanescent waves (Bogdan and Cally 1995).

In Hankel analysis (Braun et al. 1987, 1988, etc) the incoming and outgoing waves are determined by observing the waves within an annulus centred at a specific point. For comparative purposes we define the incoming and outgoing wave in Equations (2.13–2.14) as waves centred at the coordinate origin.

In the case of two tubes (Hanasoge and Cally 2009; Hanson and Cally 2014), a single tubes scatter coefficients (\mathbf{A}_l) can be easily calculated using a linear solve algorithm by rearranging Equation (2.28). We extend the interaction between tube pairs to N multiple tubes, through the scattering equation:

$$\left[\mathbf{I} - \sum_{i \neq l, l=1}^N \mathbf{B}_l \mathbf{T}_{il}^T \mathbf{B}_i \mathbf{T}_{li}^T \right] \mathbf{A}_l = \mathbf{B}_l \left(\mathbf{a}_l + \sum_{i \neq l, l=1}^N \mathbf{T}_{il}^T \mathbf{B}_i \mathbf{a}_i \right). \quad (3.2)$$

In this way we have calculated the exact \mathbf{A} solution for N tubes. Similar studies (e.g Felipe et al. 2013)) restrict the number of scatters between tubes mimicing a complete scattered wave field within the ensemble. Figure 3.1

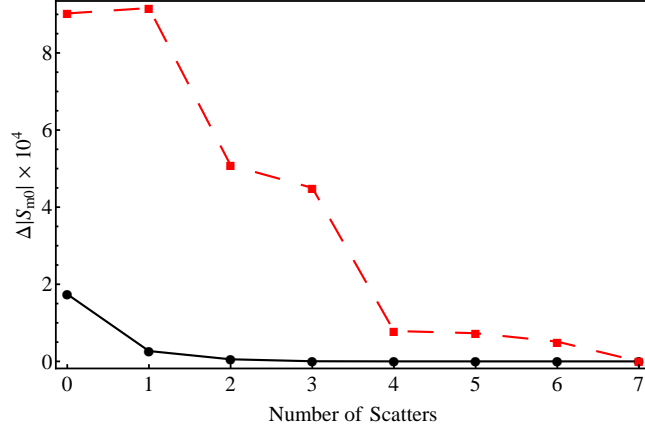


Figure 3.1: The change in the scattering coefficient as the permitted number of scatters between tubes is increased. The $m = 0$ (black) scatter coefficient converges quickly within 2–3 scatters, while the $|m| = 1$ wave (red dashed) is not as quick to converge.

shows the change in the scattering coefficient from the exact solution as the number of scatters increases. The $m = 0$ scattering coefficient converges rapidly within three scatters, whilst the $|m| = 1$ mode converges less quickly within seven scatters.

3.2.1 The Interaction of Higher Order m Modes within Ensembles

The Hankel analysis of plage (Braun 1995) has shown measurable non-zero absorption coefficients for $|m| > 1$ waves. Due to the implementation of the thin tube approximation, we only permit the interaction of $|m| \leq 1$ waves with the tubes. This is a consequence of the thin tube approximation. Any higher order m incident waves will not interact with the individual tubes, resulting in the scattering coefficient for that tube vanishing. Relating to Equation (3.1), the total wave field after a fluting mode ($|m| > 1$) interacts with a thin tube located at the origin will have a zero Ψ_{sca} and Ψ_{int} terms,

$$\Psi = \Psi_{\text{inc}}. \quad (3.3)$$

Consequently, the incident wave leaves the system unaffected by the thin tube. However, Graf's addition formula (Equations 2.27) defines an m mode by the coordinate origin. Any fluting mode defined with centre at the origin is experienced as a mixture of all other m modes by any tube that is not located at the origin. Thus, as a fraction of the incident wave's energy is

scattered by off-centre tubes through $|m| \leq 1$ interactions, the amplitude of the outgoing wave will be altered, despite the tubes being unable to interact with pure $|m| > 1$ modes. In terms of an energy budget, the scattering from an off-centre tube of $|m| \leq 1$ components reduces the outgoing power of the fluting modes.

With regards to the formalism of Kagemoto and Yue (1986), the \mathbf{T}_{il} and \mathbf{a}_l are expanded to be fully populated for a larger $|m|$ set of modes. The interaction of the tubes with fluting modes depends solely on the terms in the \mathbf{B} matrix. Since the tubes do not scatter these higher order modes, the coefficients that populate \mathbf{B} and correspond to $|m| > 1$ will simply be zero. In doing this, there will be no scatter from an isolated tube located at the origin for a $|m| > 1$ wave,

$$\mathbf{A}_l = \mathbf{B}_l \mathbf{a}_l = \mathbf{0}. \quad (3.4)$$

However, as \mathbf{T}_{il} is fully populated (and \mathbf{a}_l for off-centre tubes) energy transfer from a $|m| > 1$ wave to the tube is possible through kink and sausage components seen by off centre tubes. In a closely packed ensemble any scatter from the tube at the origin will purely be due to neighbouring tubes:

$$\mathbf{A}_l = \sum_{i=1, i \neq l}^N \mathbf{B}_l \mathbf{T}_{il}^T \mathbf{A}_i. \quad (3.5)$$

3.3 Results

3.3.1 Symmetry Studies

Let us consider ensembles of identical flux tubes, all with uniform plasma- $\beta = 1$, that are symmetrically placed around the coordinate origin. In all these cases we have allowed Graf's formula to range over $|m| \leq 4$ to demonstrate the non-zero scattering of fluting modes. The incident wave is a f -mode of order m , with a wavelength of $\lambda = 4.9$ Mm and frequency 3 mHz. A large discrete subset of jacket modes is chosen to mimic the continuum of modes present in an infinitely deep atmosphere. We define the change in absorption ($\Delta\alpha$) and in phase ($\Delta\varphi$) to be the difference between the values obtained when the tubes are interacting, and when they are not.

We begin by extending the model of Hanson and Cally (2014) to three tubes aligned along the x axis and centred upon the origin. In this ensemble we have two cases. Firstly, the tubes are positioned at $x = 0$ and $\pm 0.2\lambda$, which is close enough for near field interaction. In the second case, 1.5λ is the separation distance between them. At this distance, the tubes are far

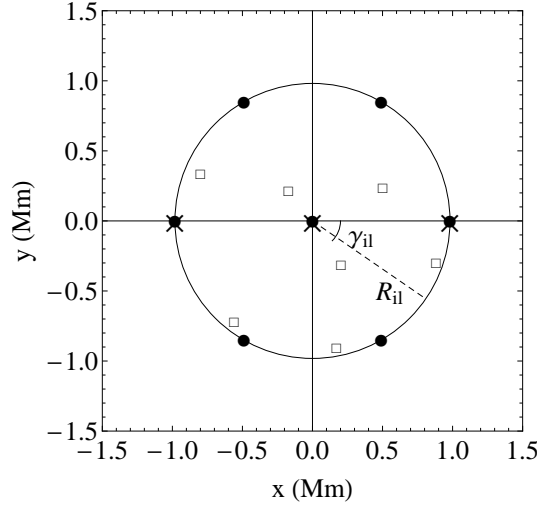


Figure 3.2: The tube positions for all ensembles in this study. The dot points represent the positions of the 7 tube ensemble, as well as the six tube ensemble with the tube located at (0,0) absent. The crosses specify the positions of the three tubes ensemble (that are separated by 0.2λ), while the squares indicate the positions of the tubes within the randomly positioned ensembles. The separation parameters R_{il} and γ_{il} are also represented. The large circle highlights the 1 Mm radius circle, inside which the random tubes cases are positioned.

enough apart to only interact through the far-field. The resultant absorption and phase shift for both cases are seen in Figure 3.3. In each case, the absorption coefficient and phase shift peaks for $|m| \leq 1$ incident waves, with the peaks being greatest for the near-field interaction case. If we compare both cases to their respective non-interacting coefficients¹, the changes in the absorption and phase shift become negligible when only interacting through the far-field. The changes in absorption for the near-field interacting triplet are of the order 10^{-2} compared to that of the isolated cases. However, when interacting through the far-field, the changes are of the order 10^{-3} . This difference between the near- and far-field cases can also be seen in the phase changes. We conclude for this first ensemble set that for $|m| > 1$ waves, the scattering is non-zero despite the tubes not directly interacting with these waves. However, these scattering effects rapidly diminish as $|m|$ increases.

Extending the model to a larger ensemble, we also investigate the case of many tubes positioned evenly around a circle of radius 0.2λ . In particu-

¹ Here we mathematically allow only a single scatter off each tube by neglecting the \mathbf{T}_{il}^n terms in Equation (2.24).

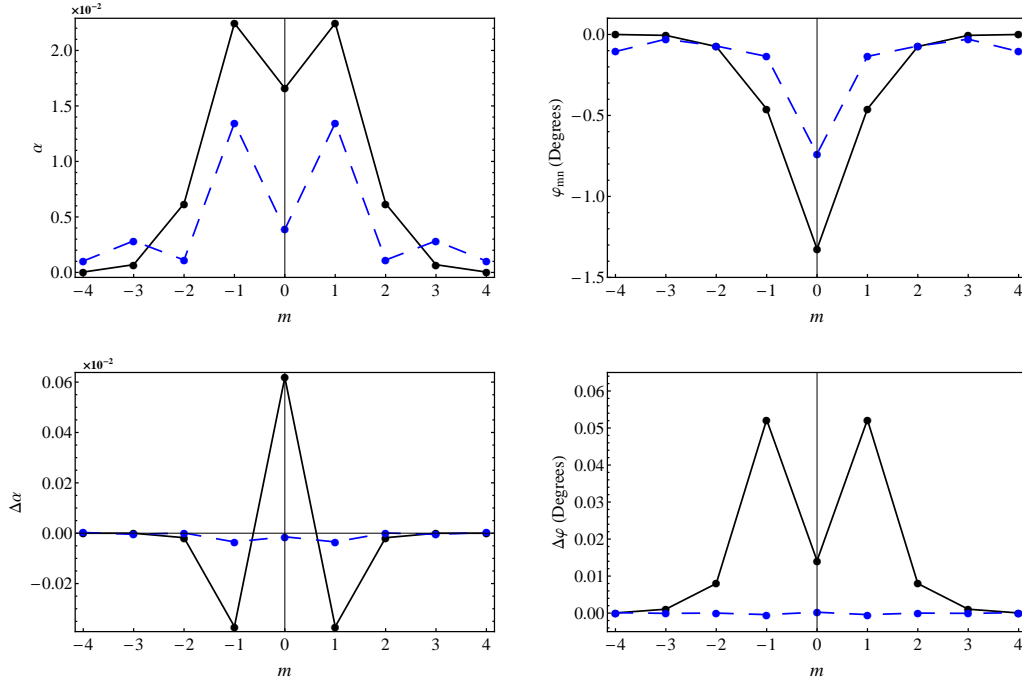


Figure 3.3: The absorption and phase shift of the outgoing f -mode for three tubes aligned along the x axis, centered on the origin and separated by 0.2λ (Black) and 1.5λ (Blue Dashed), where $\lambda = 4.9$ Mm. The top panels show the absorption and phase shift of an incident m wave when the three tubes are interacting. The bottom panels show the difference in scattering between interacting and non-interacting tubes. The change in absorption and phase is large when the tubes are interacting through the near field, but when far apart the interaction between the tubes is insignificant to the resultant outgoing wave.

lar we examine two similar ensembles, see Figure 3.2. Firstly, six tubes are positioned on the circle, with the tube centers mapping out the vertices of a regular hexagon. In the second ensemble, a seventh tube is also positioned at the coordinate origin, as in Daiffallah (2014). The affects of the seventh tube within the circle of tubes is seen in Figure 3.4. In each ensemble the absorption and phase shifts have slightly differing behavior for all m . The seventh central tube acts to increase the absorption of the ensemble for $|m| \leq 1$, but only enhances the phase shift of the $m = 0$ wave. However, in comparison to their respective non-interacting values, the six tube case sees greatest change in absorption for $|m| \leq 1$ waves, while the seven tube ensemble only peaks at $m = 0$. The change in phase shift is significant for $|m| \leq 3$ for both ensembles, with the seven tube case experiencing a greater change. Comparison to the three tube ensemble shows that the absorption and phase shift are of the same magnitude. However, comparing the change in scattering properties from the non-interacting tube cases demonstrates that the larger ensembles experience a change in both phase and absorption, that is an order of magnitude larger than the smaller three tube ensemble.

Within the solar atmosphere, as well as in this model, the scattering between tubes is not just restricted to the order (m, n) of the incident wave. In fact the tubes may scatter into all other m' and n' wave components. The fraction of outgoing energy that is transferred from a p_n to a $p_{n'}$ wave, for the above mentioned seven tube ensemble, is seen in Figure 3.5. The plot is similar to Figure 3 of Hindman and Jain (2012) (for the $m = 0$ mode), demonstrating that for both the sausage and kink modes the energy fraction diminishes with increasing n' . The greatest energy transfer occurs with waves that are scattering from or to an f mode. Furthermore, Table 3.1 shows the energy fraction of the outgoing wave components (m') from an incident positive m . The strongest scattering is into the incident mode ($m' = m$), which is due to the $\delta_{mm'}$ in Equation (2.15). Interestingly, due to the symmetry of the system, the scattering of an even m is restricted to even m' components, and vice versa for odd m .

3.3.2 Random Ensembles

While symmetry studies are useful in determining some characteristics of ensembles that affect absorption and phase, we are also interested in how the random nature of an ensemble affects measurable parameters. We have built three ensembles, from which we will examine the effect of random positions, as well as various tube characteristics. The first ensemble is of seven identical

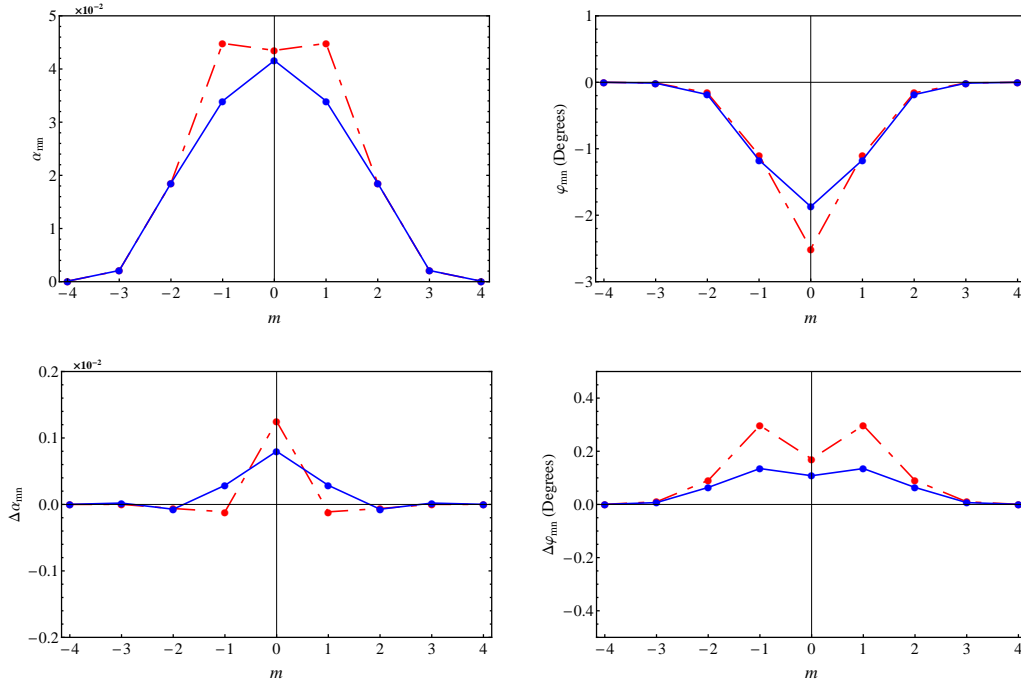


Figure 3.4: The absorption (left) and phase of the outgoing wave (right) from a hexagonal ensemble of seven tubes (red dashed) and six tubes (blue). The scattering coefficient examined here is the f - f coefficient. Six tubes are 0.2λ from the origin, with the seventh tube located at the center. The hexagonal distribution is symmetric and hence has symmetry between $\pm m$ modes. The addition of the seventh tube acts to increase absorption and shift the phase further to the negative, while also reducing $\Delta\alpha$ for the $m = \pm 1$ modes.

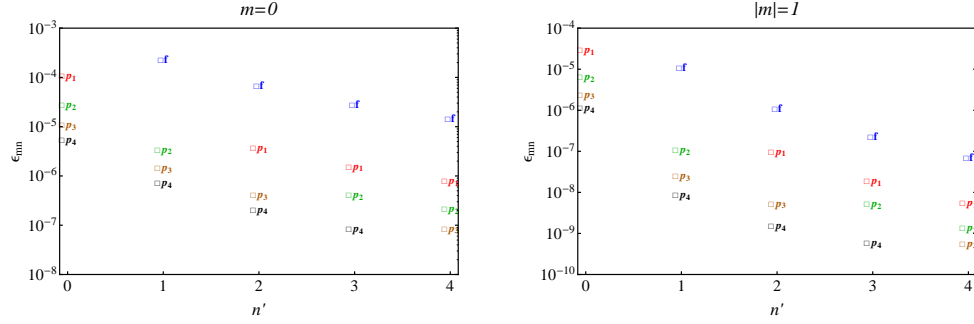


Figure 3.5: The energy fraction (Equation 2.15) of the outgoing $p_{n'}$ from the seven tube hexagonal case, with an incident p_n mode of frequency 3 mHz. The scattering is strongest when involving the f mode, with the energy rapidly diminishing with increasing n for both the sausage and kink modes. The color and small label indicate the nature of the incident wave (f , p_1 , \dots), the horizontal position indicates the scattered wave (for the incident m only), and the vertical position represents the fractional energy in the scattered mode (logarithmic scale). The outgoing energy fraction in the original mode is not shown as it is nearly 1 in all cases.

Table 3.1. The energy fraction ϵ_{mn} of outgoing wave components m'

m'	$m = 0$	$m = 1$	$m = 2$	$m = 3$	$m = 4$
-4	4.3×10^{-9}	...	7.8×10^{-9}	...	1.5×10^{-13}
-3	...	1.6×10^{-7}	...	1.3×10^{-8}	...
-2	2.0×10^{-7}	...	5.7×10^{-6}	...	7.8×10^{-9}
-1	...	1.6×10^{-6}	...	1.4×10^{-7}	...
0	9.5×10^{-1}	...	3.5×10^{-8}	...	5.4×10^{-9}
1	...	9.5×10^{-1}	...	7.0×10^{-10}	...
2	2.0×10^{-7}	...	9.8×10^{-1}	...	1.8×10^{-11}
3	...	1.2×10^{-8}	...	9.9×10^{-1}	...
4	4.3×10^{-9}	...	1.2×10^{-10}	...	9.9×10^{-1}

Note. — The energy fraction (Equation 2.15) of an outgoing m' wave, produced by an incident $+m$ wave. The dominant diagonal (bold face) appears for cases where $m' = m$. The symmetry of the seven tube system forces the system to scatter into even m' , for an incident even m wave. This is also the case for odd m . If the incident wave was of order $-m$ the results would be reversed about $m = 0$.

$\beta = 1$ tubes, positioned randomly within 1 Mm of the origin. The second and third ensembles are identical in tube placement to the first, but have a selection of different β .

In the first ensemble (randomly distributed identical tubes), three cases are studied for the incident wave frequencies of 3, 4 and 5 mHz. The resultant absorption and phase shift can be seen in Figure 3.6. The largest scattering effects in both outgoing values and change from isolated values are seen in higher frequencies. The higher frequency waves also act in highlighting differences in the absorption coefficients between $\pm m$. As the tubes are not symmetrical around the origin a difference in absorption appears between $\pm m$. Interestingly, the $\pm m$ modes have no apparent difference in the phase shift. Similarly to the previous ensembles, the scattering coefficients peak at $|m| \leq 1$ and rapidly decrease with increasing $|m|$.

The scattering effects of the second and third ensembles of non-identical flux tubes is shown in Figure 3.7. Two cases are explored here, both with different selections of plasma β (see Table 3.2), to which we compare the values of the identical tube ensemble. In both these cases the differing β amongst the ensemble acts in enhancing the overall absorption, in comparison to the identical ensemble case. However, the changes from the non-interacting ensemble demonstrates that depending on the β of the tubes present, the distribution of $\Delta\alpha$ can be very different across m . With regards to the phase, one ensemble shows increased negative phase shift, while the other shows a slightly diminished phase shift from the identical ensemble case. The change in phase from isolated values supports this, showing that the multiple scattering between the tubes enhances this difference. We note here that while higher frequencies could not reveal the difference in phase across $\pm m$, the random distribution in β highlights that a difference does exist (even if it is very small).

We conclude this section by exploring how the scattering coefficient changes with an increasing number of flux tubes within 2.5 Mm of the origin. The tubes are identical, randomly distributed and each additional tube is added to the ensemble without moving the others. Figure 3.8 shows the absorption and phase shift for increasing tube numbers for both incident $m = 0$ and $m = 1$. The addition of each tube generally increases the absorption, as well as the negative phase shift. Although each added tube is randomly placed, the absorption varies in a rough linear relationship with tube number, and similarly with the phase shift for $m = 1$. However, the phase shift of the $m = 0$ wave seems to depend quite sensitively on tube position, resulting in a more irregular dependence on tube number.

Table 3.2. The tube position and corresponding β for the three random ensembles of seven fluxtubes.

x (Mm)	y (Mm)	β (Case 1)	β (Case 2)	β (Case 3)
0.17	-0.90	1	1	10
0.20	-0.30	1	5	0.5
0.50	0.25	1	0.5	5
-0.17	0.23	1	1	0.1
-0.56	-0.70	1	0.1	1
-0.80	0.35	1	1	0.1
0.82	-0.29	1	0.1	0.5

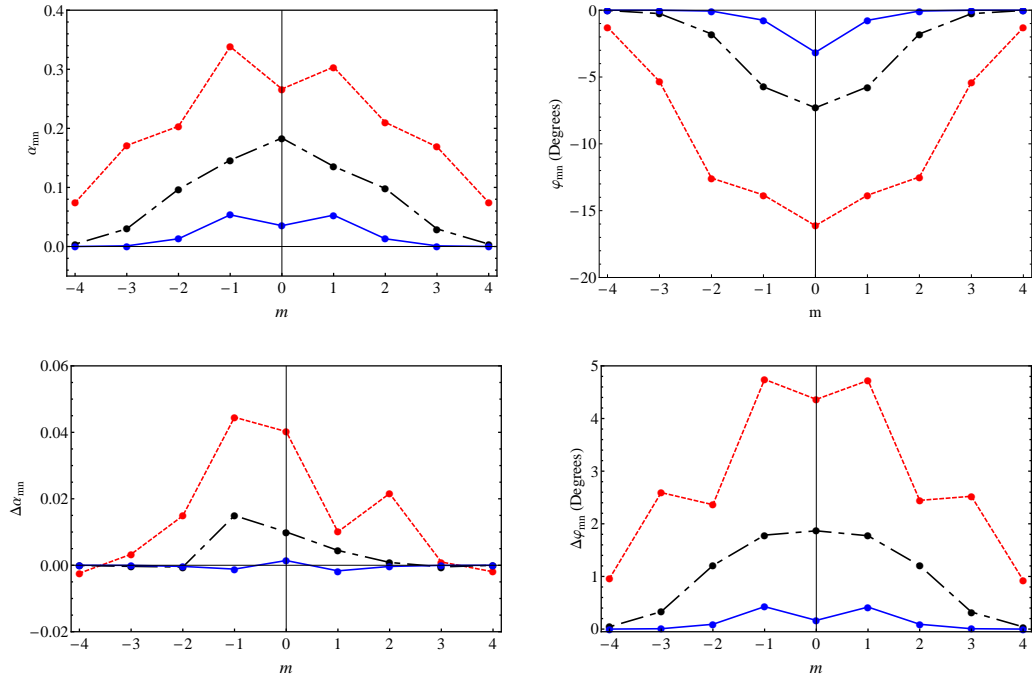


Figure 3.6: The absorption and phase from an ensemble of seven randomly positioned identical ($\beta = 1$) tubes. Again we investigate f - f mode scattering. The incident wave (blue solid: 3 mHz, black dot-dashed: 4 mHz, red dashed: 5 mHz) is scattered differently by the ensemble for different frequencies. The degree of absorption and phase shift is generally increased by higher frequency waves. The absorption of the incident wave is not symmetric for $\pm m$ modes, as the assortment is randomly positioned around the coordinate origin. However, the phase shift appears to be symmetrically distributed across m .

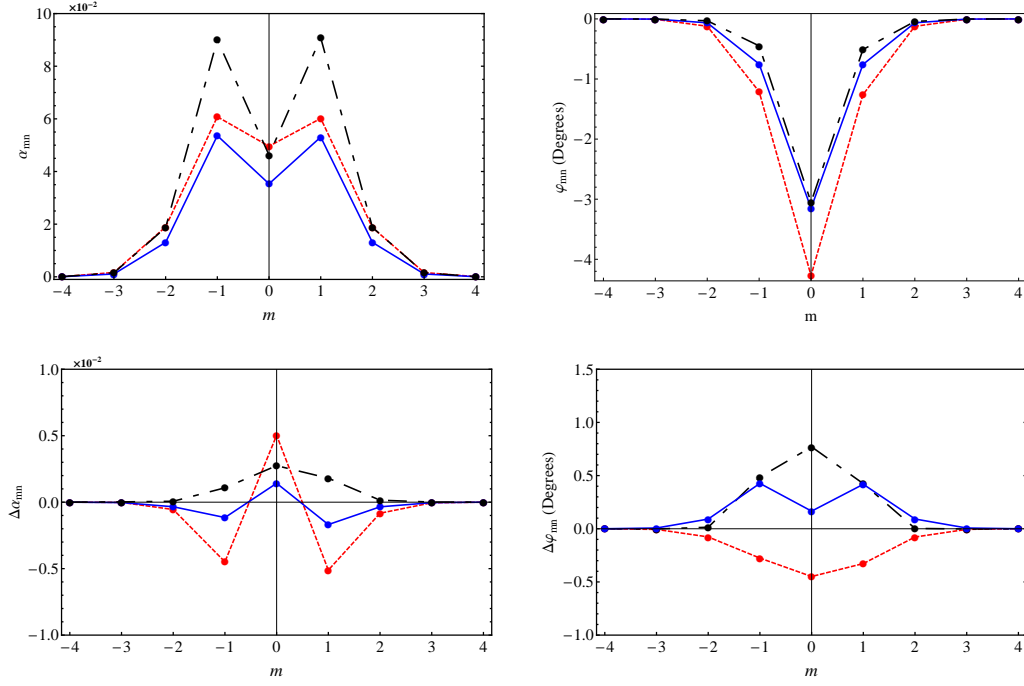


Figure 3.7: The absorption and phase from an ensemble of identical tubes (blue) and two random non-identical ensembles (red dashed and black dot-dashed). The tube positions are identical to those of Figure 3.6, but vary in β . The incident wave is a f -mode of 3 mHz and all of the tubes reside within 1 Mm of the origin. The absorption and phase are distributed differently across m and are strongly dependent upon the individual tubes present. Differences in phase for $\pm m$ are more apparent when the tubes are non-identical.

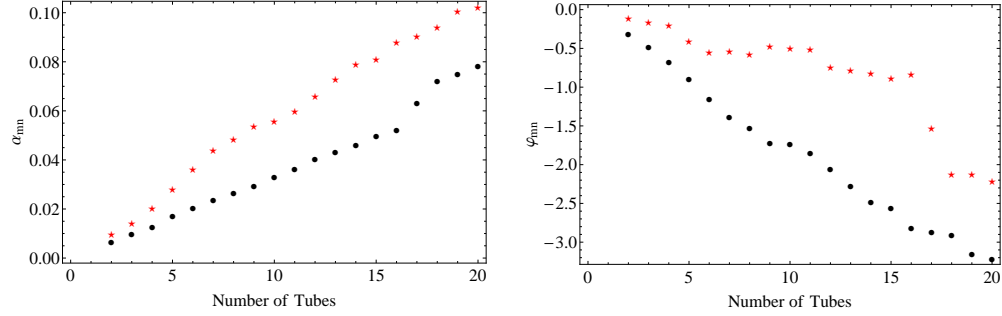


Figure 3.8: The absorption and phase of a 3 mHz f mode ($m = 0$: red star, $m = 1$ black dot), as the number of tubes that reside within a circle of radius 2.5 Mm increases. Each additional tube increases the absorption and negative phase shift. Generally following a linear relationship. We see in this distribution that absorption of the $m = 0$ is greater, while the $m = 1$ wave has a larger negative phase shift.

3.3.3 Case Study: Magnetic Flux

The results thus far have shown how the multiple scattering regime creates a collective behaviour of an entire flux tube bundle. This collective behaviour then raises the question, how do the scattering properties of an ensemble differ from a single tube that has the same magnetic flux as the entire ensemble? In order to remain consistent, we examine how a 3 mHz f -mode interacts with two different cases. The first is a trio of ensembles with three tubes within each (see Figure 3.9). The centres of these ensembles are separated by λ and are evenly spaced from the origin in an equilateral triangle distribution. Within each ensemble are three identical tubes (with $\beta = 1$ and flux $= \Phi_f$) which are separated by 0.2λ (0.49 Mm), in a similar equilateral triangle distribution to the larger structure. The second case replaces these bundles with three individual tubes with the same magnetic flux as each entire bundle ($3 \times \Phi_f$). A comparison of these two cases will show how the scattering affects of a bundle differ from that of a single tube.

Figure 3.10 shows the absorption and phase of both cases, as well as the change from their isolated (non-interacting) values. In both cases the absorption and phase (for interacting tubes) have a similar distribution across m . However, the peaks in the distribution appear at high m compared to the other study in this chapter. These different peaks are the result of the triangular positioning of the ensembles and the nature of the higher flux. The greatest differences in the absorption of the two cases occur in the $|m| \leq 3$ range, with higher m showing little difference between the two cases. How-

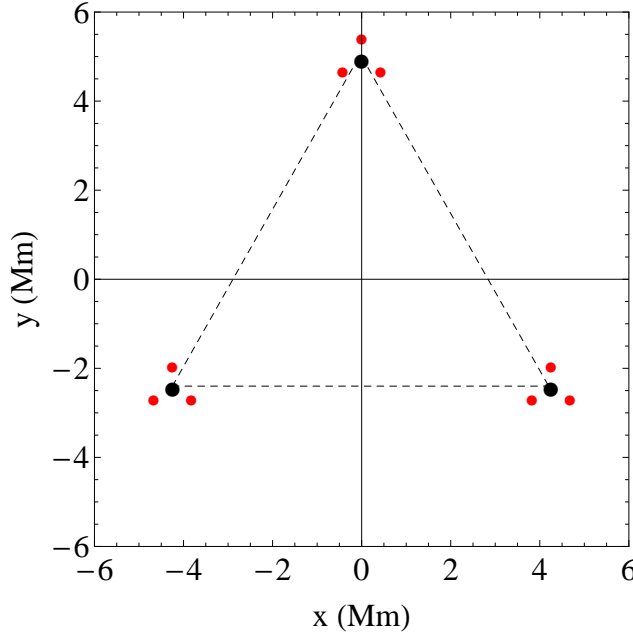


Figure 3.9: The positions of the tubes in the magnetic flux case study. The tubes within the small bundles (red points) are separated by ≈ 0.49 Mm with respect to the other tubes within their ensemble, and the centre of each bundle is located 4.9 Mm from the origin. The black dots show the comparative case with three tubes located at the origin of the previous ensembles, but with a flux equal to that of an entire bundle.

ever, the phase shows noticeable differences across all m . Close examination of how the absorption and phase changes from the isolated situation shows a very different distributions. In the three tubes case the absorption is decreased for $|m| = 0, 3, 6$, while the change in phase is small (of order 10^{-2}). However, the bundle case shows a decrease in absorption for $|m| = 1$ as well, while the change in phase is a magnitude larger than the three tubes case. Overall, the results of this study show how small bundles of flux tubes can imitate a single flux tube of greater magnetic flux, resulting in a similar distribution of the absorption and phase across m .

3.4 Discussion and conclusions

We have extended the work in Chapter 2 to ensembles of more than two tubes. This study represents a significant step in understanding the seismic behaviour of complex ensembles of small magnetic flux tubes threading the solar surface. We have examined cases of both regular symmetric and random

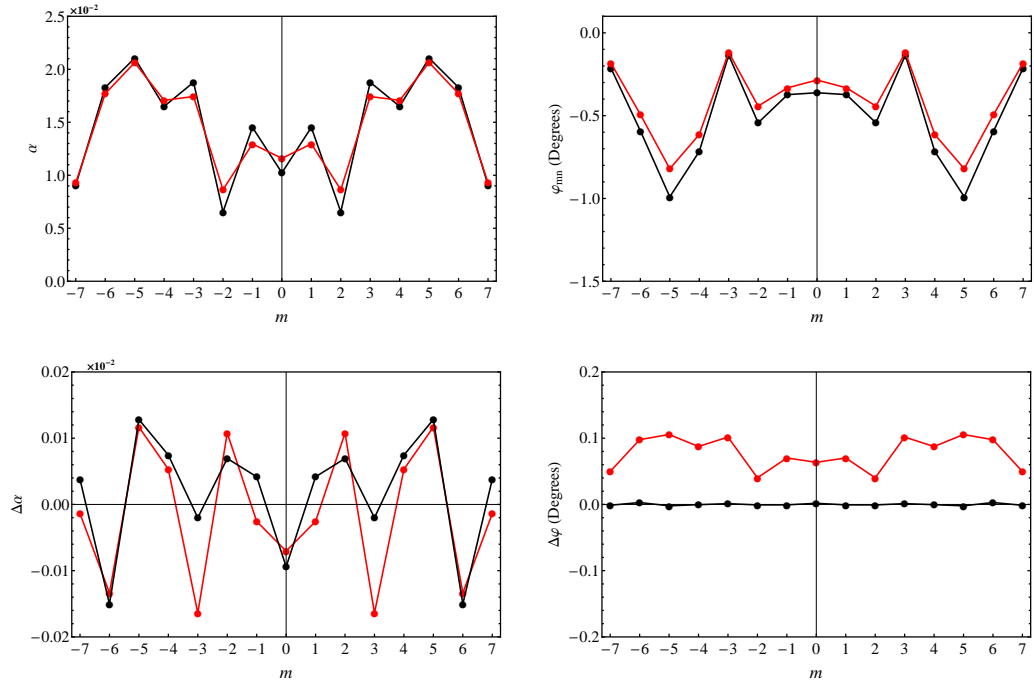


Figure 3.10: The absorption and phase (top) for the magnetic flux case study, with their respective change to their non-interacting situations (bottom). The line colours match that of Figure 3.9. As with the previous symmetric studies in this chapter, the absorption and phase shift are identical across $\pm m$. However, the configuration of this ensemble creates peaks in absorption and phase in the range of $3 \leq m \leq 6$ (instead of $|m| \leq 1$).

flux tube distributions within a stratified atmosphere, allowing scattering between both m and p_n modes. The incoming and outgoing waves are defined in terms of waves centred upon the origin, in a similar fashion to observational Hankel analysis. The caveats to our model are outlined in Hanson and Cally (2014) (Chapter 2), and while here we address the indirect scattering affects of incident $|m| > 1$ waves, the tubes are still assumed to be thin and unable to scatter pure fluting modes (as defined in their local coordinate system). As such, the direct absorption of fluting modes is still not addressed due to mathematical complexity. Studies of thicker tubes that can directly interact with these modes may require direct numerical simulation.

Clearly the thin tube approximation cannot be continued to arbitrary height, as the expansion of the flux tubes eventually sees them thicken to the stage where the assumption breaks down (Bogdan et al. 1996). Our stress-free top boundary condition is a simplistic attempt to avoid this inconvenience, and ignores potential upward losses, both in the flux tubes (though see Crouch and Cally 1999) and the field-free atmosphere. Upward losses in the field-free region may not be important for low frequencies where the p -modes reflect quite low, but above the acoustic cut-off they do in reality penetrate into the atmosphere.

In this study the definition of absorption is positive by its very nature, as there cannot be more energy emitted than was sent in. Felipe et al. (2013), as well as the observations of Braun (1995) calculated negative absorption coefficients (emission) in some cases, which was due to the coordinate definition, rather than real emission. We note that this study sends in a pure cylindrical wave, and hence will not produce negative absorption in m . In numerical studies (as well as observations), plane waves consist of all m modes and hence interactions between various m in the multiple scattering regime may lead to the perceived ‘negative’ absorption in Hankel analysis.

Having stated these clarifications, let us consider the implications of the symmetric ensemble studies. In these studies the tubes are identical, and positioned in a symmetrical nature around the origin. The three-tube cases are similar in fashion to the numerical studies of Felipe et al. (2013), while the seven-tube cases are similar to Daifallah (2014). The symmetry of the system maintains a mirror distribution of absorption and phase shift between $\pm m$. Complementary to Felipe et al. (2013), the absorption peaks for the $|m| \leq 1$ modes, with $|m| = 1$ showing the greatest absorption, but these coefficients diminish rapidly with increasing $|m|$ thereafter. The multiple scattering between the tubes alters the coefficients, primarily for $|m| \leq 1$ modes. In this model these results are reasonable, given that the only scat-

tering from a tube is in $|m| \leq 1$ and outgoing wave components of $|m| > 1$ is purely a fraction of the incoming $|m| \leq 1$ wave. As in the study of Hanson and Cally (2014), the near-field enhances the multiple scattering between tubes, leading to greater changes in absorption and phase when compared to the case of far-field interactions alone. Expanding to larger ensembles of six or seven tubes demonstrates similar behaviour, with the larger tube numbers altering the absorption and phase in significant ways. Firstly and most clearly, the scattering effects are generally increased as a result of the additional contribution from each tube to the scattered wave field. This is reasonable given the results shown in Figure 3.8. Secondly, the presence of additional tubes that are within the near-field of each other, creates a significant increase (an order of magnitude) in the change of absorption and phase when compared to the smaller three tube values. Lastly, the addition of the seventh tube reduces $\Delta\alpha$ for the kink modes, while enhancing the negative phase shift of the sausage mode. These three results demonstrate that the addition of more tubes, within close proximity, can change the observable distribution of absorption and phase across m .

Interestingly, in symmetric ensembles an incoming wave of even m is unable to generate an outgoing odd m wave, and vice versa. The odd m components scattered by each tube interferes at the origin with the same components generated by a tube located on the other side of the origin. The interference results in no outgoing wave of odd m from the origin, given an incident even m wave. Thus, similar to a single tube that can only scatter the incident m wave, a large symmetric ensemble is unable to scatter waves of odd (or even) m order given the incident wave of even (or odd) order. While truly symmetrical ensembles could not realistically exist, this is an interesting result in the case of near-symmetrical ensembles; we may expect diminished outgoing odd m components from an ingoing even m for roughly symmetric ensembles. With regards to p_n mode scattering, the results are consistent with the observations of Zhao and Chou (2013) that the outgoing energy of a $p_{n'}$ mode rapidly diminishes with increasing n . The strongest coupling is between the f -modes.

We have also investigated random ensembles of tubes. The random positioning of identical tubes breaks symmetry in m of the absorption. The resulting asymmetry is enhanced for higher frequency waves, so these ensembles may be more sensitive observational probes. However, phase shows an apparent mirror symmetry across m regardless of tube arrangement. We note that the ensembles show a difference in phase between $\pm m$, but these differences are small compared to the actual values. This apparent symmetry

could be attributed to the fact that as more thin tubes are placed randomly within close proximity, the system will approach a closely symmetrical system. In fact, when the system is of a small number of tubes (Hanson and Cally 2014), or contains thicker tubes (Felipe et al. 2013), the asymmetric nature is more apparent in the phase data.

Finally, we investigated the question of how the scattering effects induced by the multiple scattering regime in a bundle, differ from those of a single tube of magnetic flux equal to the entire bundle. The collective nature of ensembles has been apparent to this point, and the results of this study clearly point to the fact that the multiple scattering within a small ensemble will result in the constituent tubes behaving as a single tube. It was shown that the distribution across m were similar for both the absorption and phase with a small degree of difference, especially in the $|m| < 3$ range. However, the greatest difference in these two cases was apparent when investigating the difference from their respective isolated values. While a non-interacting ensemble is unphysical, these results demonstrated how powerful the near-field is in altering the scattering nature of the constituent tubes.

Given these results and taking into account the simplicity of the model, how can we use this model to interpret observable parameters? Braun (1995) was amongst the first to determine the absorption and phase of cylindrical waves within magnetic plage regions, finding significant measurable absorption, while Braun and Birch (2008) found that plage produces considerably less shift than penumbrae and umbrae. We have shown here that within closely packed ensembles the multiple scattering regime enhances both absorption and phase shift. In fact the larger the ensemble, or higher the frequency, the greater the absorption. This is a reasonable result, given that each additional tube will absorb more of the incident wave, and will have this absorption coefficient enhanced by the scattered wave field from nearby tubes. Within large enough ensembles the absorption coefficients should be measurable above any noise. The spatial distribution of tubes appears to have a greater effect on absorption at higher frequencies (5 mHz), which therefore may be more useful observational probes. Also the absorption profiles are heavily altered by the characteristics of the individual tubes (in this study β), and may be used to indicate the internal constitution. Our obtained phase shifts are small, possibly too small for measurable certainty (especially at 3 mHz), and thus are not in contradiction to observation. Given observations with an appropriate spatial/temporal resolution, the outgoing phase may be used for probing sub-surface structures, as we have shown that individual tube characteristics as well as the number of tubes will affect the

outgoing phase. This model is a significant step in an analytical approach to the multiple scattering regime. As the aim of scattering studies is to constrain sub-surface structures with scattered wave field data, both numerical and analytical models must continue to be improved to better interpret observational results.

Monash University

Declaration for Thesis Chapter 4: Using SDO Data to Examine the Seismic Emissions Surrounding Complex Active Regions

Declaration by candidate

In the case of Chapter 4, the nature and extent of my contribution to the work was the following:

Nature of contribution	Extent of contribution (%)
Key Ideas, data reduction, development of codes, results, writing of paper.	80

The following co-authors contributed to the work. If co-authors are students at Monash University, the extent of their contribution in percentage terms must be stated:

Name	Nature of contribution	Extent of contribution (%) for student co-authors only
Alina –C. Donea	Supervision and guidance, discussion and analysis	
K.D Leka		
Charles Lindsey		

The undersigned hereby certify that the above declaration correctly reflects the nature and extent of the candidate's and co-authors' contributions to this work*.

Candidate's Signature		Date 13/10/2014
--------------------------	--	--------------------

Main Supervisor's Signature		Date 13/10/2014
-----------------------------------	---	--------------------

*Note: Where the responsible author is not the candidate's main supervisor, the main supervisor should consult with the responsible author to agree on the respective contributions of the authors.

Chapter 4

Using SDO Data to Examine the Seismic Emissions Surrounding Complex Active Regions

The use of holography in the high-frequency p -mode spectrum can sufficiently resolve the distribution of enhanced seismic emissions within halo structures surrounding active regions. In doing so, the application of statistical methods can ascertain relationships with the magnetic field. This is the focus of our study.

The mechanism responsible for the detected enhanced seismic emissions around solar active regions has yet to be explained. Furthermore the relationship between the magnetic field and enhanced seismic emission has not yet been comprehensively examined. We have used vector-magnetograms from HMI/SDO to image the magnetic field properties in the halo. In doing so, the acoustic morphology of three active regions with complex halos and glories, has been explored and some of these acoustic properties have been linked to the magnetic field configuration. Additionally, we have compared the results of the seismic emission maps calculated from holography and the commonly used local acoustic oscillation map, finding that the two types of halos are very similar, although close scrutiny does show subtle differences.

4.1 Instrumentation: SDO

To study the mechanisms responsible for local helioseismic phenomena, high resolution observations of the Sun need to be analysed. In order to achieve this, the Solar Dynamics Observatory (SDO) was launched on the 11th of February 2010, to provide near-continuous imaging of the full solar disk. SDO's three instruments, the Helioseismic and Magnetic Imager (*HMI*, Schou et al. 2012b), EUV Variability Experiment (*EVE*, Woods et al. 2012) and the Atmospheric Imaging Array (*AIA*, Lemen et al. 2012), simultaneously capture full-disk images in numerous wavelengths to provide detailed information about the solar atmosphere. Improving on its predecessor, the Michelson-Doppler Imager (MDI) on board the Solar and Heliospheric Observatory (SOHO), SDO's HMI provides higher resolution images of the surface velocity, magnetic field and intensity continuum more frequently and at four times the resolution. Meanwhile, EVE measures the Sun's extreme ultraviolet output, which is responsible for heating the Earth's upper atmosphere. Finally, the AIA instrument provides detailed information of various regions ranging in height from the photosphere to the upper corona. In this study, the data products from the HMI and AIA instruments will be used to examine power halos.

Since the beginning of its mission, HMI has provided Doppler data (Dopplergrams) of high spatial resolution ($0.5''$) and temporal cadence (45 s). The Dopplergrams are calculated from observations of the $6173.3 \pm 0.1 \text{ \AA}$ Fe I line which has a formation height, once resolution limitations are accounted for, of 140-150 km (Fleck et al. 2011). With these observations taken every 45 s, spectral analysis performed on any surface oscillations will have a high-frequency limit at 11.1 mHz (an improvement on MDI: 8.3 mHz). This limit is known as the Nyquist Frequency. Thus far, most holography studies have used MDI data, but the higher resolutions of HMI make it ideal to examine the spatial distributions of enhanced seismic glories, as well high frequency seismic sources.

Another significant advantage of HMI data is its capability to detect magnetic field characteristics, such as orientation and magnitude. A brief overview of how magnetic field vectors are determined is given here, and for further information refer to Hoeksema et al. (2014). The magnetic field characteristics are determined from circular and linear polarized light, detected by HMI every 135 s (Schou et al. 2012a). Detections are measured in six wavelengths and averaged over 720 s to reduce noise, which reduces the cadence to 12 minutes. These polarimetric quantities are the Stokes parameters

(I, Q, U, V) and the final step in the pipeline is their inversion through the use a custom version of the Very Fast Inversion of the Stokes Vector (“VFISV”, Borrero et al. 2011; Centeno et al. 2014). The resultant maps (referred to as *vector-magnetograms*) specify the absolute magnetic field strength as well as the orientation (azimuth and inclination) in each pixel.

Prior to inversion of the Stokes parameters, the magnetic field orientation was extrapolated through various methods (e.g. potential, linear force-free and non-linear force-free fields), which is potentially problematic as it may lead to inaccurate representations of the magnetic field (e.g. Wiegmann et al. 2005). However, as Stokes parameters are determined directly from observation, confidence in the accuracy of magnetic field vectors is high. But, while the Stokes parameters can give insight into the magnetic fields, there is a major limitation that requires consideration. The determination of the transverse magnetic field requires inversion of Zeeman splitting, which results in an azimuthal ambiguity of 180° (Harvey 1969). This inherent ambiguity is resolved in the HMI pipeline using a minimum energy method (Metcalf 1994; Leka et al. 2009; Hoeksema et al. 2014).

We conclude this section by outlining the capabilities of the AIA instrument. Unlike HMI, AIA produces lower resolution images at $0.6''$, which results from the larger field of view required to observe the corona. However, due to the nature of the phenomenon it observes (e.g. flares) the cadence is significantly better ~ 12 s. AIA observes two ultra-violet (UV) and seven Extreme Ultra Violet (EUV) channels. The two UV channels, 1700\AA and 1600\AA , highlight the concentration of magnetic fields near the photosphere at heights 360 km and 430 km, respectively (Fossum and Carlsson 2005). The presence of strong magnetic fields appear as black pixels within the images, while weaker magnetic fields (but still concentrated) appear as bright pixels. These two channels show the nature of the magnetic field just above the observation heights of HMI. Meanwhile, the seven EUV channels show detailed information of upper chromosphere and corona. Together with HMI data, the information provided by AIA will shed some light on the nature of magnetic fields and seismic emission surrounding active regions. However, holography is restricted to calculating seismic emission at and below the photosphere, and thus we are restricted in our comparisons with AIA data to a qualitative nature.

4.2 Data Processing

4.2.1 Data Selection

This study has focussed on large multi-polar active regions that have emerged since the launch of SDO. Twenty-four hours of near-continuous observations were sought for each active region, in order to obtain clear integrated power maps that show the enhanced acoustic power halos at high frequencies. Each chosen region is missing only a few frames (< 20) within their respective 24 hour period of observation. These missing frames were absent from the HMI pipeline, presumably due to observational errors. In order to reduce any line of sight errors, the observation time for each region was chosen so that it passed through the central meridian half-way through its respective time frame. The asymmetry of large active regions makes it difficult to determine when the centre of a region passes through the meridian. However, the Carrington latitudes and longitudes specified herein (see Table 4.1) are to be considered the approximate centre of the associated active regions. Table 4.1 outlines the chosen active regions and corresponding observation dates, tracked Carrington latitude (L) and longitude (B), National Oceanic and Atmospheric Administration's (NOAA) Active Region (AR) designation and the vector-magnetogram data sets used.

We note that in the quiet sun, spatial fluctuations caused by interference among modes with the same frequency, can appear in local acoustic power maps. Chou et al. (2009) stated the only way to reduce errors that arise from these fluctuations is to increase the number of observed frames. Therefore, twenty-four hours of observations ensures that a significant number of frames are taken into account.

All data examined here comprises full-disk Dopplergrams, intensity continuum, SHARPs vector-magnetograms (see section 4.2.3 for further details) and the AIA channels (1700Å, 1600Å). The frame size of the full-disk images is 4096×4096 pixels, where each pixel size is approximately $0.5''/362.5$ km (with AIA: $0.6''/435$ km). The temporal resolution of the Dopplergrams and Intensity cubes are 45 s, while the SHARPs products are 720 s. This results in 16 Doppler images for every SHARP image.

The following sections outline the procedure for data reduction (§ 4.2.2), an overview of the SHARPs data (§ 4.2.3), the process required for using the SHARPs products (§ 4.2.4) and the precautions taken with all data (§ 4.2.5).

Table 4.1. Information of Observed Active Regions

Date and Time of Initial Observation	Carrington L and B	NOAA AR designation	Vector Magnetogram data set
2011/02/13 1200 UT	35.9 -19.4	11158	SHARPs
2012/03/08 1000 UT	303.9 17.2	11429	SHARPs
2014/01/07 0800 UT	96.7 -9.8	11944	Full Disk

4.2.2 Data Reduction

Due to the varying sizes of the active regions and extent of the surrounding plage, all three Doppler cubes have differing sizes on which holography computations are performed. The Doppler data was Postel projected and tracked at the specified Carrington coordinates (Table 4.1) throughout the twenty-four hour period. Any missing or defective images were replaced with blank frames. At each time step, the rotation effects of the sun were removed and the resultant image was projected onto an appropriately sized blank frame with a frame height and width of pixel count 2^n (which assists in the Fourier Transform). The data cube (of size $2^n \times 2^n \times 1920$) was then transformed using the Very Fast Fourier Transform algorithm, whereby each cube was filtered into frequency bands of 1 mHz bandwidth. Having split the data cube into bandwidths of 1 mHz, the temporal resolution of any computed egression cube will be reduced to 1000 s ($\Delta t = 1/\Delta\nu$). Since we will be examining integrated power maps this reduction will not affect the results.

At this stage, two separate computations (mutually exclusive) are performed. One transforms the maps back to the time domain and calculates the associated oscillation power in each bandwidth, thereby determining the local acoustic power. The other is the seismic holography computation in the frequency domain, which is transformed back to the temporal domain and the associated power of seismic sources is calculated.

Regarding the seismic holography computation, an egression (Equation 1.13) was calculated at the surface ($z = 0$)¹, waves that only travel only one skip were included, with all further skips ignored. The pupil size used

¹I point out to the reader that as per the discussion in the introductory chapter, the presence of strong seismic emitters in the halo will cause the appearance of artificial seismic stalactites to appear at various depths. Hence, all holography computations will be restricted to the surface.

in these calculations has an inner radius of 7 Mm and an outer radius of 44 Mm, which results in a diffraction limit of 2.5 Mm. With the chosen focal depth and pupil size, the egression integral (Equation 1.13) was calculated using a plane-parallel assumption, where the curvature of the solar surface is assumed to have negligible affects on the holography computation. This assumption is valid, considering that the pupil size is significantly smaller than the solar disk.

4.2.3 The Use of SHARPs and Full-disk Vector Magnetograms

At the time of this research, the SDO pipeline had full-disk images of all observable parameters, with the exception of computed full-disk disambiguated azimuth maps (before January 2014). As such, the Space-weather HMI Active Region Patches (SHARPs) were made available, in which the disambiguated azimuth is computed (Bobra et al. 2014). As a result of using these SHARPs products, the following pipeline procedures need to be taken into account. Once the full-disk Stokes parameters are computed, the data is then reduced to rectangular patches (called HMI Active Region Patches; HARPS) which typically contain regions of strong magnetic fields that may not coincide with NOAA designations. Then, these patches are traced throughout their transit across the solar disk (Turmon et al. 2014). The inversion of the Stokes parameters within these patches then follow the previously discussed process (§4.1). The limitation in comparing SHARPs products with full-disk Doppler images is that the calculated patch is not large enough to cover all of the quiet sun in which halos occur. As such this, study is forced to omit data computed in the power maps that do not have corresponding SHARPs data. However, the SHARPs products are generally large enough to examine a majority of the halos.

For the active regions 11158 and 11429, the SHARPs data was used. However, in the case of AR 11944 (which occurred after Jan 2014), full-disk disambiguated vector-magnetograms were available. Three disambiguation processes can be applied to this data which include ‘randomly assigned’, ‘radial-acute’ and ‘potential-acute’ methods. The SDO JSOC team advises that the randomly assigned method is the safest for use in the quiet sun, due to the other method’s tendency to show large-scale patterns in weak regions. Therefore, we have used this method for resolving the ambiguity in the halo.

Having collected the vector-magnetograms of all three regions, the data was then projected and aligned to the full-disk Dopplergrams. The alignment

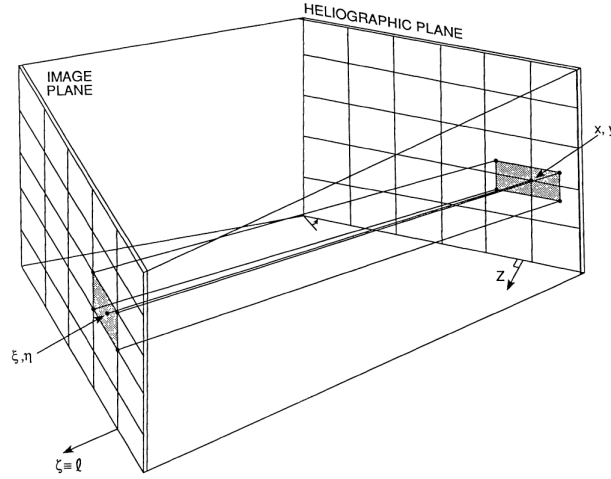


Figure 4.1: An illustration of how the heliographic plane differs from the image plane. This difference requires the appropriate transforms of Equation 4.1 to be applied, in order to obtain magnetic field vector relative to the solar surface. Image from Gary and Hagyard (1990).

was achieved through the matching of the reference latitude and longitude of each region. Close scrutiny of SHARPs data reveals a 1 pixel misalignment with the Dopplergrams, and this was taken into account in projections.

4.2.4 Mapping of the Magnetic Field Vectors

An inherent complication of observing the Sun is that measurements of observables such as Dopplergrams and magnetic fields are subject to the line-of-sight. Specifically, the angle that subtends the normal of an observed point on the solar surface will affect the measured parameter. Consequently, appropriate transforms need to be made in order to draw conclusions on the relationships between observables. To accurately examine the relationship between the magnetic field and seismic emission, the magnetic field relative to surface normal must be determined. Specifically, a transform needs to be applied to the vector-magnetograms to convert the pixel values, which are measured by the CCD (referred herein as the image plane), to values that are relative to the solar surface (the heliographic plane). Figure 4.1 shows how the image and heliographic plane differ due to the line of sight between the observed solar surface and the detector. Gary and Hagyard (1990) specifies this transformation of magnetic field image plane components ($B_{\mathbf{r}}^i$, where

$\mathbf{r} = (x, y, z)$, to the heliographic plane ($B_{\mathbf{r}}^h$) as:

$$\begin{pmatrix} B_x^h \\ B_y^h \\ B_z^h \end{pmatrix} = \begin{pmatrix} a_{11} & a_{12} & a_{13} \\ a_{21} & a_{22} & a_{23} \\ a_{31} & a_{32} & a_{33} \end{pmatrix} \begin{pmatrix} B_x^i \\ B_y^i \\ B_z^i \end{pmatrix} \quad (4.1)$$

where the matrix terms are given by

$$\begin{aligned} a_{11} &= -\sin(B_o)\sin(P)\sin(L - L_0) + \cos(P)\cos(L - L_0), \\ a_{12} &= +\sin(B_o)\cos(P)\sin(L - L_0) + \sin(P)\cos(L - L_0), \\ a_{13} &= -\cos(B_o)\sin(L - L_0), \\ a_{21} &= -\sin(B) [\sin(B_o)\sin(P)\cos(L - L_0) + \cos(P)\sin(L - L_0)] \\ &\quad -\cos(B)[\cos(B_o)\sin(P)], \\ a_{22} &= -\sin(B) [\sin(B_o)\cos(P)\cos(L - L_0) + \sin(P)\sin(L - L_0)] \\ &\quad -\cos(B)[\cos(B_o)\cos(P)], \\ a_{23} &= -\cos(B_o)\sin(B)\cos(L - L_0) + \sin(B_o)\cos(B), \\ a_{31} &= +\cos(B) [\sin(B_o)\sin(P)\cos(L - L_0) + \cos(P)\sin(L - L_0)] \\ &\quad -\sin(B)[\cos(B_o)\sin(P)], \\ a_{32} &= -\cos(B) [\sin(B_o)\cos(P)\cos(L - L_0) + \sin(P)\sin(L - L_0)] \\ &\quad -\sin(B)[\cos(B_o)\cos(P)], \\ a_{33} &= +\cos(B)\cos(B_o)\cos(L - L_0) + \sin(B_o)\sin(B). \end{aligned} \quad (4.2)$$

Here B and L are the heliographic Carrington latitude and longitude of the observed point on the solar surface, and B_o and L_o are the latitude and longitude of disk centre. Additionally, the variable P is the solar P -angle that subtends the rotation axis and the north-south axis of the solar disk image.

We note that though the active region passes through the meridian (hence B_x requires no transform at that time), the active region is still above disk centre and thus requires the appropriate transforms to B_y and B_z .

Having calculated the heliographic field components, we redefine the inclination (γ) in a similar fashion to Schunker and Braun (2011),

$$\tan(\gamma) = \frac{B_z}{B_h}, \quad (4.3)$$

where $B_h = \sqrt{B_x^2 + B_y^2}$. Here γ ranges from -90° to $+90^\circ$, with the horizontal field being 0° and $+\gamma$ outward facing from the surface.

4.2.5 Statistical Precautions

The accuracy of the inferred field vector depends upon the strength of the I, Q, U, V polarization signals. In the quiet sun, where the acoustic halo is present, the signal strength of the Stokes parameters is generally weak, which results in a higher noise level. Since we are primarily concerned with the surrounding quiet sun in which the halos manifest, we have taken precautions when interpreting the associated field information.

We first reduced the noise in the azimuthal data by taking an average of the field vectors over a period of 36 minutes. Longer averaging results in additional uncertainty due to solar evolution. In the results of this study, we used the magnetic field data at the time the active region is situated on the central meridian. For consistency, we examined the magnetic field at different times and found the results to be in a general agreement (Appendix A). The second precaution was to only consider pixels that have a good signal to noise ratio ($|B|^2/|B_{error}|^2 > 1$; K.D Leka, Private Conversation). As a final precaution, we analysed a quiet sun patch void of any apparent magnetic structure, and found a minimum field strength of 60 G remains. As such, we omit pixels with field strengths below 60 G, attributing these values to noise. Upon performing these precautions, the remaining pixels number approximately 50% (see Figure 4.2) of those originally within the halo. As a result, the confidence in interpreting these pixel values becomes high and is a major improvement with respect to the work of Rajaguru et al. (2013), which used all pixels and imposed a lower field strength threshold of 40 G. Although a few studies have applied (in part) some of these precautions, we are unaware of any that have been as strict when examining the halos.

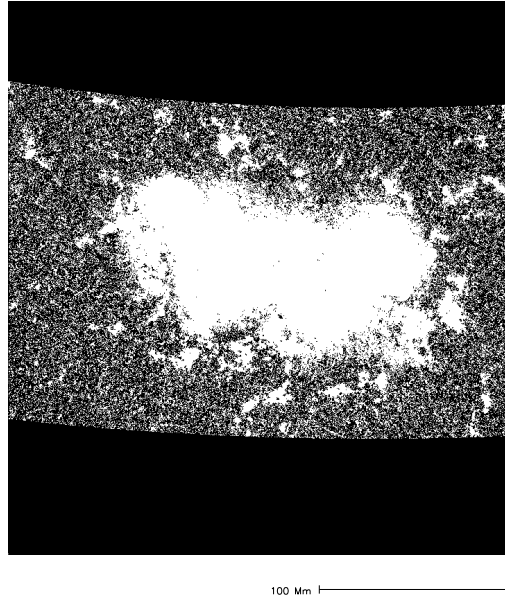


Figure 4.2: A mask applied to the active regions (in this case AR11429) to remove all pixels that have a signal to noise ratio less than 1, are below 60 G and that are situated outside of the SHARPs image area. White pixels remain in our analysis, while black pixels are removed. Pixels with stronger magnetic field strengths (within the active region) have a larger S/N ratio, therefore provide accurate field readings in the map, although they are not important for halo analysis.

4.3 Results

Figures 4.3 - 4.11 show the magnetic field maps, computed power maps (local acoustic and seismic emission) and the halo and glory locations of the three active regions examined. Power maps are displayed for the 1 mHz bandwidths centred on 3, 6 and 9 mHz. Appendix C shows the power maps for more frequency bands, but for the purpose of this chapter, these three bandwidths will suffice in examining halo morphology at low (3 mHz), high (6 mHz) and very high frequency (9 mHz) ranges. The morphological features of the magnetic and power maps will be discussed in the following sections. Particular attention will be given to the relationship between the magnetic field and the power halos. The width of the halos specified herein will be the smallest and largest widths from the penumbra boundary to the outer extent of the $\mathcal{C}_{1.4}$ contour (see below for definition).

For statistical purposes, we define the seismic emission halo as the region of enhanced power surrounding the active region at 6 mHz, with power exceeding 140% of the seismic power in the quiet sun ($|H_+|^2/|H_{+0}|^2 > 1.4$, see Figures 4.5, 4.8, 4.11). Herein, we refer to the outer bounds of this region as the $\mathcal{C}_{1.4}$ contour. Our choice in this power minimum provides a definable boundary for computing masks within which the pixels can be examined. If a lower limit is chosen, the halo becomes more diffuse with the quiet sun and becomes hard to define a boundary with which to draw any statistical conclusions. Interestingly, the boundary of $\mathcal{C}_{1.4}$ subtends an area of quiet emission in the 1700Å channel (bottom panel, Figures 4.5, 4.8, 4.11), suggesting that the physical conditions at 360 km, such as field line concentration, dictates the morphology of the seismic halo at the lower height of 150 km. Additionally, the area having intermediate seismic power ($1 \leq |H_+|^2/|H_{+0}|^2 < 1.4$) seems to be more of a transitory area, in which the magnetic field (near the active region) is strong. The 1700Å maps shows the intermediate power region coincides with high intensity pixels. We name this area the *seismic plateau* and we discuss its properties later.

Small regions within the halos, where the excess in seismic power is more than $1.8 \times |H_{+0}|^2$, have been identified as *acoustic glories*. The choice in this lower limit is based on a visual inspection of the seismic maps, with the identification of the most noticeable areas. A higher value of the threshold in seismic power means that fewer glories will be recorded for our statistical purposes. We aim at keeping a significant number of pixels that show significant enhancement in the seismic power. Therefore an optimal threshold value of 1.8 seems to suffice for all active regions analysed in this chapter.

These regions are located in the halo and are delimited by the green contours in Figures 4.5, 4.8 and 4.11.

4.3.1 Active Region Enhanced Power Morphology

10 February 2011: AR11158

The magnetograms and intensity continuum maps for AR11158 are shown in Figure 4.3, with calculated power maps shown in Figure 4.4 and the identified halo and glories in Figure 4.5. This complex active region has been the focus of many studies, with particular interest in the X2.2 flare that generated a sun quake on the 15th of February 2011 (Kosovichev 2011; Zharkov et al. 2011, etc.).

AR11158 is an isolated multi-polar region (Hale Class $\beta\gamma$) with an approximate area of $81 \times 127 \text{ Mm}^2$. The continuum maps (Figure 4.3 panel *a*) show three distinct regions. The east and west (relative to image) regions contain single, large asymmetric sunspots with pore structures nearby. The central region contains three large umbra regions separated by the surrounding and connecting penumbra. The magnetograms (panels *b* - *d*) show strong magnetic fields (peak 2700 G) that are highly inclined (see panel *d*) within the umbra of these three regions. These magnetic maps also show that the western region is of negative polarity, the east is positive and the central region is bipolar. Surrounding the three main structures with strong magnetic fields is a plage with weaker field strengths (300-1000 G).

The power maps in Figure 4.4 show a strong power deficit in both seismic emission and local acoustic power, which corresponds to the strong magnetic fields of the active region including plage. The low frequency maps (panels *a* and *b*) show an acoustic moat (~ 0.6 quiet sun units) surrounding the active region of a varying width of 17-37 Mm. At high frequencies (panels *c* and *d*), this moat is replaced with an enhanced power halo of similar width, in both the seismic emission (~ 1.54 quiet sun units) and local acoustic power (~ 1.45 quiet sun units). However at very high frequencies (9 mHz, panels *e* and *f*), the seismic emission halo becomes diffuse within the surrounding medium and the local acoustic halo is compact (with width $\approx 15 \text{ Mm}$), tracing around the strong power deficit of the active region. Additionally, in the local acoustic oscillation power, the formation of a secondary weaker halo has appeared, surrounding the halo at a distance of 25 Mm.

Figure 4.5 shows $\mathcal{C}_{1.4}$ and $\mathcal{C}_{1.8}$ contours, which will be examined in this study. These regions predominantly occur in the southern areas of the active region, with a small halo component in the north. In this active region,

strong seismic emitters are located within a glory to the south, occupying approximately 4% of the total halo region. The size of the individual, high powered emitters within the glory varies between 5-7 Mm in diameter.

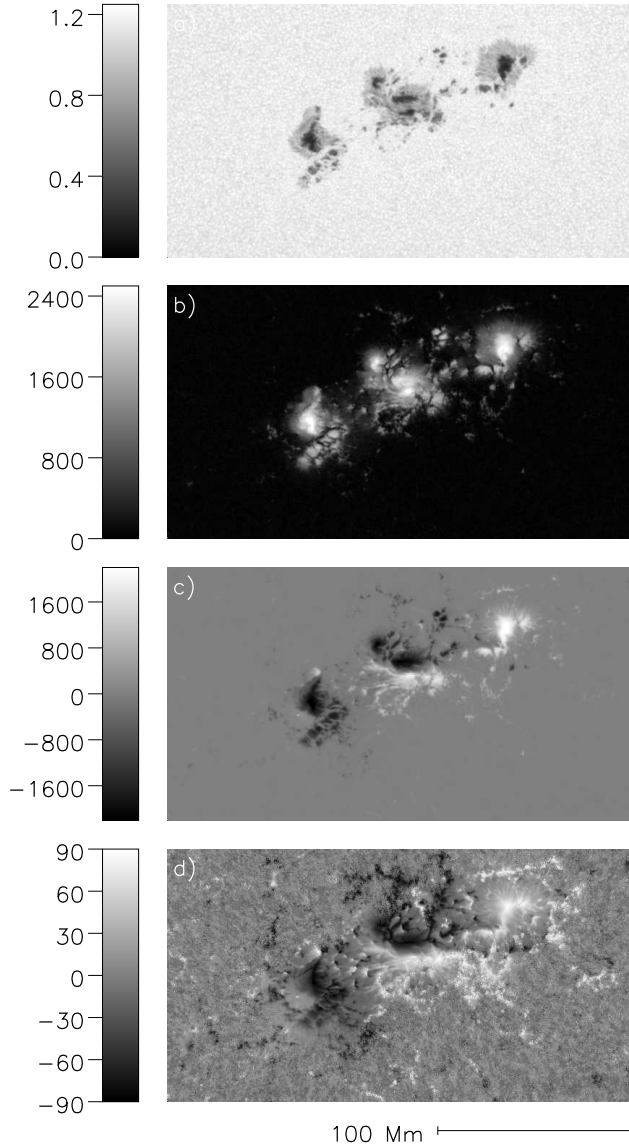


Figure 4.3: Snapshots of intensity continuum (panel *a*), $|\mathbf{B}|$ (*b*), B_z (*c*), and γ (*d*) for the active region AR11158 at the central meridian. AR11158 consists of three distinct regions of strong magnetic fields separated by magnetic plage.

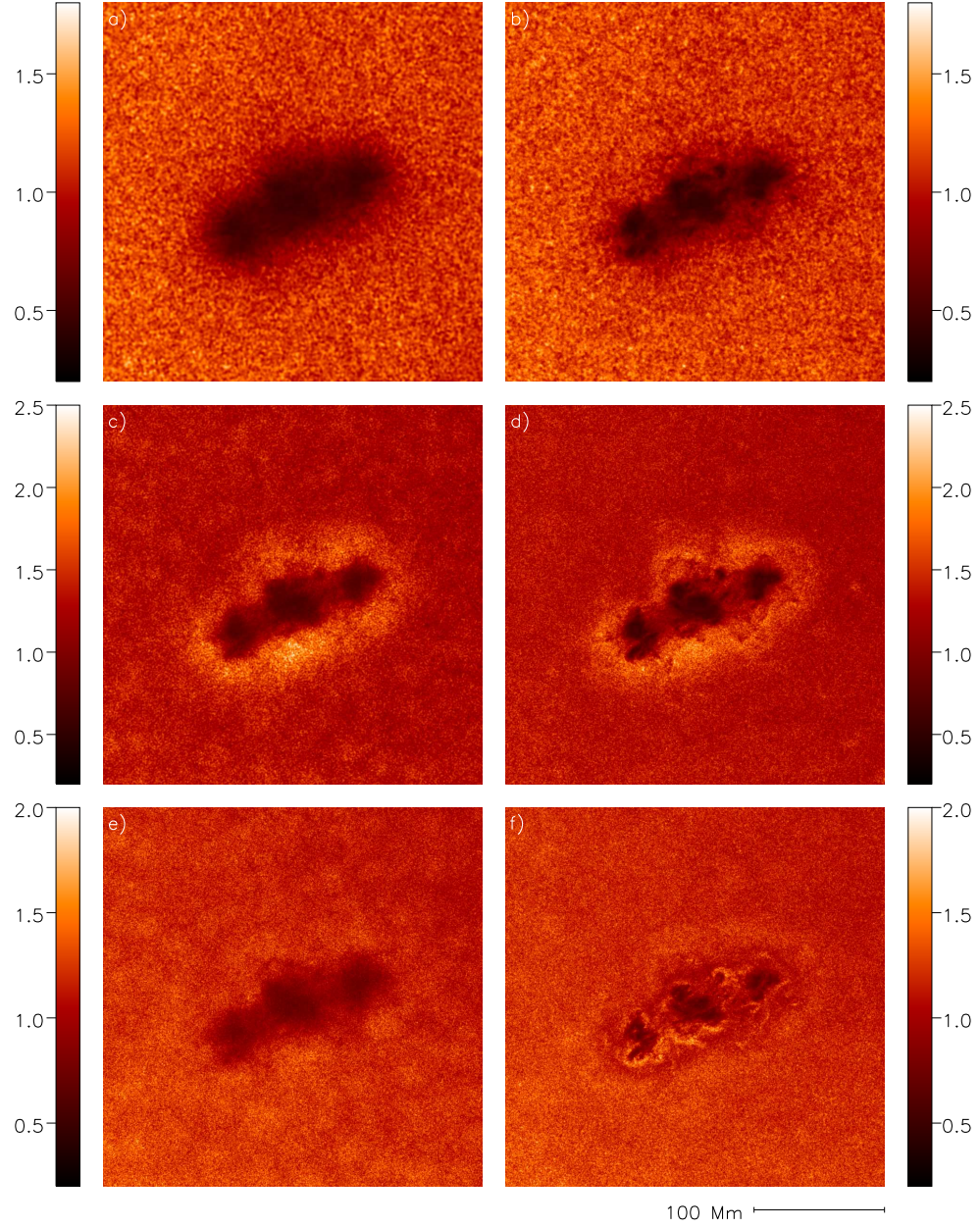


Figure 4.4: The seismic emission (left) and local acoustic (right) power maps at 3, 6 and 9 mHz (top to bottom) of the active region AR11158, normalized to the quiet sun. Comparison with Figure 4.3 shows that the seismic emission and local acoustic power are in deficit in the presence of magnetic fields, whether it be plage or stronger fields. Acoustic and seismic halos are visible at 6 mHz.

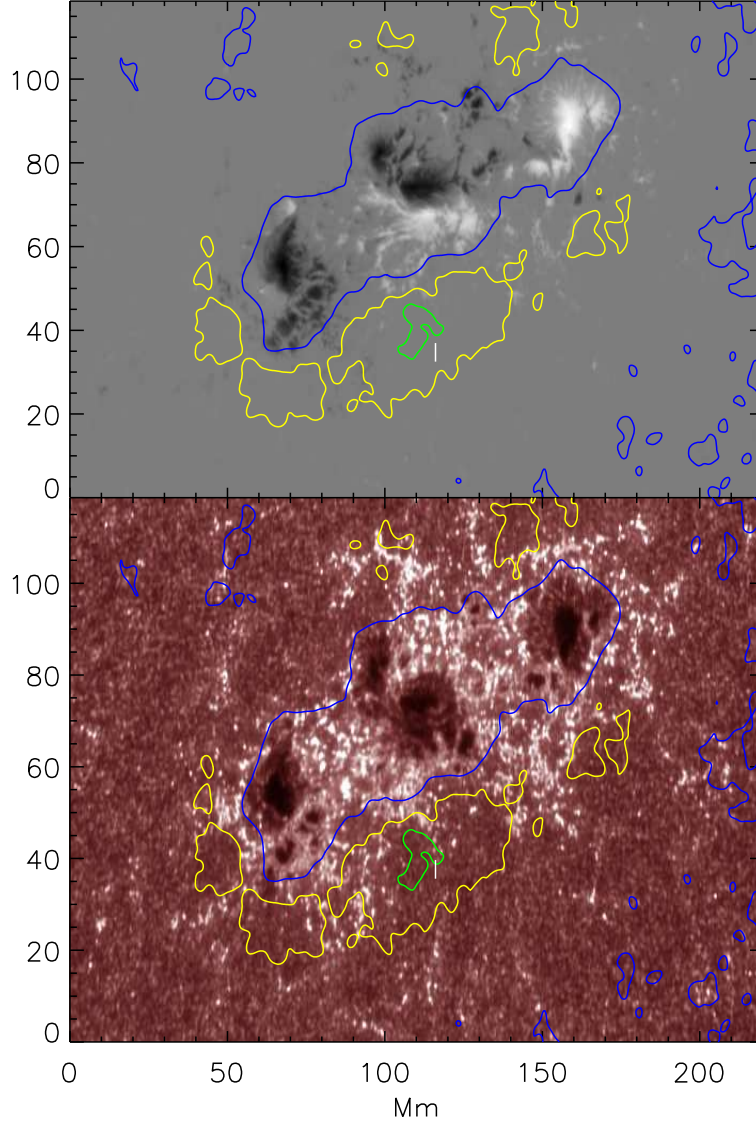


Figure 4.5: The contours of the halo (yellow, $|H_+|^2/|H_{+0}|^2 > 1.4$), glory (green, $|H_+|^2/|H_{+0}|^2 > 1.8$) and inner plateau boundary (blue, $1 < |H_+|^2/|H_{+0}|^2 < 1.4$) superimposed onto maps of B_z (top) and 1700\AA intensity (bottom) for the active region AR11158.

08 March 2012: AR11429

Figure 4.6 shows the intensity and magnetogram maps of AR11429, with the computed power maps shown in Figure 4.7. The halo, glories and plateau are shown in Figure 4.8. This active region is of similar size to AR11158 covering an area approximately $77 \times 133 \text{ Mm}^2$ in size. However, the entire active region has one encompassing penumbra. Interestingly, AR11429 is known as a rare ‘delta island’ active region (Elmhamdi et al. 2013), where the polarity is reversed compared to other active regions in the northern hemisphere. While most active regions in the solar northern hemisphere lead with negative polarity (for cycle 24), AR11429 leads with a positive polarity.

The intensity continuum maps show two predominant umbral regions to the east and west, with surrounding penumbra. These umbra have a radius of 11.5 Mm and 7 Mm, respectively, with a penumbra radius of 17 Mm and 9.5 Mm, respectively. Between these two regions are numerous magnetic pores with various umbra radii between 1-2.3 Mm. The magnetograms show a complex multi-polar active region (Hale Class $\beta\gamma\delta$) with associated plage located to the east and in a band (3-12 Mm wide) surrounding the region. The peak magnetic field strength of the active region is 2700 G and occurs in the two large umbra regions. Unlike the previous active region, the polarity here is contained at the north-east (positive) and south-west (negative), with a magnetic neutral line separating the two.

At all frequencies, the seismic and acoustic power maps (Figure 4.7) show a central region of greatly suppressed power (≈ 0.1 quiet sun values), which coincides with the strong magnetic fields of the active region. Again, at 3 mHz, the acoustic moat is present and ranges in thickness between 27-61 Mm. At 6 mHz, the area occupied by the 3 mHz acoustic moat is now a region of enhanced seismic emission (~ 1.6 quiet sun units), which is detected in the helioseismic holography maps. This enhancement is also seen in the local acoustic power maps (~ 1.5 quiet sun units). The halo surrounds the active region with a width of 25-60 Mm, and in some regions extends slightly beyond the region suppressed at 3 mHz. The seismic glories are mainly located at the north and south of the active region covering an area approximately $40 \times 76 \text{ Mm}^2$ and $20 \times 39 \text{ Mm}^2$, respectively. Additionally, there is a band of seismic glories located to the west occupying an area of approximately $17 \times 74 \text{ Mm}^2$. The bottom two panels of Figure 4.7 show that at higher frequencies (9 mHz), the seismic emission halo has become diffuse with the surrounding quiet sun and the region of power deficit corresponding with the strong magnetic fields, remains. However, the local acoustic power

halo is now compact (10 Mm wide), with a hint of diffuse enhancement beyond (30 Mm). Bright compact acoustic power areas can be seen within the central parts of the active region. These large power spikes (and their cause) have often been ignored in studies, and have only recently begun to be addressed (Zharkov et al. 2013, Donea et al. 2014, in preparation). As the power halos within the surrounding quiet sun are the focus of this study, we too will not address this phenomenon in detail.

There is a neighbouring active region located to the solar west (approximately 190 Mm) with the NOAA designation of AR 11430. The region between the two active regions is occupied by magnetic plage, which generates a small power deficit between the two. However, the two active regions are far enough apart that seismic (and local acoustic) power halos are restricted to their respective active regions, and as such the relatively small halo of AR 11430 will be omitted.

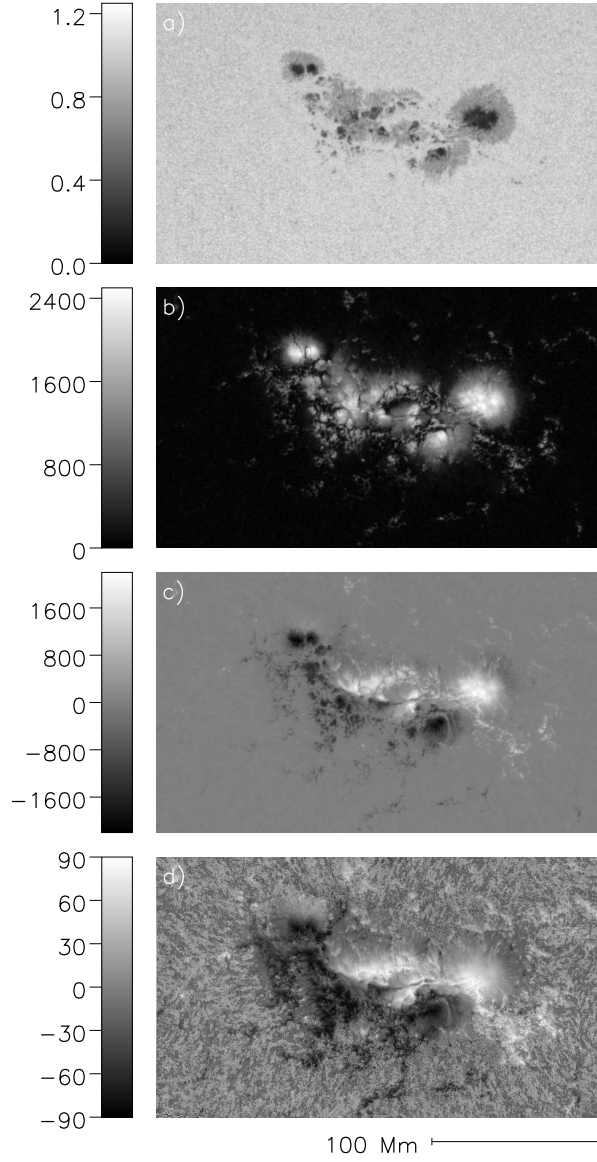


Figure 4.6: A snapshot of intensity continuum (*a*) and averaged maps (over 36 minutes) of $|\mathbf{B}|$ (*b*), B_z (*c*) and γ (*d*) for the active region AR11429 at the meridian. While this active region is multi-polar, the fields of identical polarity are confined into two separate regions, with positive polarity located in the north east and the negative polarity located in the south west region. Surrounding the entire active region is magnetic plage.

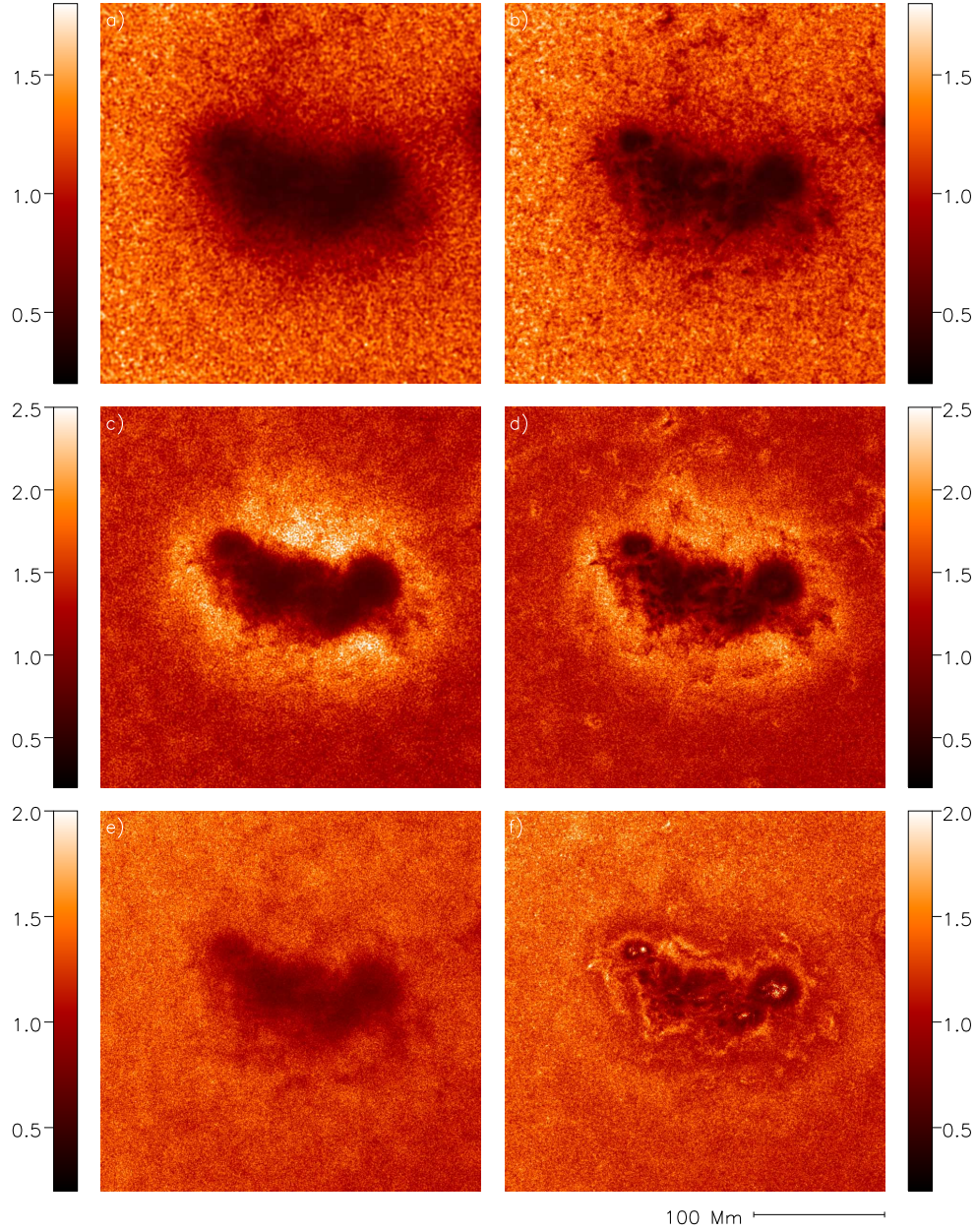


Figure 4.7: The seismic emission (left) and local acoustic (right) power maps at 3, 6 and 9 mHz (top to bottom) of the active region AR11429, normalized to the quiet sun. The magnetic plage that surrounds the active region shows a small deficit compared to the halo, but is close to quiet sun values.

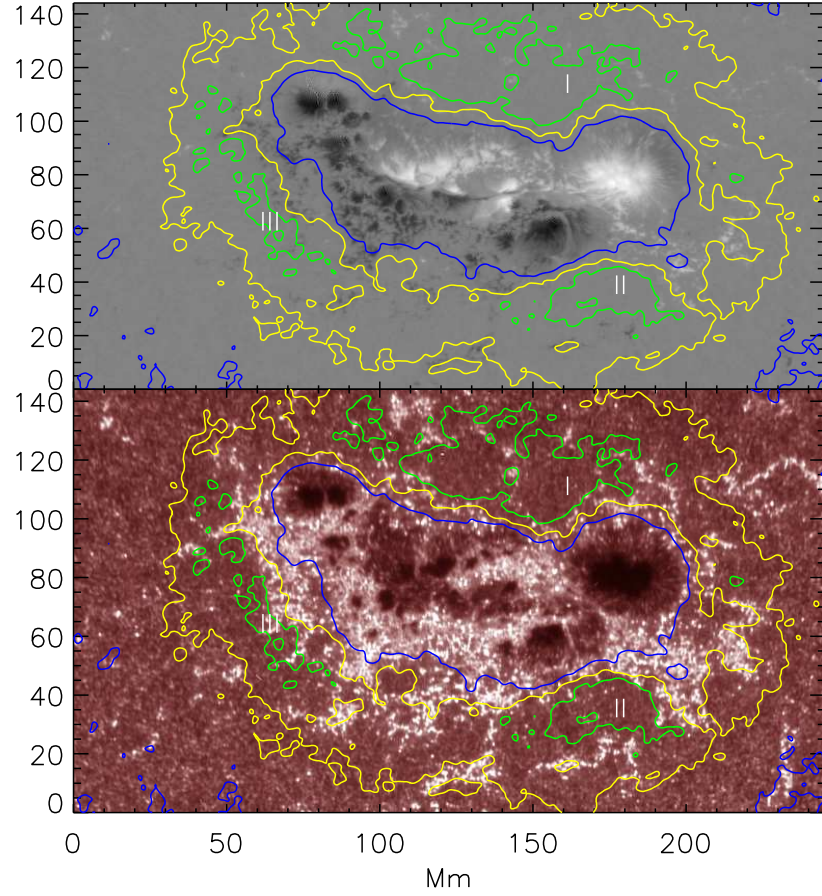


Figure 4.8: The contours of the halo (yellow), glories (green) and inner plateau boundary (blue) superimposed onto maps of B_z (top) and 1700\AA intensity (bottom) for the active region AR11429.

Table 4.2. Areas of the Seismic Halo and Glories

AR	$\mathcal{C}_{1.4}$ Area (Mm ²)	$\mathcal{C}_{1.8}$ Area (Mm ²)
11158	6.0×10^3	2.6×10^2
11429	4.6×10^4	1.0×10^4
11944	7.5×10^4	1.4×10^4

07 January 2014: AR11944

This active region is the largest examined in this study, covering an area of 125×228 Mm² and a maximum field strength of 4300 G. This active region has a Hale classification of $\beta\gamma\delta$, with a predominant sunspot (to the image east) of radius 15 Mm for the umbra and 28 Mm for the penumbra. A secondary smaller sunspot is located near the centre of the region, with an umbral radius of 8 Mm and penumbra of 16 Mm. Trailing these sunspots are small compact magnetic pores (1-3 Mm) of opposite polarity (negative) to the spots. The magnetograms also shows extensive plage interwoven between these pores. Figure 4.9 shows the continuum and magnetic maps for the active region AR 11944.

The power maps (Figure 4.10) again reveal the three main morphological features seen in the previous active regions: 1) The acoustic moat (~ 0.4 quiet sun values) occurs again at 3 mHz with a width of 16-32 Mm wide, 2) An enhanced halo (~ 1.64 quiet sun values) surrounding the active region at 6 mHz (16-45 Mm wide), 3) The diffusive behaviour of the seismic halo, and the change to the compact acoustic halo (≈ 10 Mm) at 9 mHz. However, what is noticeably different in this active region, is the extent and intensity of the seismic halo, as well as the presence of many seismic glories. The most intense emitters (see Figure 4.11) are situated in the south-east and northern sections of the halo, bordering the magnetic plage. The remainder of the halo is still intense when compared to the other active regions.

Pixels within the centre of the large sunspot appear to be defective in the Doppler images. Therefore, we have masked this region in order to remove any artificial sources occurring within the computed holography maps.

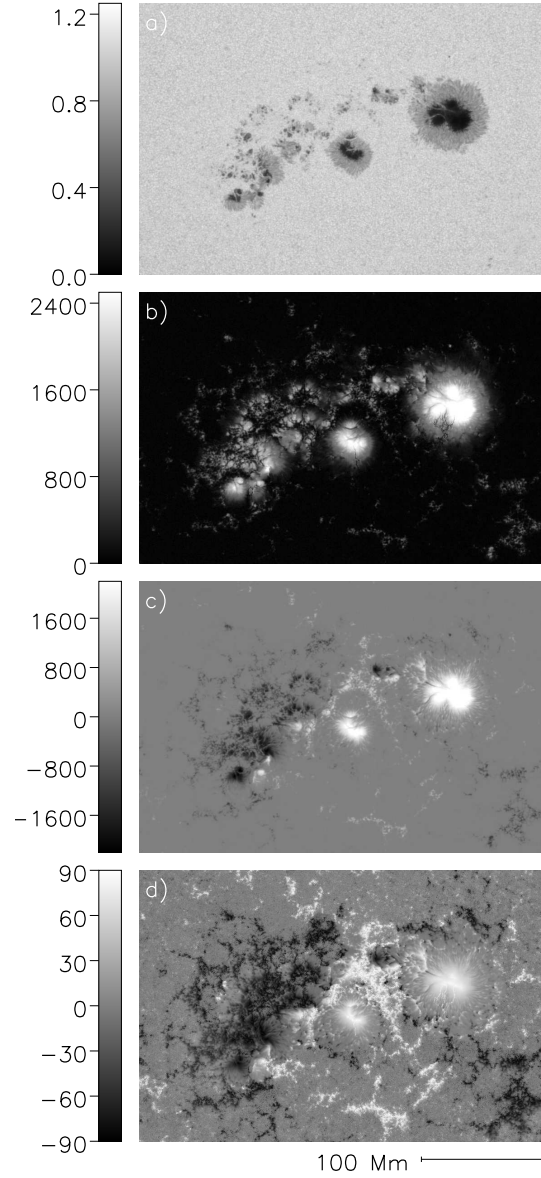


Figure 4.9: Snapshot of intensity continuum (panel *a*) and averaged $|\mathbf{B}|$ (*b*), B_z (*c*) and γ (*d*) for the active region AR11944 at the meridian. This large multi-polar active region consists of two sunspots of positive polarity, the largest of which (located in the east) has a radius of 28 Mm. Trailing these spots are small pores of negative polarity interwoven with dense magnetic plage.

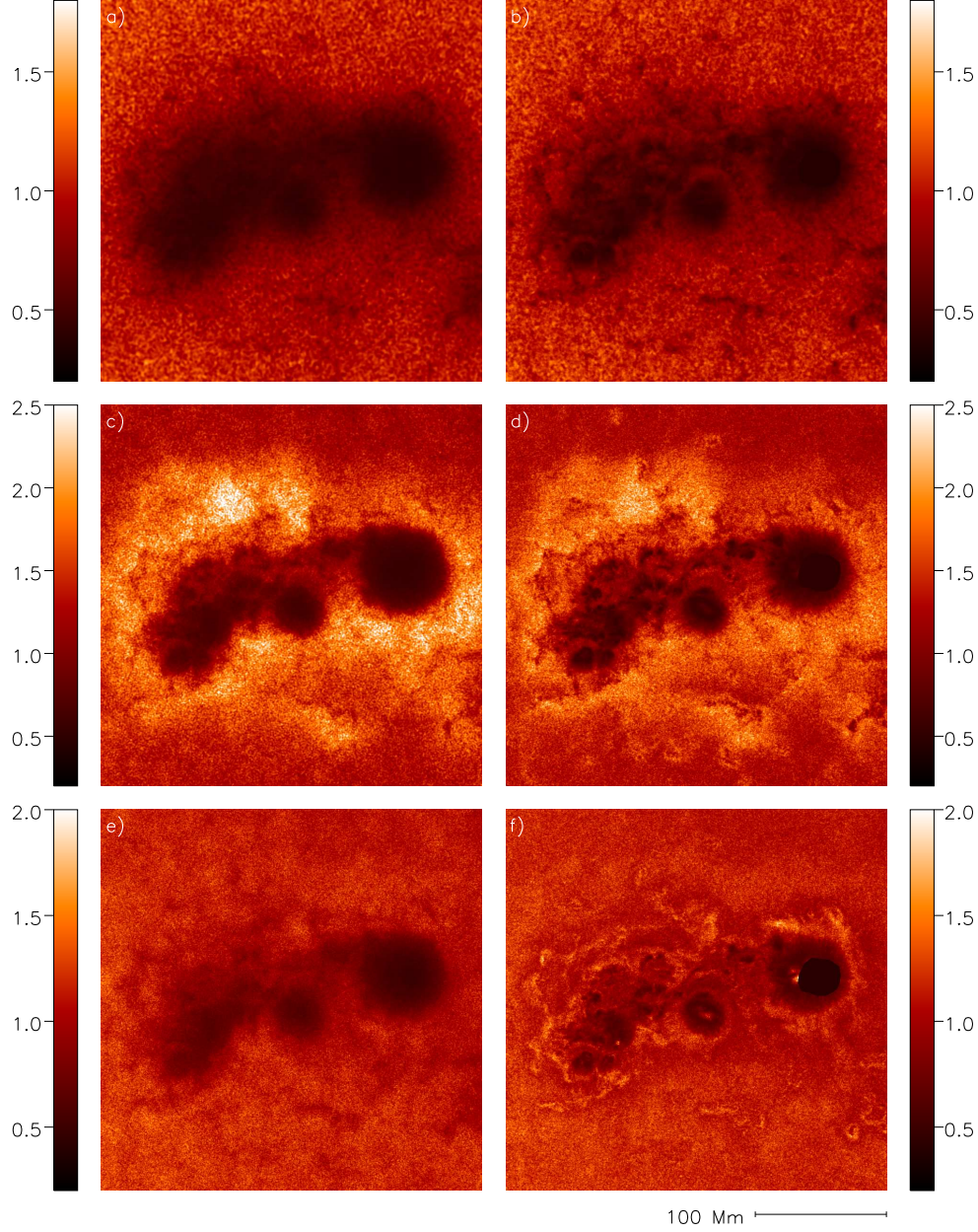


Figure 4.10: The seismic emission (left) and local acoustic (right) power maps at 3, 6 and 9 mHz (top to bottom) of the active region AR11944, normalized to the quiet sun. Due to some damaged pixels at the centre of the large sunspot, a mask is applied to prevent any artificial seismic sources appearing in the holography.

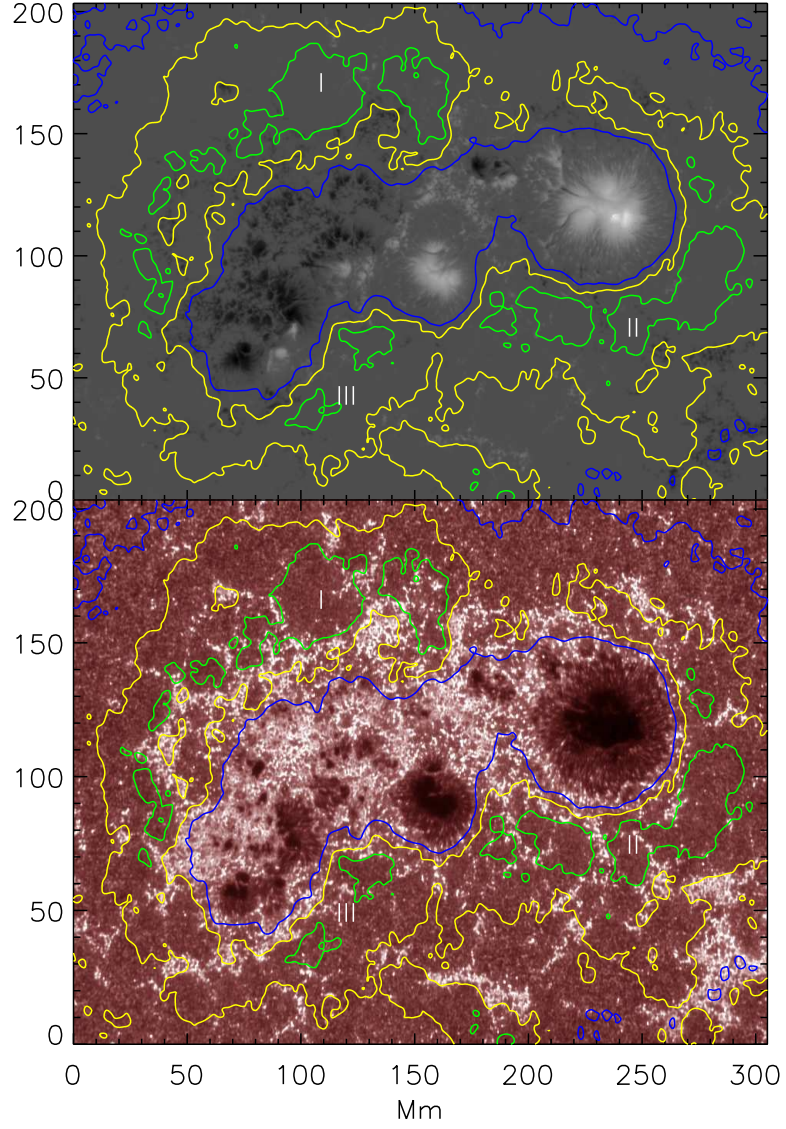


Figure 4.11: The contours of the halo (yellow), glories (green) and inner plateau boundary (blue) superimposed onto maps of B_z (top) and 1700\AA intensity (bottom) for the active region AR11944.

4.3.2 Correlations Magnetic Fields and Acoustic Power Halos

In this section, relationships between the magnetic field, seismic and acoustic power will be explored. This section has two parts. The first part examines the relationships between field strength, inclination, power and frequency when averaged over the entire region (including umbra, penumbra and quiet sun). The second section focuses on the properties of halos and glories. By isolating the halo from the ‘true’ quiet sun which is not acoustically enhanced, and used for normalization purposes, we can ascertain accurate relationships between the field and acoustic enhancement without skewing the results.

Given the similarities found between the properties of all three regions, we decided to choose the results of AR11429 as representative for the following discussions. The other active region results can be found in the Appendices. Where specified, the results of all three active regions are examined.

Active Region as a whole

Figure 4.12 shows the average power (seismic and local acoustic) of AR11429 as a function of magnetic field strength and inclination (in bins of 10 G and 10°) for three examined frequencies. The standard error of the mean power is ± 0.002 quiet sun units. From figure 4.12 some basic relationships can be deduced. Firstly, with high magnetic field strength (> 350 G) both seismic and local acoustic power pixels are in deficit, when compared to the quiet sun. However, below this field strength the average power tend towards quiet sun values, except in the 6 mHz case. At 6 mHz, the power becomes enhanced, especially in the quasi-horizontal ($< 40^\circ$) fields of intermediate strengths ($60 < |\mathbf{B}| < 150$). These averaged power values include the halo and quiet sun, hence the values are less than the actual halo enhancement (see next section). Close examination of the 9 mHz plots show the high local acoustic power spikes at high field strengths (> 2000 G) and intermediate inclinations ($\pm 45^\circ$), which correspond to the highly inclined strong magnetic fields of the umbra. These high power spikes (noted in the previous morphology section) are not apparent in the egression, which indicates they are not sources with signatures that re-emerge within our pupil.

Figure 4.13 shows the average power as a function of field strength and frequency, in two inclinations ranges $|\gamma| < 40^\circ$ (top) and $|\gamma| > 40^\circ$ (bottom). In all four frames, the average power peaks between 5-7 mHz and at a field strength between 60-300 G. The frames with a field inclination of less than 40° have a broadly enhanced power distribution (across $|\mathbf{B}|$) with a greater

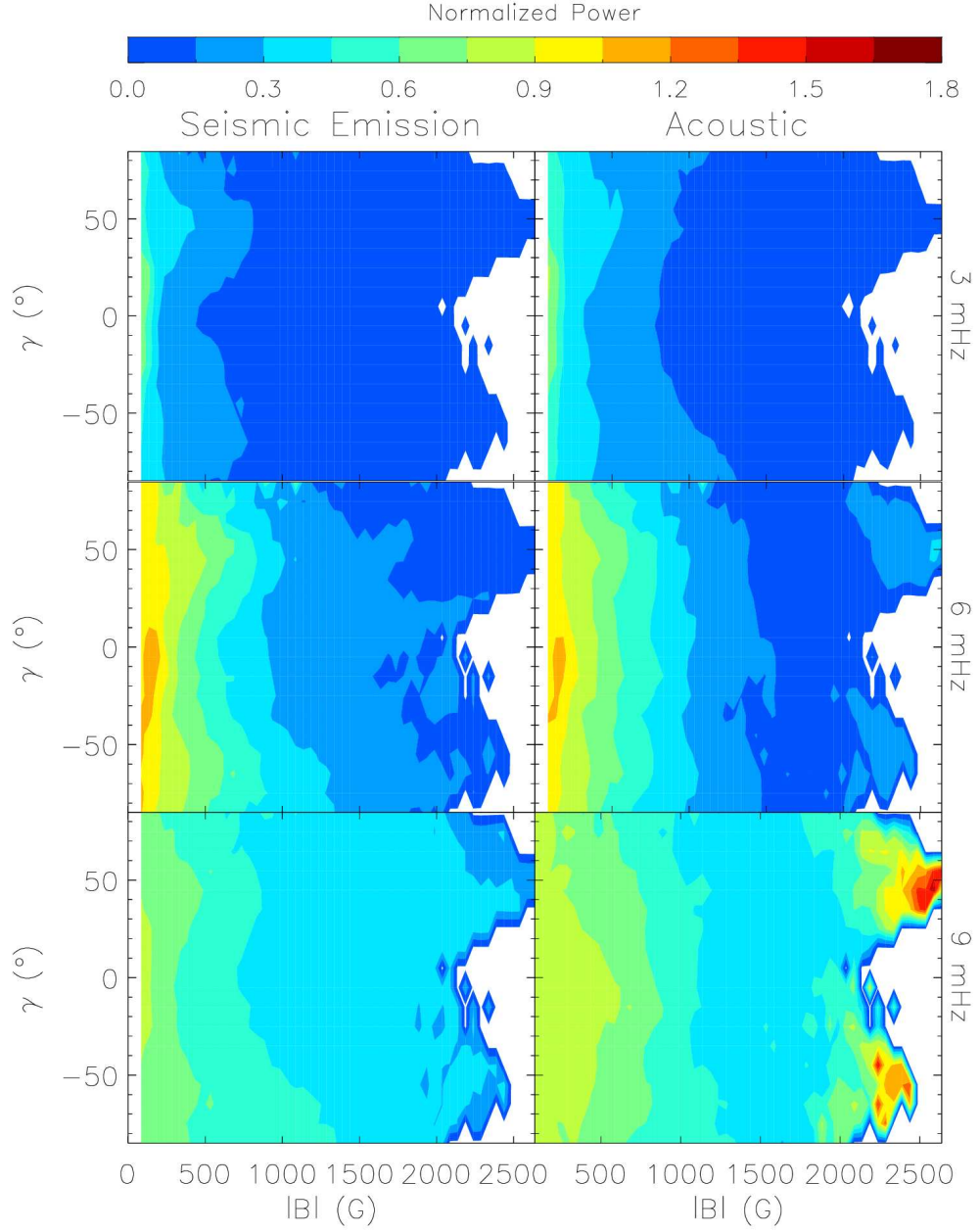


Figure 4.12: The mean normalized power of the seismic emission (left) and local acoustic (right) power as a function of $|\mathbf{B}|$ and γ of the entire map of AR11429 for 3,6 and 9 mHz (top to bottom, respectively).

power peak (> 1.4) centred at 6 mHz. Additionally, in all frames the acoustic moat is apparent below 4.5 mHz, with greater power suppression at higher field strengths and inclinations. A comparison between the two types of power maps reveal significant similarities, yet subtle differences. While both power maps peak at the same frequency and field strengths, there is more acoustic power at higher ranges and the seismic power has a greater power deficit within the frequency range of the acoustic moat. We will speculate on these differences in section 4.4.

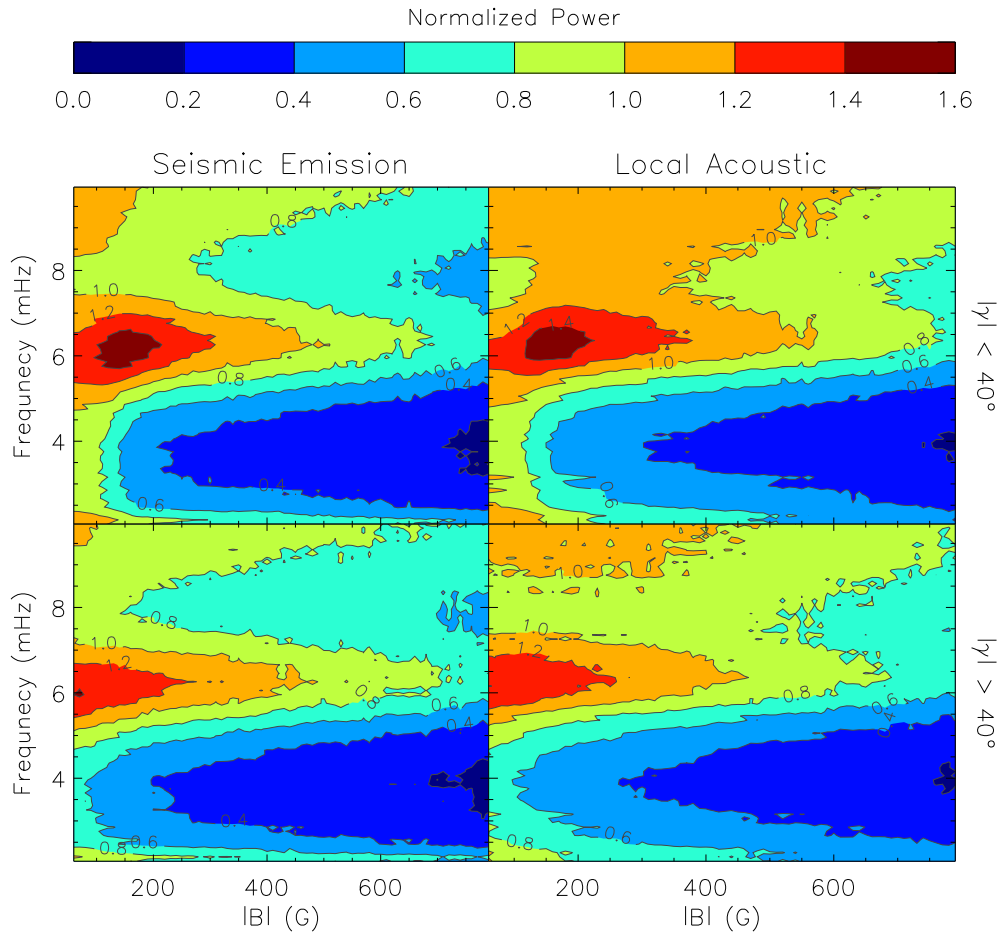


Figure 4.13: The average normalized power as a function of magnetic field strength and frequency for two different ranges of $|\gamma|$ (top: $< 40^\circ$, bottom: $> 40^\circ$). The left frame shows the seismic emission power, while the right frame shows the local acoustic oscillation power.

Power Halo

Shifting our focus to the role of magnetic fields on enhancing seismic emission, Figure 4.14 shows the average power within the halo in a similar fashion to Figure 4.12, which examined the entire region. Also it should be noted that we are only examining the pixels that lie within the seismic emission halo at 6 mHz. Hence in all panels the pixel distributions (for specific γ and $|\mathbf{B}|$) are identical, with the corresponding power being the only difference between each frame. Figure 4.14 reveals numerous morphological properties of both types of halos. 1) There is a general symmetry of pixels around $\gamma = 0$. 2) The relationship of power with frequency (shown in Figure 4.15) is reflected here, with the greatest enhancement seen at 6 mHz and suppression at 3 mHz. 3) At 3 and 9 mHz, local acoustic power generally dominates over seismic emission power (which is dominant at 6 mHz). 4) The greatest seismic emission and local acoustic power, occurs within relatively horizontal ($\gamma < 40^\circ$) and intermediate field strengths ($< 300\text{G}$). 5) At 9 mHz, the acoustic power is enhanced at greater magnetic field strengths ($> 200\text{G}$) and more inclined fields ($< 60^\circ$), while the seismic emission power is similar to quiet sun values. Figure 4.13 shows the normalized power in the entire halo as a function of frequency (bins of 0.5 mHz). It is shown that the mean seismic power dominates over local acoustic power at 5-6 mHz and 7.5-9 mHz. However, below 4 mHz, the acoustic power is dominant.

These results demonstrate the similarities between the acoustic and seismic power relationship with the magnetic field, however as stated above, there are notable differences that distinguish the two. These differences include; the extent of power enhancement, as a function of field strength and inclination, as well the halo behaviour at high frequencies. As a concluding note to this result, there also appears to be an outlier to these observations at 6 mHz, 200G and $\gamma = +80^\circ$, which is greatly enhanced in both power types. This does not occur at different time frames (see Appendix A) indicating that at the chosen time of this magnetic field map, the field properties of a glory were changing.

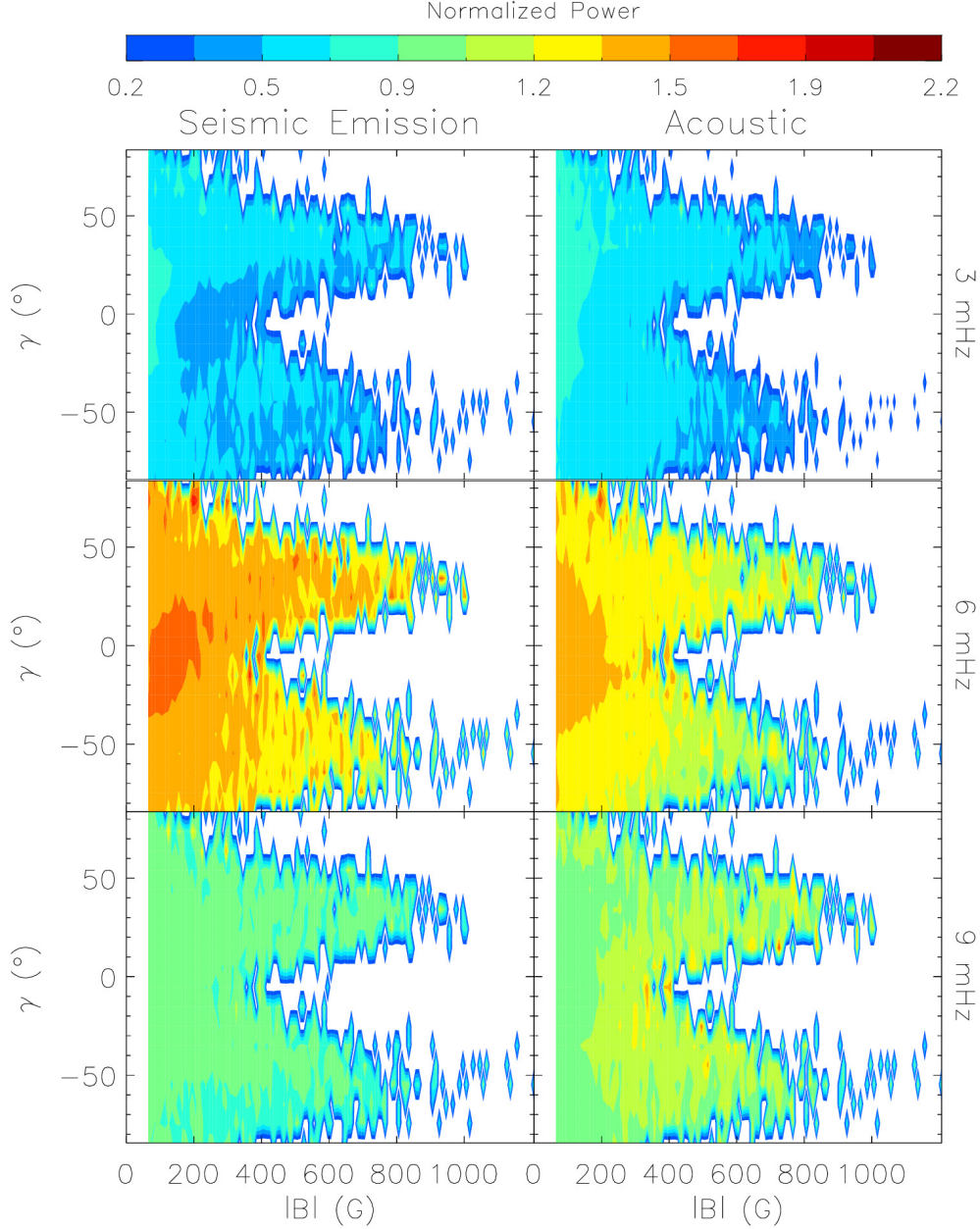


Figure 4.14: The mean normalized power within the AR11429 halo of the seismic emission (left) and acoustic (right) power for 3,6 and 9 mHz (top to bottom, respectively).

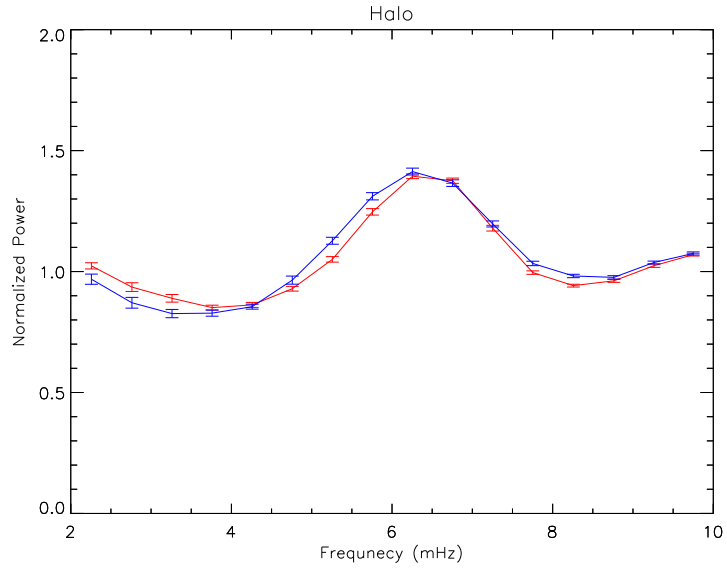


Figure 4.15: Average seismic (blue) and acoustic (red) power within the halo, as a function of frequency. The data is averaged into bins of 0.5 mHz and associated error bars shown. The halo region is enhanced in the high frequency range, with seismic power dominating of the local acoustic.

Table 4.3. Average pixel values within the examined regions

AR	Map	I	II	III	Halo	Plateau	QS
AR 11158	3mHz ($ H_+ ^2/ \psi ^2$)	0.58/0.69	0.59/0.71	0.66/0.74	1
	6mHz ($ H_+ ^2/ \psi ^2$)	1.89/1.70	1.54/1.45	1.18/1.15	1
	9mHz ($ H_+ ^2/ \psi ^2$)	1.10/0.92	1.00/0.96	0.98/0.97	1
	$ B $ (G)	85	105	133	46
	γ ($^\circ$)	-4	-1	2	-7
	I_{uv}	0.95	1.16	1.33	1
AR 11429	3mHz ($ H_+ ^2/ \psi ^2$)	0.68/0.80	0.59/0.71	0.73/0.87	0.68/0.78	1.03/1.07	1
	6mHz ($ H_+ ^2/ \psi ^2$)	1.98/1.70	1.95/1.70	1.91/1.74	1.65/1.50	1.10/1.09	1
	9mHz ($ H_+ ^2/ \psi ^2$)	1.07/0.99	1.07/0.99	1.12/1.05	1.02/1.03	1.11/1.15	1
	$ B $ (G)	90	94	84	130	267	60
	γ ($^\circ$)	-6	-7	-13	-7	-12	2
	I_{uv}	0.89	0.92	1.08	1.2	1.76	1

Table 4.3 (cont'd)

AR	Map	I	II	III	Halo	Plateau	QS
AR 11944	3mHz ($ H_+ ^2/ \psi ^2$)	0.54/0.60	0.49/0.55	0.49/0.61	0.44/0.61	0.30/0.40	1
	6mHz ($ H_+ ^2/ \psi ^2$)	2.00/1.76	1.96/1.62	1.93/1.64	1.64/1.47	1.22/1.14	1
	9mHz ($ H_+ ^2/ \psi ^2$)	0.90/0.90	0.84/0.81	0.99/0.84	0.89/0.9	0.76/0.89	1
	$ B $ (G)	107	101	92	123	239	61
	γ ($^\circ$)	-1	1	-3	-5	-8	0
	I_{uv}	1.32	1.16	1.06	1.38	1.89	1

4.3.3 Seismic Glories

To distinguish regions of different seismic emissivity, we have identified seven regions of significantly enhanced seismic emission within the three active region halos (see green contours in Figures 4.5, 4.8 and 4.11). Table 4.3 shows a summary of the total seismic/acoustic power averaged over the defined areas, along with estimates of the mean magnetic field strength, inclination and the normalized 1700Å values. These regions are clear of magnetic structures such as plage and this lack of magnetic fields is also reflected in the 1700Å maps, devoid of both high and low intensity pixels. However, these glories still contain some magnetic properties. Specifically, the magnetic field strength varies between 85-128 G, with a near-horizontal average inclination angle ($\pm 10^\circ$). In comparison, the quiet sun magnetic field strength is around 60 G, though as discussed previously this is possibly noise. Of all seven zones, the zones located around the large active region AR11944 were found to be the most intense seismic emitters and this is seen to a lesser extent in the oscillation power maps. Similar to the average power within the halos, the acoustic power within glories is less than the seismic emission power (which is generally 120-130% quiet sun units). Remarkably for each active region, the mean power of its associated glories are relatively similar to each other. This similarity may indicate that the degree of excess power within the glories may be associated with the active region, not the location of the glory.

To further expand on the relationship between glories and the magnetic field, we examine all of the seismic glories identified in the three active regions. Figure 4.16 shows that seismic glories are 197% (with $\sigma = 0.24$) more powerful than the quiet sun, while the acoustic power is 170% ($\sigma = 0.22$). The peak magnetic field strength is below our error minimum, indicating that the field strength is near quiet-sun values. However, the distribution of magnetic field strength within the glories is broader than the quiet sun, with the maximum field strength within these regions reaching around 200 G. The distribution of field inclination within the glories is different to the quiet sun ($\mu = 1^\circ, \sigma = 19^\circ$), with a large majority (53%) with $\pm 10^\circ$ of horizontal and the remainder within $\pm 40^\circ$.

We conclude by examining the power correlation between the two types of power maps. Figure 4.17 shows a scatter plot of pixel values of the two types of power maps for Region I of AR11429. These results show that within the glory the seismic emission power generally dominates over the local oscillation power. The length of the error bars are a standard deviation of the data. This dominance is fairly consistent with the mean average seismic and acoustic

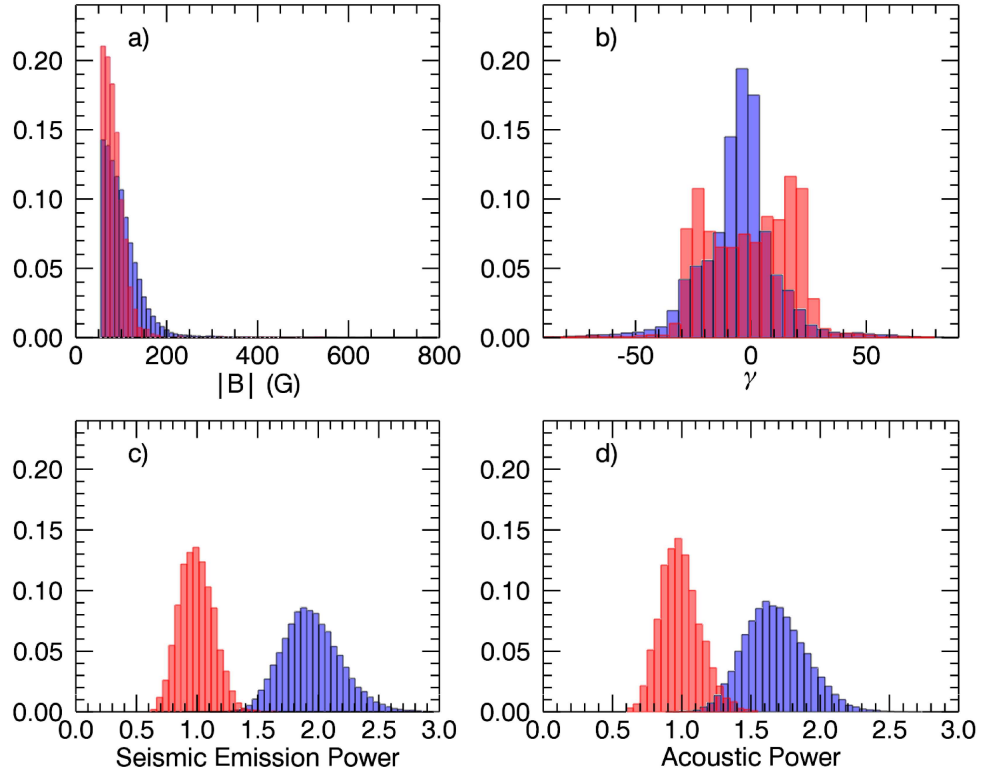


Figure 4.16: Histogram plots of the seismic emission glory (blue) compared to the quiet sun (red). The histograms are normalized to the number of pixels within the region. The glory has a mean seismic power 97% greater than the quiet sun, while the acoustic power is only 70%. When compared to Figure 4.18 the seismic glory has a compact distribution over a small magnetic field strength, while also the distribution across field inclination is narrow and centred on a horizontal field.

power in all examined regions (see Table 4.3).

4.3.4 The Seismic Plateau

The seismic emission power maps at 6 mHz have revealed an intermediate power belt ($1 \leq |H_+|^2 \leq 1.4$) that is situated between the emission halo and the penumbral boundary of each active region. We refer to this region as a *seismic plateau* (see blue contour of Figures 4.5, 4.8 and 4.11) where the average seismic power is 110-120% quiet sun values. This region contains numerous pixels with high field strength values and therefore the number of accurate pixels is high (i.e. 90% for AR11429).

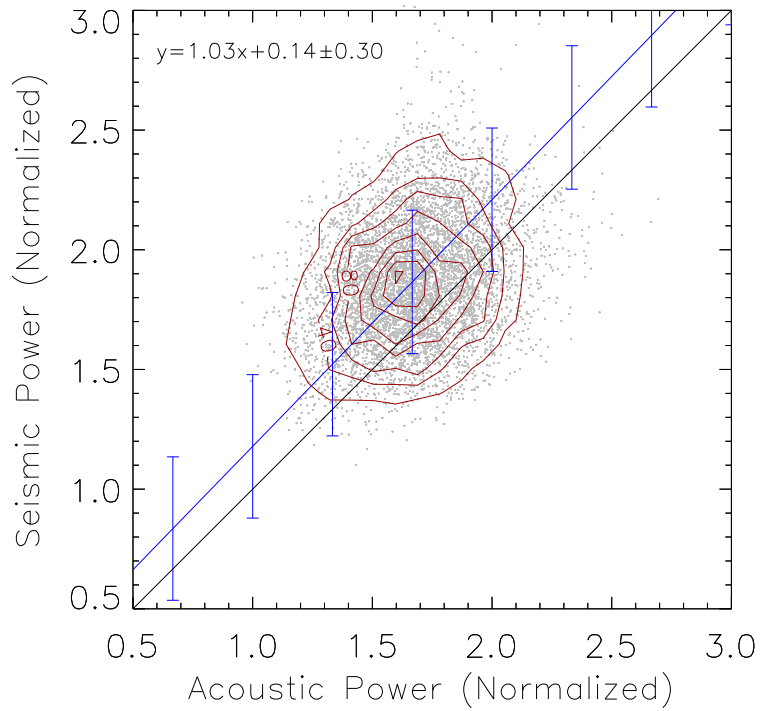


Figure 4.17: The power correlation between seismic emission and local acoustic oscillations. The area sampled is Region I of AR 11429. The orange contours show the density distribution of the points, with the greatest density at (1.6, 1.9). The line of best fit is shown by the blue line, compared to a purely linear relationship (black line). The error bars are the standard deviation of the data (± 0.2996).

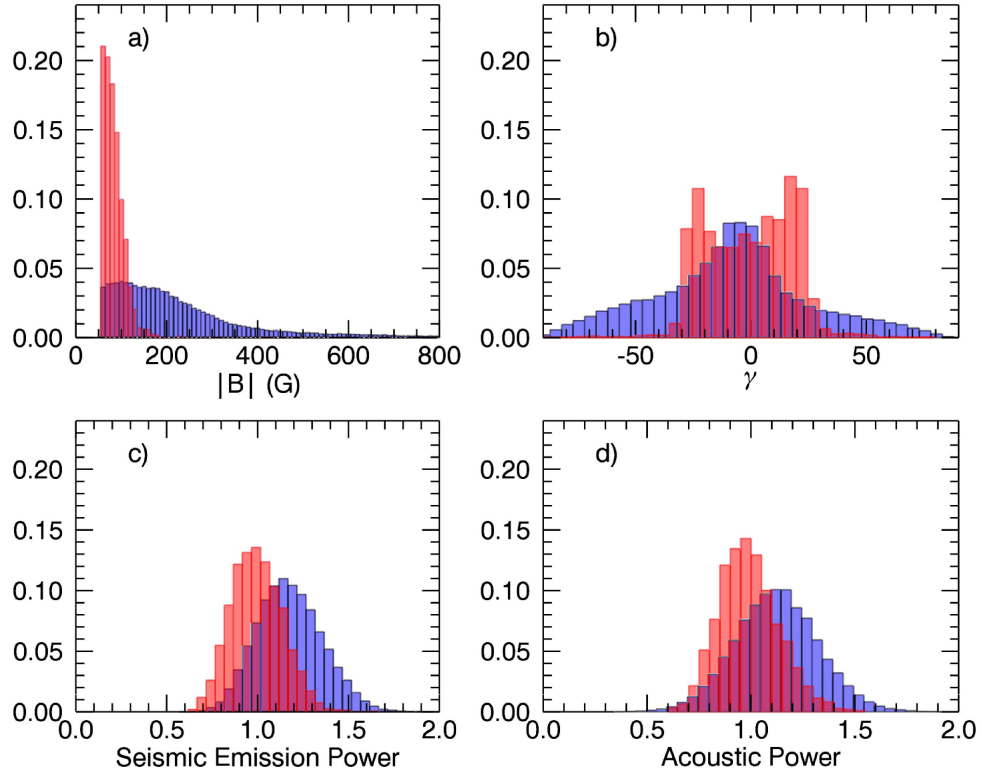


Figure 4.18: Histogram plots of the seismic plateau (blue), compared to the quiet sun (red). The histograms are normalized to the number of pixels within both regions. The seismic plateau has a 10% larger mean acoustic and seismic power, compared to the quiet sun. However, the magnetic field strength and inclination is broader.

From the magnetic field maps it can be seen that these regions contain a large proportion of magnetic plage. Figure 4.18 shows that while the seismic emission and acoustic power have a mean value close to that of the quiet sun ($\sim 110\%$), the magnetic field morphology differs significantly. The plateau field strength has a broad peak between 60-200 G, while the field distribution is broader than the quiet sun, with values greater than 400 G. The field inclination is also broadly distributed across all angles with most pixels within $\pm 70^\circ$ from horizontal. Referring to the AIA images (and Table 4.3) it can be seen that the seismic plateau has high pixel values (1.7-1.8 quiet sun values) indicating the presence of closely bundled field lines at the 1700\AA formation height.

4.3.5 Spatial Correlations: Seismic versus Local Acoustic Power

In this section, we examine the spatial correlation between the most intense local acoustic and seismic emission power kernels. Figure 4.19 shows filled contours of the most powerful kernels of the local acoustic (blue) and seismic emission (red) power (at 70% of their respective peak values) within glory region II (AR11429). The background maps show the total magnetic field strength (saturated at 400 G), inclination, intensity continuum and the local acoustic power of region II.

In general, the large scale spatial correlation is good, with the kernels located within an area situated between regions of high magnetic field strength and inclination. However, this correlation is weakened when examining the alignment of the individual kernels with respect to each other. Locations where the kernels do not align, may suggest the presence of seismic signatures that resurface within the pupil, but are not apparent in acoustic maps due to dampening by local oscillations. Conversely, convective motion may aid in enhancing local acoustic oscillations and as such do not appear as a seismic signature. However, our pupil collects Doppler signals from magnetic areas of the active region, where local oscillations are attenuated. These magnetic fields act as an “acoustic shower-glass” (Lindsey and Braun 2005) and will impact our assessment of seismic emissivity near magnetic fields and its relationship with the local oscillation power. Efforts to correct this “shower-glass” effect may address the lack of spatial correlation.

Figure 4.20 shows the same contours of the seismic and acoustic kernels on the AIA 1700Å image. The darker pixels of the background image show that 1700Å emission values are close to quiet sun values. Again we see how closely the $1.4 \times |H_+|^2 / |H_{+0}|^2$ contour follows the enhancement of the 1700Å channel. Close examination of the 1700Å channel suggests that enhancement should occur in the quiet sun region located to the solar west (due to near quiet sun values), yet there appears to be significantly smaller enhancement. We are not sure why this is, and speculate in the conclusions.

In seismic holography we are limited to examining signatures at and below the surface. In the statistical results of the previous sections, we have included the normalized 1700Å values, since the formation height is relatively close to the 6173Å detected by the vector camera. However, comparisons to other AIA data sets, which have formation heights out to $1.2 \times R_\odot$, can not be as direct. As the study of acoustic halos at different heights has already been examined (Rajaguru et al. 2013), we qualitatively compare the seismic emis-

sion halo to the magnetic field structure above the photosphere as seen by AIA’s EUV channels. Figure 4.21 shows a slice of AR11429, including glory regions I and II, in six wavelengths. The glories are located in the quiet sun patches seen to the south and north in the 1700Å and 1600Å images. The other channels (especially 171Å) show large magnetic loops extending outward from the active region, over these glories. Keeping in mind that line of sight issues greatly affect any visual interpretation of these magnetic structures, we speculate that the glories are below the horizontal part of these loops, underneath what is known as the magnetic canopy. We will discuss the implications of a canopy further in section 4.4

4.4 Discussion and Conclusions

We have used high-resolution HMI and AIA images to explore relationships between enhanced seismic emission and local acoustic oscillation power observed in the halos of active regions. In this study, we have taken significant statistical precautions in examining the weak magnetic fields in the region of the halo. Our main conclusions may be summarized as follows:

- 1) The complex multi-polar active regions have large patches of enhanced seismic emission localized mainly in magnetically “quiet” areas surrounding the penumbrae;
- 2) We have been able to determine accurate statistical relationships between the enhanced seismic emission and the local magnetic field morphology;
- 3) Seismic emission is enhanced at 5-7 mHz within regions of horizontally inclined magnetic fields with intermediate field strengths of 60-200 G;
- 4) A plateau of intermediate seismic power has been defined;
- 5) Field properties of the halos indicate that it is situated within horizontal fields ($\pm 40^\circ$);
- 6) The morphology of the seismic emission halo and local acoustic halo are similar in many ways, but differ at high frequencies and in degree of power enhancement;
- 7) There is a strong relationship between significantly enhanced seismic sources (glories) and a horizontal magnetic field morphology of intermediate strength;

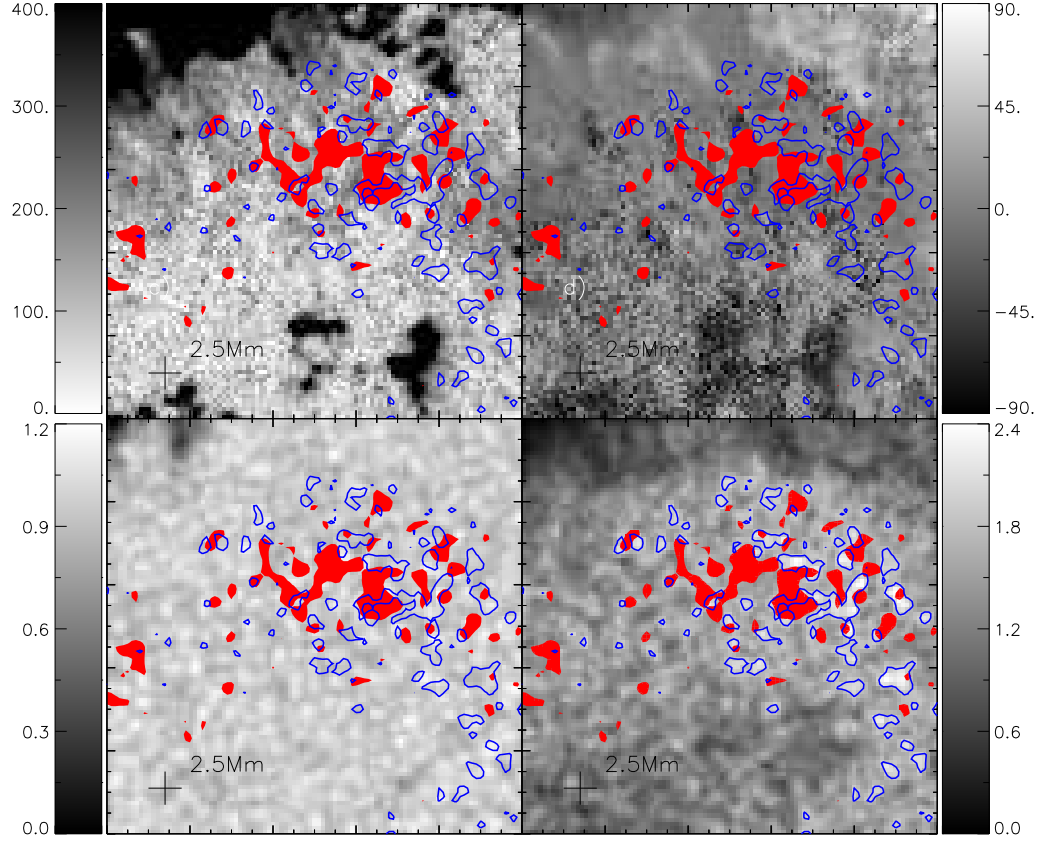


Figure 4.19: Filled contours of the acoustic (blue) and seismic emission (red) power of the enhanced region II (AR11429) at 6 mHz, overlaid on maps of the $|B|$ (where pixels of $|B| > 400$ are saturated), γ , Intensity Continuum, and local acoustic power at 6 mHz (top left to bottom right). While both contours are localized in a large-scale fashion, examination of the individual kernels reveals a weak spatial correlation.

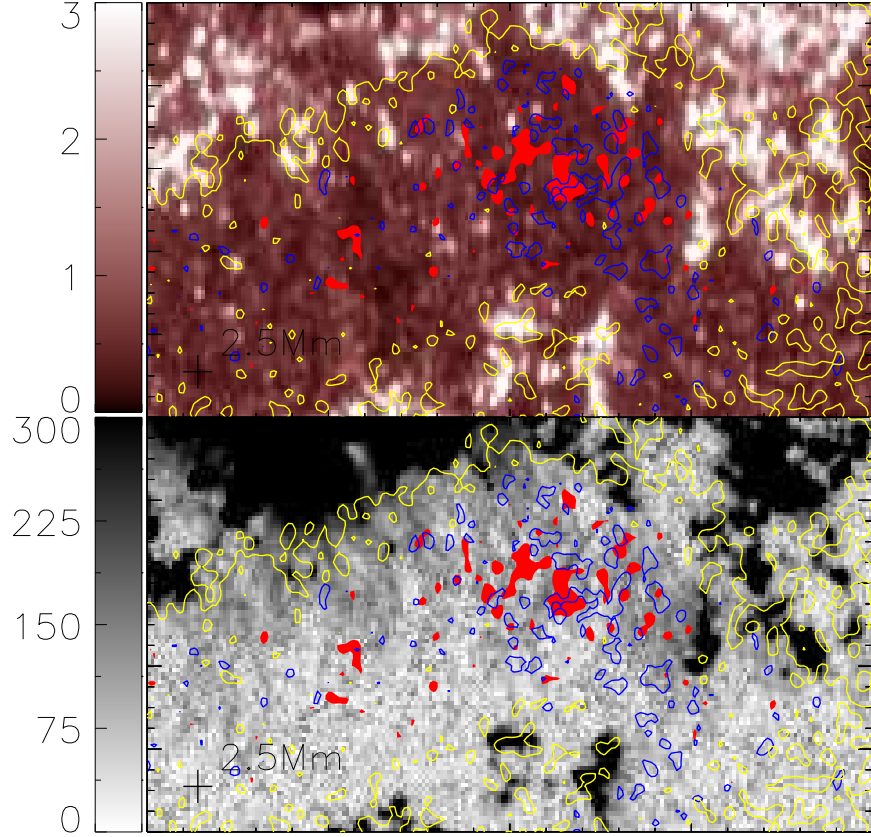


Figure 4.20: Filled contours of the acoustic (blue) and seismic emission (red) power at 6 mHz of the enhanced region II, overlaid on maps of the 1700Å AIA channel (top) and $|B|$ saturated at 400G (bottom). The $C_{1.4}$ contour borders the enhanced pixels of the 1700Å map. Close scrutiny of the kernel locations show that they are located within relatively quiet regions, close to the strong fields of the active region.

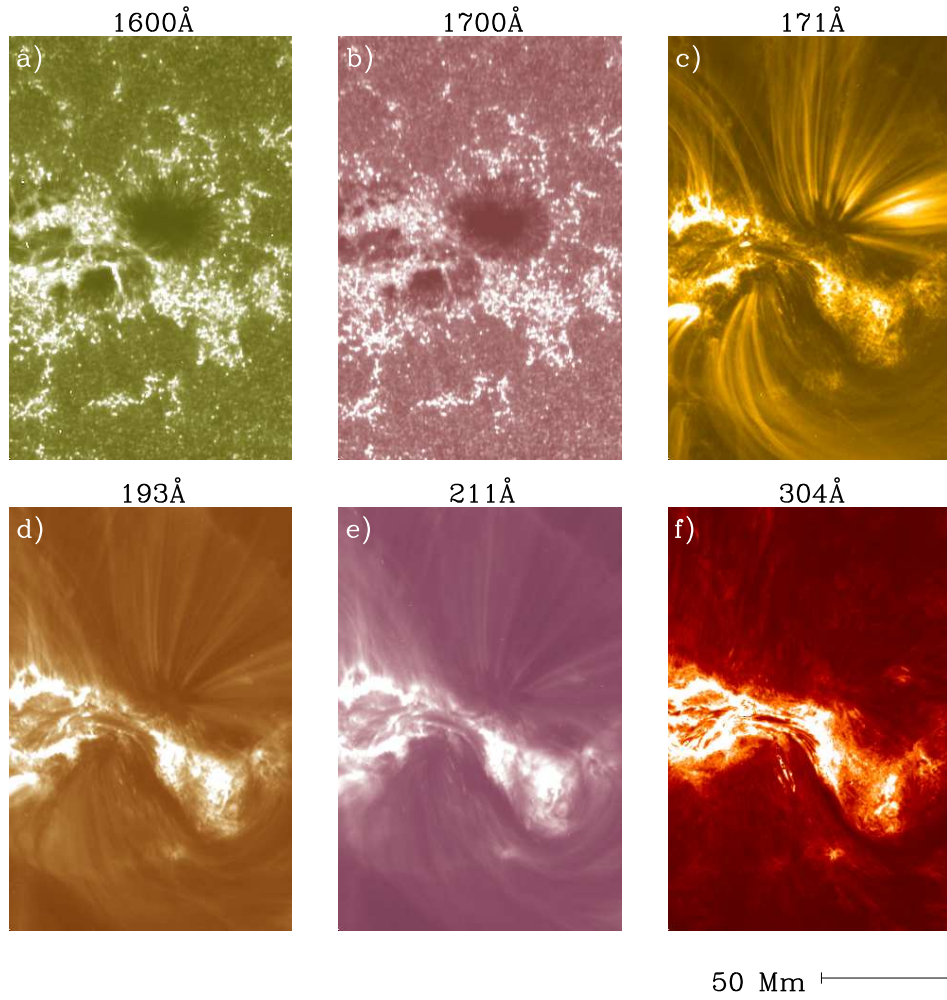


Figure 4.21: Slices of the AIA images of AR11429. The wavelengths in each image are as specified. In the 1600Å and 1700Å images the seismic glories (region I and II) are located in quiet sun patches located to the north and south.

- 8) There is no exact spatial correlation between the local seismic power and local oscillations in the halos.

Our results compliment those of previous studies (Schunker and Braun 2011; Rajaguru et al. 2013), which agree that a relationship exists between the enhanced local acoustic power and the magnetic field. However, these studies were unable to differentiate seismic sources from other acoustic oscillations (e.g. convection), but we have achieved this through the use of holography. We have thoroughly examined the magnetic morphology of three distinct regions of seismic emission: the halo, glories and what we refer to as the ‘seismic plateau’. In examining these regions, it was found that seismic emission is also greatly influenced by the magnetic field, with enhancement occurring within regions of near-horizontal field inclination. However, regions interwoven with magnetic plage (such as the plateau) hinder seismic emission, producing near quiet sun power belts situated between the enhanced halo and the strong magnetic fields of an active region.

With regards to the relationship between the local acoustic power and seismic emission power, we find a strong similarity. Both halos show the greatest enhancement in the same frequency range and magnetic field morphology. The similarity in these results is to be expected considering that the seismic emission calculated by holography is a subset of the wave field that produces the local acoustic power maps. Yet, examination of spatial correlations show that localized acoustic noises may hinder the high powered local acoustic kernels that are seen in seismic emission maps. Furthermore, it is possible that local emitters submerged just below the photosphere emit different amounts of energy in an upwards direction, when compared to the downwards direction. For example, if the energy upward (contributing to the local oscillations) was different to that emitted downward (contributing to the signals sampled in the pupil) then one would expect to see the power differences reported in this study. We understand this would not be the case if the emitters were simple dipoles or quadrupoles, however it is possible to contrive coherently related combinations of dipoles and quadrupole emitters that support this.

The current study provides a wealth of information on the seismic sources surrounding complex active regions, however the question of what mechanism is responsible has yet to be answered. Our results concerning field inclination and power enhancement are consistent with mechanisms, such as mode-conversion (Khomenko and Collados 2009) and the trapping of waves (Kuridze et al. 2008), that require a near horizontal magnetic field structure.

Such a structure is known as the magnetic canopy, which spans over quiet sun patches (or single granules) located near active regions. These canopies have previously been linked to acoustic power halos (Muglach et al. 2005) and our inspection of the AIA images (keeping in mind our caveats) appears to support this.

With regards to the trapping of waves, Kuridze et al. (2008) suggested that a small-scale canopy above a solar granules (on scale of ~ 0.5 Mm) will create a field-free cavity below, in which waves are trapped and enhance the local Doppler signature. While the model was very simple (i.e. cold-plasma, unstratified etc.), one would expect to see evidence of this process as seismic sources restricted to within granular regions. The diffraction limited (2.5 Mm) maps of holography are unable to resolve these small emitters. However, to generate the observed seismic halo and glories, these small cavities would have to be located closely together, be broadly distributed and have lifetimes on par with the observation time frame. With regards to the mode conversion process, fast waves with frequencies above the acoustic cut-off travel to chromospheric heights to be refracted and converted into slow-waves. This process is sensitive to field inclinations (Cally 2006), and should generate additional seismic sources in horizontal field regions, where a majority of the fast wave is returned to the surface. The change in the morphology of local acoustic halos with chromospheric height (Rajaguru et al. 2013) compliments this theory and our analysis of the seismic emission halos confirms that seismic sources are significantly enhanced within regions of near-horizontal inclinations, as suggested by mode conversion. We note that recent forward modelling work by Rijs et al. (2015) presents results suggesting fast-wave refraction can produce the observed seismic emissions.

Although canopy related mechanisms may account for the seismic halo, they are unable to clearly explain the presence of glories. If the magnetic field in glory regions was quasi-horizontal (ideal for enhanced seismic sources), while the field in the halo was more inclined, then it is possible that glories are the result of mode conversion. However, a sustained horizontal field is unlikely as the configuration will change in these localized regions over the 24 hours that the power maps are integrated. Although regions with an average near-horizontal field (compared to nearby field lines) are plausible. In order to ascertain whether these canopy mechanisms are responsible for glories, an investigation into the evolution of the canopy and the presence of small intense seismic sources needs to be performed.

Hindman and Brown (1998) suggested that kink motion of magnetic flux tubes could deposit additional energy into the photosphere. This addition of

energy into regions already enhanced by canopy related mechanisms, could give rise to glories. However, this concept presents two problems that will need addressing. Firstly, it's unlikely that the kink mode is responsible for any observed additional vertical oscillations, as it is transversal in nature and any motion of the plasma will not be seen in Doppler images near the disk centre. We suggest that if tube motion is responsible, then it is most likely sausage motion, in which the compression of plasma would add to the vertical velocity profile (see Figure 1.4). The second issue is a question of flux tube lifetimes. Anchored flux tubes (in the surrounding photosphere) are generally located at granular boundaries and any motion of these tubes would have the same lifetime as the solar granules (on order of minutes), adding little to the power maps over 24 hours. We suggest the presence of seismic glories is probably due to some small scale dynamical process, that has yet to be understood in terms of sustained enhanced seismic emission.

While we have discussed the agreement of our results with some proposed mechanisms, there need to be further observational studies into the nature of the magnetic fields, the plasma- β heights, magnetic canopies and their relationship with the oscillation and emission power halo. Furthermore, theoretical and numerical models need to be developed, improved and tested against observable parameters to better understand the mechanism responsible for the enhanced seismic sources surrounding complex active regions.

Chapter 5

Summary and Future Prospects

In this chapter, a summary of the research outcomes from chapters 2, 3 and 4 will be presented. Firstly, a short overview of the semi-analytical model developed and implemented in chapters 2 and 3 will be presented, followed by a review of the case study results. Then a conclusion of the analytical study of this thesis will be given by discussing the future prospects of modelling thin flux tube ensembles. The next section will begin with an outline of the main insights gained in the study of seismic sources located near active regions. We briefly highlight relationships with the magnetic field and the main similarities and differences found between seismic and local acoustic power. We will conclude this section with an overview of the future prospects in studying power halos.

5.1 The Behaviour of Flux Tube Bundles

Since the discovery of the 5-minute oscillations, the field of helioseismology and in turn our understanding of the sun, has grown rapidly. Braun et al. (1988) was amongst the first to establish the strong interactions between solar acoustic waves and the magnetic fields of active regions. Consequently, these observations have raised questions about possible mechanisms driving the absorption and phase-shifts of solar p -modes, which are readily detected within magnetic features.

In the first part of this thesis, the semi-analytical formalism of Kagemoto and Yue (1986) (adapted for solar application by Hanasoge and Cally 2009) was introduced, with several key changes applied, in order to explain the absorption of solar p -modes within small scale magnetic features. Our first key change introduced sausage motion into the formalism, allowing any thin tube within a system to interact through the scattering of $m = 0$ waves. Although, the kink mode has previously been examined in the context of the multiple scattering regime (Hanasoge and Cally 2009), a system with both sausage and kink motion has not. By allowing the tubes to interact through both modes, the absorption profiles of the system change dramatically. In the case studies of Chapter 2, it was shown that these changes were significant when the tubes were within close proximity ($d < \lambda/2$). Another key change resulted from the lack of symmetry between $m = \pm 1$ modes shown by Hanasoge and Cally (2009). This lack of symmetry was found to be incorrect and arose from an inappropriate near-field solution. However, upon choosing the appropriate solution, our results agreed with recent numerical studies by Felipe et al. (2013).

While previous unstratified studies have shown that a multiple scattering regime exists within tight bundles of tubes, we confirm the presence of this regime in stratified cases and conclude that the near-field plays the most significant role. Without the near-field, scattering is only due to the far-field, which is small in comparison. Finally, it was shown that the properties of the incident wave (frequency and m) will affect the extent of the multiple scattering regime, in particular, the observable absorption and phase shift. Overall, the results of the two tube case studies agree with numerical studies and offer a deeper insight into how the multiple scattering regime enhances the absorption of a flux tube bundle.

The second stage of the semi-analytical study was presented in chapter 3 (Hanson and Cally 2014), and involved the extension of the model to include numerous flux tubes. Various ensemble structures and properties were ex-

plored, with results showing the effect these had on the multiple scattering regime. Motivated by the results of Braun (1995), the model was further developed to include $|m| > 1$ waves, which are known to interact with solar plage. It was shown that while these waves could not directly interact with the tubes, they could be indirectly absorbed through the interaction of their $|m| \leq 1$ components. In the case studies, morphological parameters such as flux tube properties (β , Φ_f), position and symmetry were found to play a significant role in the overall scattering properties of an ensemble. Additionally, it was shown that small ensembles could mimic flux tubes of greater magnetic flux by producing similar absorption and phase-shift profiles across m . As with the flux tube pair cases, these ensemble studies are in agreement with numerical studies, and hence represent a significant step in understanding the role of the multiple scattering regime in large ensembles.

Overall, this model presents a computationally inexpensive (for moderate numbers of tubes) and mathematically enlightening approach to investigating the multiple scattering regime. However, it is still simple and will require further adaptations in order to be more physically accurate. In particular, while the stratification of the atmosphere has introduced an energy-loss mechanism at the bottom of the tube, the model has a stress-free boundary condition at the top which prevents waves escaping into the upper atmosphere. By allowing the tube waves to escape through the top boundary into the above chromosphere, the absorption and phase-shifts of the tube will change. To address this energy escape mechanism, Gascoyne et al. (2014) placed an isothermal atmosphere above a polytrope. As a result, energy can be extracted from the tube waves, in the form of p -modes, which travel within the isothermal atmosphere. Gascoyne et al. (2014) showed that the stress-free boundary condition applied in this thesis, is valid for frequencies under ~ 3.5 mHz. However, once the frequency approaches the acoustic cut-off, energy loss into the upper atmosphere must be considered. In light of the results of Gascoyne et al. (2014), the next logical step for our model is to include an isothermal atmosphere on top of the polytrope. Since the acoustic waves below the acoustic cut-off, in non-magnetic regions, are unable to travel into this upper atmosphere, any matching of the wave fields will be restricted to the tube. Gascoyne et al. (2014) matched the sausage mode at the top tube boundary through the continuity of the vertical displacement and Lagrangian pressure perturbation. Similarly in our model, the kink modes will also need to be matched at the boundary through the radial displacement. We suspect that the addition of the upper atmosphere will significantly change the absorption, phase-shift and the extent of the

multiple scattering regime

There is still a lot of work required in order to understand the interactions between constituent tubes of a flux tube bundle. In recent years, numerical and analytical studies have come a long way in explaining the behaviour of waves with small magnetic structures. However, further advancements in both these approaches are required in order to compare with observational statistics. Additionally, with the improved observational capabilities of instruments such as those on SDO and Hinode, the accurate probing of subsurface structures may not be that far away.

5.2 Enhanced Seismic Sources

The phenomenon of enhanced acoustic power surrounding active regions has been a mystery for the last few decades. In this thesis, observational statistics has been presented in order to understand the morphology and significance of the magnetic field in generating additional seismic sources. We have used the helioseismic holography technique to discriminate oscillations that generate acoustic waves, which re-emerge some distance away, from other localized oscillations. With the capabilities of HMI, we have been able to generate and examine the seismic source maps of an active region at unprecedented resolutions. Furthermore, unlike previous holography studies we have made direct comparisons with the magnetic field morphology.

In Chapter 4, the SDO data of three complex active regions was examined. The study applied numerous precautions in order to obtain accurate statistical relationships between observables. It was shown that magnetic fields of intermediate strength (60-200 G) coincide with locations of enhanced seismic emission. Additionally, the halos were predominantly located in regions of field inclinations within $\pm 40^\circ$ from horizontal, while the highest powered emitters (glories) coincided with fields closer to horizontal ($\pm 10^\circ$). Comparisons were made with the commonly used local acoustic power maps, and significant similarities were reported. However, close scrutiny of the two power maps revealed a differing behaviour between enhanced seismic sources and local oscillations at very high frequencies. Local acoustic oscillations were still enhanced at 9 mHz, while the seismic sources were indistinguishable from the quiet sun. Additionally, the differing degree of enhancement (relative to quiet sun) within each map depended upon the frequency examined. This study identified three regions of differing seismic emissivity which included the halo, glories and a near quiet sun belt referred to as the seismic plateau.

In examining these regions, the morphology of the magnetic field (strength, inclination and concentration) was found to play a significant role in either hindering additional seismic sources (high field strengths and/or inclinations) or aiding them (horizontal fields of intermediate strength). These results are in agreement with the studies of Schunker and Braun (2011) and Rajaguru et al. (2013), though further observational statistics need to be gathered with regards to how the above magnetic canopy is related to seismic sources.

The use of the helioseismic holography technique on HMI data has enabled this study to explore seismic sources that surround complex active regions at high resolutions. Thus far, no other study has done this. Though we have limited the use of holography to the 6173.34\AA observation height of 140 km, this does not mean future studies are similarly restricted. Recently, Rajaguru et al. (2013) used the outer pair of filtergrams on HMI ($\pm 172\text{m\AA}$) to calculate Doppler images corresponding to a height of 20 km. Furthermore, it is possible to calculate other multi-height Dopplergrams (Paul Rajaguru, Private Communication) from the HMI data, which could be used by holography. By using these images and comparing them to models, the relationship between seismic sources and height can be identified.

However, the various limitations of holography need to be addressed in order to obtain more accurate results. Of these limitations, the “Acoustic Shower-glass” effect is the most important, so that the behaviour of acoustic waves within the magnetized photosphere can be understood. Currently, the holography technique does not consider the effect magnetic fields will have on the ray path that waves follow from the source to the pupil locations. By addressing this, the cause for the lack of spatial correlation between seismic emitters and local acoustic power kernels maybe resolved.

Thus far, HMI and AIA have provided sufficiently high resolution images of the acoustic and seismic power halos. To further understand this phenomenon, this data needs to be compared with complex models in order to identify the mechanisms responsible. In the context of granular canopy trapping, or flux tubes motions, the current capabilities of SDO are insufficient to observe such small scale phenomenon to a satisfactory resolution. However, the 4m Daniel K. Inouye Solar Telescope (DKST, formerly ATST) (ground based), which is set for operation in 2019, will provide unprecedented high resolution ($0.03''$ - $0.08''$) images of the solar magnetic field and may present answers on the role these small-scale mechanisms play in enhancing local oscillations. However, the images will still need to be compared to the continuous imaging of SDO, in order to comprehend the relationships between the halo and magnetic fine structures.

The study presented here has expanded upon its predecessors' results (Braun and Lindsey 1999; Donea et al. 2000; Donea and Newington 2011) to further explore the application of helioseismic holography in ascertaining relationships with the magnetic field and comparing them with the commonly used local acoustic power maps.

Appendix A

Statistical Precautions

This Appendix presents figures that support the statistical precautions carried out in Chapter 4. Figure A.1 shows the histogram plots of the three quiet sun patches used to normalize each of the active regions' power maps. The histograms are normalized to the number of pixels.

Figure A.2 shows the seismic and acoustic power as a function of field strength and inclination (similar to Figure 4.12). Each row represents a 36 minute average taken at three different times (6 hours apart): before, during and after the transit through the meridian. The distributions in each row are similar, indicating that it is a good approximation to analyse only 36 minutes of magnetic data at a time, in order to reduce error arising from solar evolution.

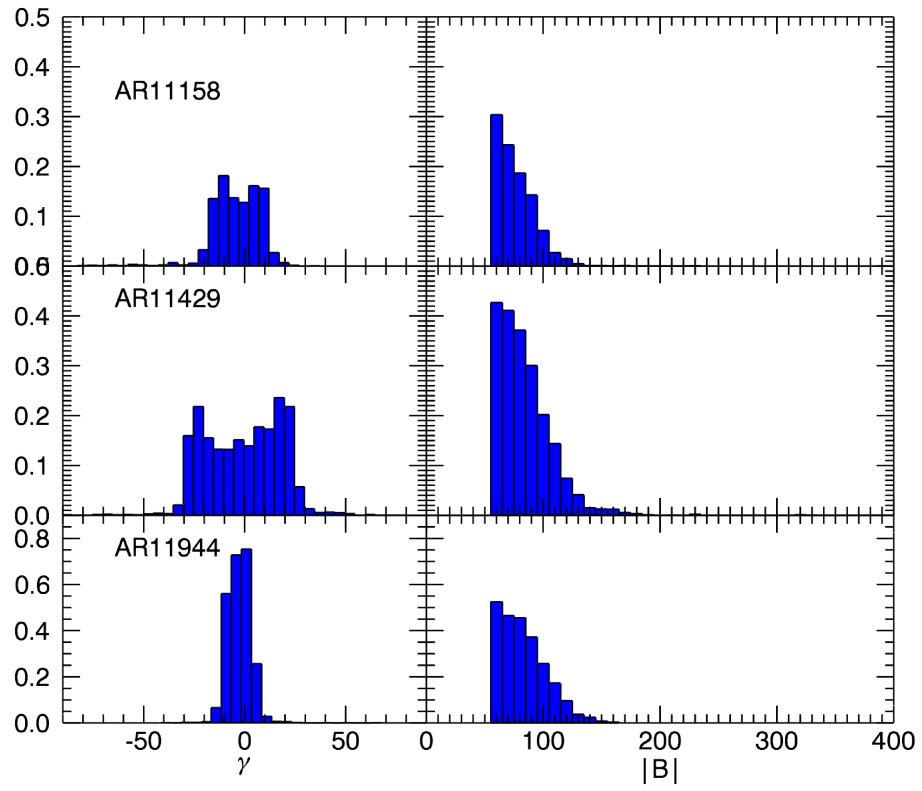


Figure A.1: Histogram plots of the magnetic morphology in the quiet-sun patches used to normalize each of the three active region's power maps.

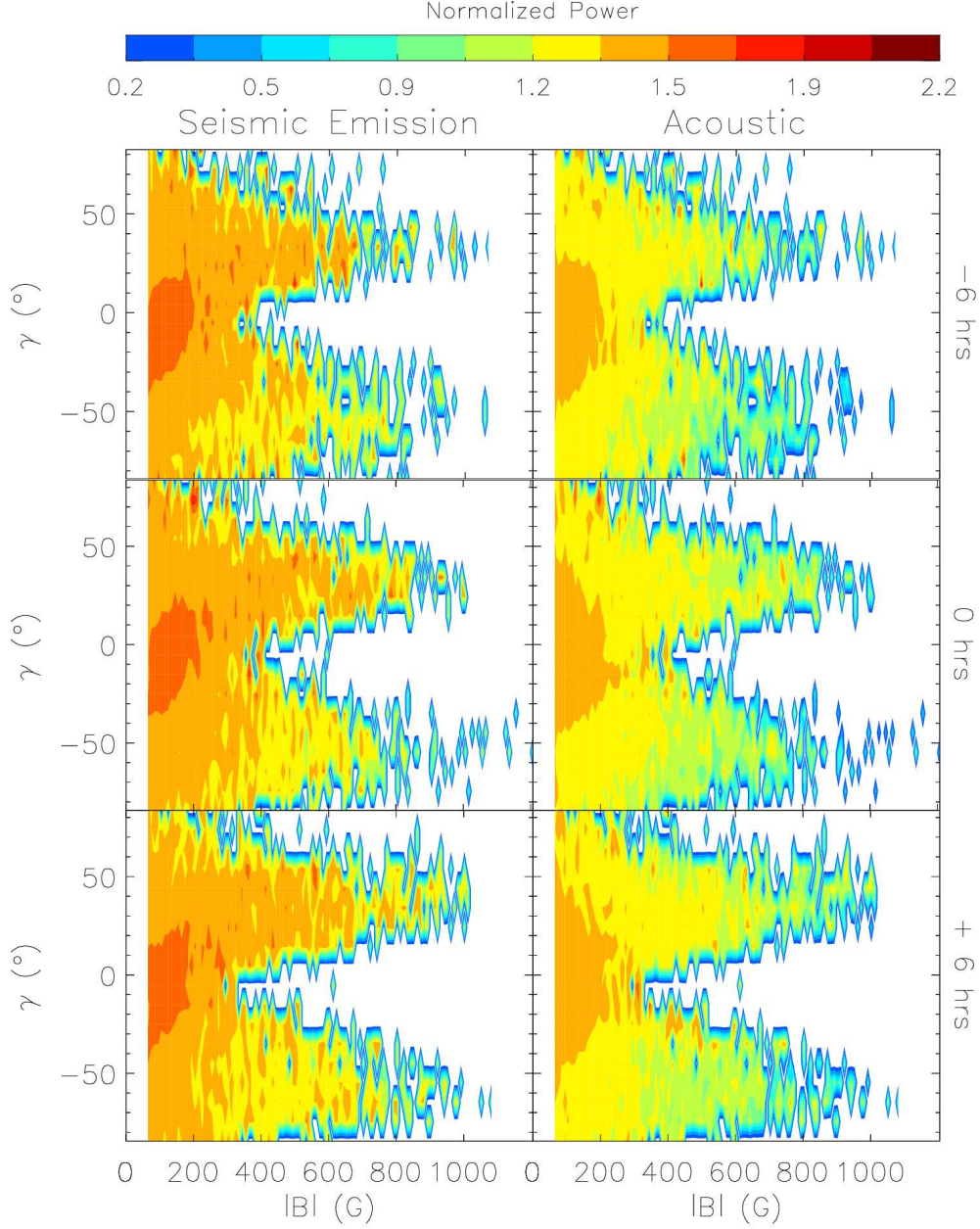


Figure A.2: The seismic emission and local acoustic power of the halo surrounding AR11429 at three times before, during and after the transit through the meridian.

Appendix B

Power as a Function of $|\mathbf{B}|$ and γ

In this Appendix, the power distributions as a function of magnetic field strength and inclination for AR11158 and AR11944 are presented. These figures are similar to figures 4.12 and 4.14, presented in Chapter 4. Figures B.1 and B.2, show the distributions for AR11158 over the entire region and halo, respectively. Likewise, Figures B.3 and B.4 show the distributions for AR11944's entire region and halo, respectively.

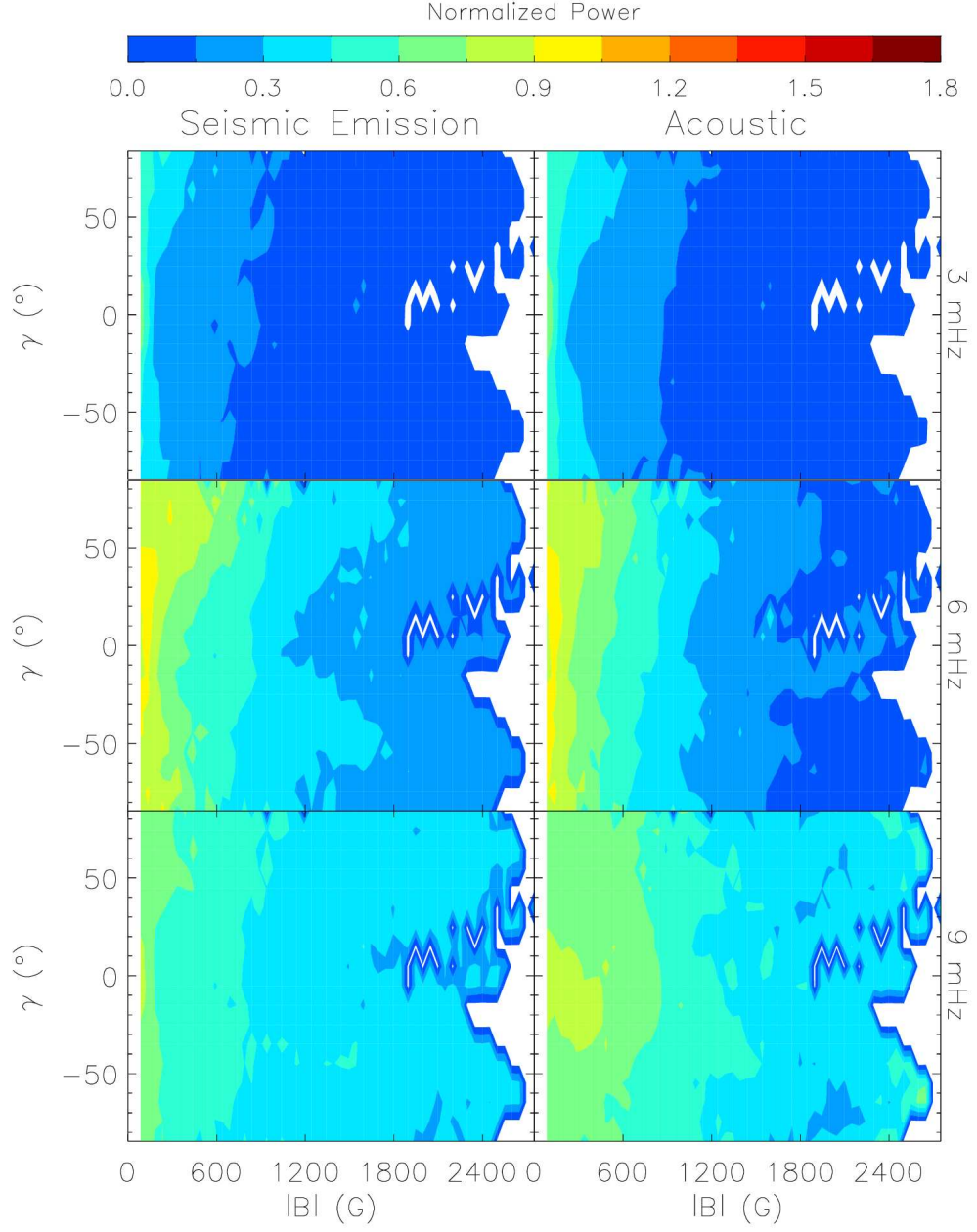


Figure B.1: The mean normalized power (in bins of 10 G and 10°) of the seismic emission (left) and local acoustic power (right), for the entire map of AR11158. Each row corresponds to the frequencies; 3,6 and 9 mHz from top to bottom, respectively.

APPENDIX B. POWER AS A FUNCTION OF
 $|\mathbf{B}|$ AND γ

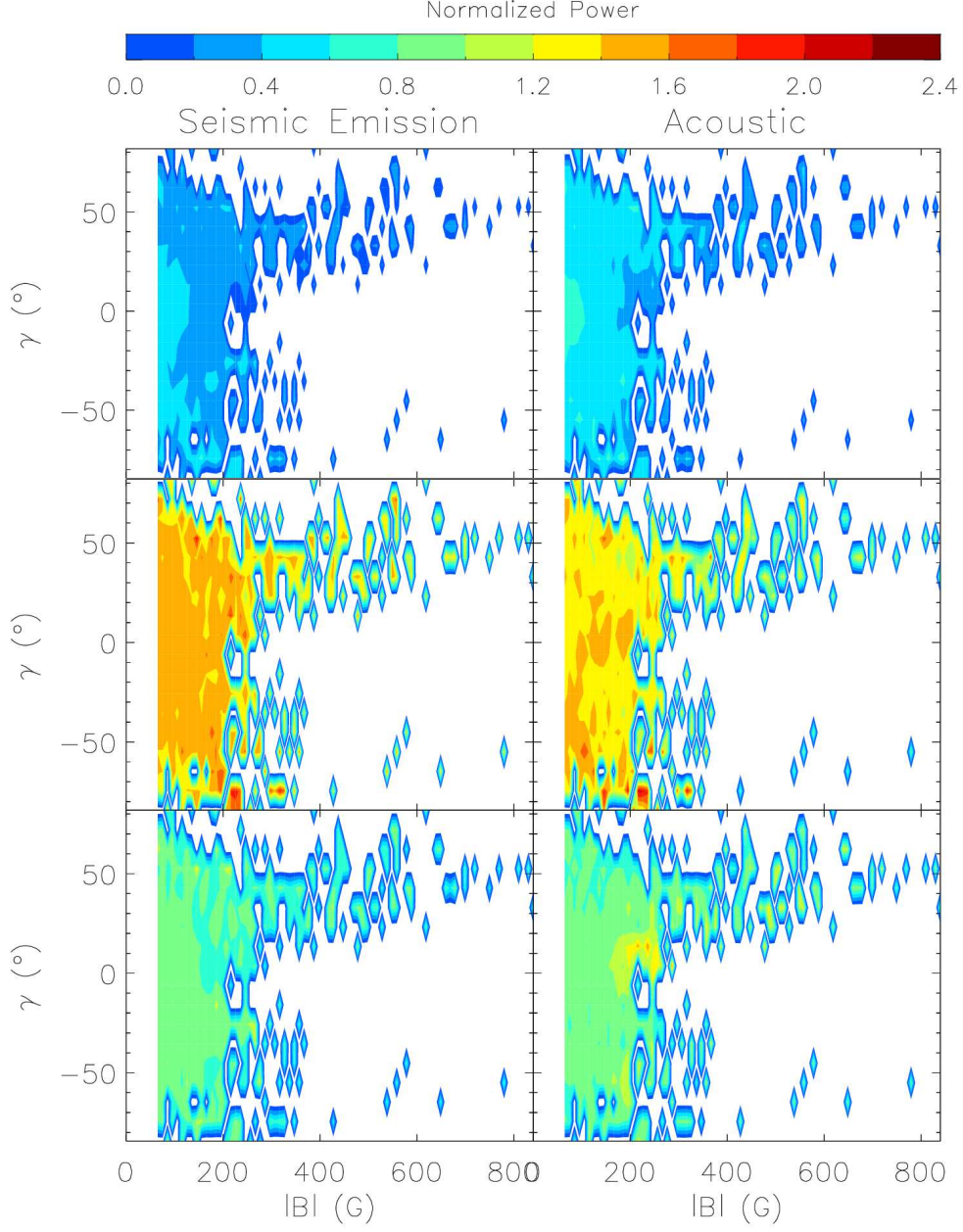


Figure B.2: The mean normalized power (in bins of 10 G and 10°) of the seismic emission (left) and local acoustic power (right), for the halo surrounding AR11158. Each row corresponds to the frequencies; 3, 6 and 9 mHz from top to bottom, respectively.

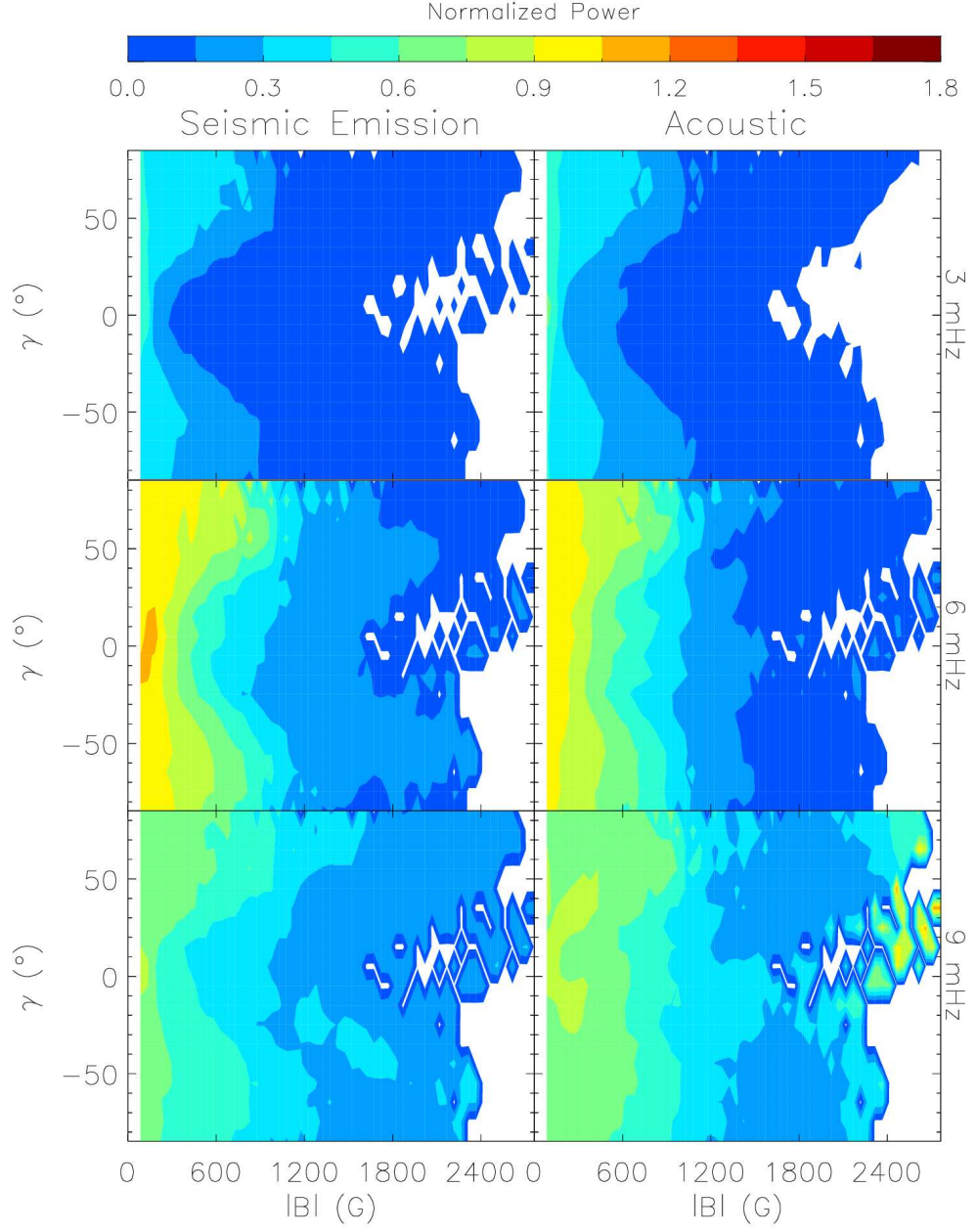


Figure B.3: The mean normalized power (in bins of 10 G and 10°) of the seismic emission (left) and local acoustic power (right), for the entire map of AR11944. Each row corresponds to the frequencies; 3,6 and 9 mHz from top to bottom, respectively.

APPENDIX B. POWER AS A FUNCTION OF
 $|\mathbf{B}|$ AND γ

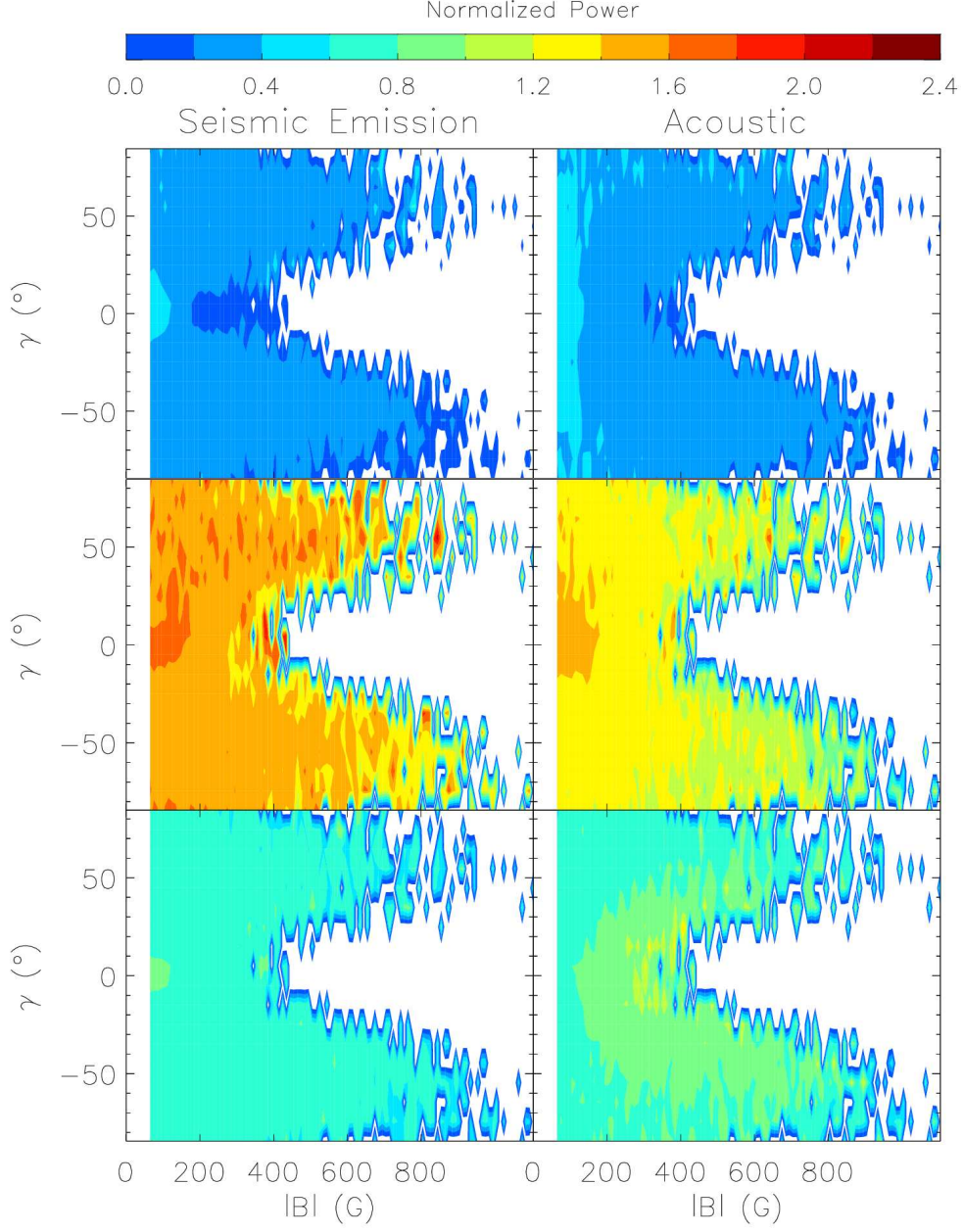


Figure B.4: The mean normalized power (in bins of 10 G and 10°) of the seismic emission (left) and local acoustic power (right), for the halo surrounding AR11944. Each row corresponds to the frequencies; 3,6 and 9 mHz from top to bottom, respectively.

Appendix C

Seismic and Local Acoustic Power maps at all Frequencies

In this Appendix the nature of the seismic and local acoustic power halos (for AR11429) for different frequencies will be shown, in order to illustrate the behaviour of the halo at different frequencies. In each Figure, 7 frames show 1 mHz bandwidth maps centred at frequencies between 2-10 mHz. The 8th frame (bottom right) shows the integrated power map for all frequencies.

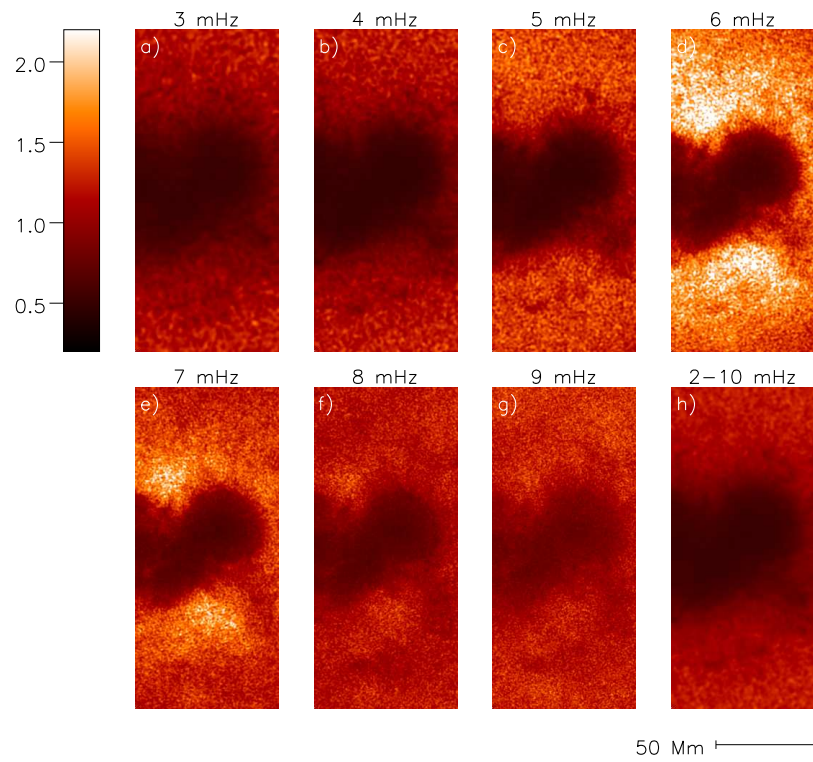


Figure C.1: A slice of the seismic emission power maps (AR11429) for different frequencies.

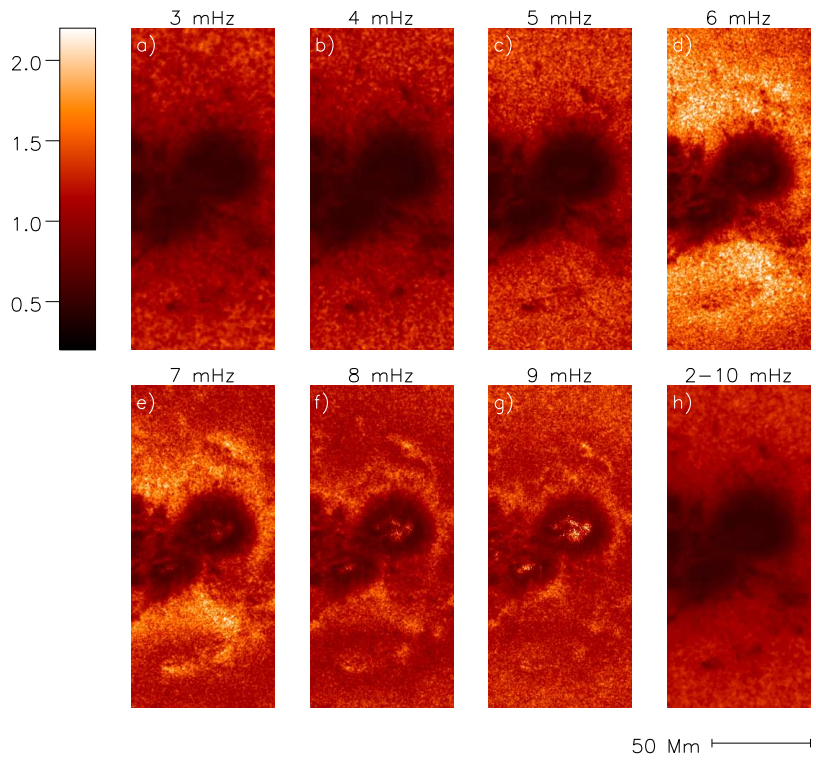


Figure C.2: A slice of the local acoustic power maps (AR11429) for different frequencies.

Chapter 6

Bibliography

- Abramowitz, M. and Stegun, I. A. (1964). *Handbook of mathematical functions*. National Bureau of Standards, Washington D.C., 2nd edition.
- Andries, J. and Cally, P. S. (2011). On the dispersion and scattering of magnetohydrodynamic waves by longitudinally stratified flux tubes. *ApJ*, 743(164):15.
- Barnes, G. and Cally, P. S. (2000). Mode mixing by a shallow sunspot. *Sol. Phys.*, 193:373–382.
- Bobra, M., Sun, X., Hoeksema, J., Turmon, M., Liu, Y., Hayashi, K., Barnes, G., and Leka, K. (2014). The helioseismic and magnetic imager (hmi) vector magnetic field pipeline: Sharps space-weather hmi active region patches. *Solar Physics*, 289(9):3549–3578.
- Bogdan, T. (1987a). Propagation of compressional waves through fibril magnetic fields ii. scattering from a slab of magnetic flux tubes. *ApJ*, 318:888–895.
- Bogdan, T. (1987b). Propagation of compressional waves through fibril magnetic fields iii. waves that propagate along the magnetic field. *ApJ*, 318:896–903.
- Bogdan, T. and Cally, P. (1995). Jacket modes: Solar acoustic oscillations confined to regions surrounding sunspots and plage. *ApJ*, 453:919–928.
- Bogdan, T. J., Brown, T. M., Lites, B. W., and Thomas, J. H. (1993). The absorption of p-modes by sunspots - variations with degree and order. *ApJ*, 406:723–734.

-
- Bogdan, T. J. and Fox, D. C. (1991). Multiple scattering of acoustic waves by a pair of uniformly magnetized flux tubes. *ApJ*, 379:758–775.
- Bogdan, T. J., Hindman, B. W., Cally, P. S., and Charbonneau, P. (1996). Absorption of p-modes by slender magnetic flux tubes and p-mode lifetimes. *ApJ*, 465:406.
- Bogdan, T. J. and Zweibel, E. G. (1985). Effect of a fibril magnetic field on solar p-modes. *ApJ*, 298:867–875.
- Bogdan, T. J. and Zweibel, E. G. (1987). Propagation of compressional waves through fibril magnetic fields. *ApJ*, 312:444–456.
- Borrero, J. M., Tomczyk, S., Kubo, M., Socas-Navarro, H., Schou, J., Couvidat, S., and Bogart, R. (2011). VFISV: Very Fast Inversion of the Stokes Vector for the Helioseismic and Magnetic Imager. *Sol. Phys.*, 273:267–293.
- Braun, D. C. (1995). Scattering of p-modes by sunspots. i. observations. *ApJ*, 451:859–876.
- Braun, D. C. and Birch, A. C. (2008). Surface-focused seismic holography of sunspots: I. observations. *Sol. Phys.*, 251:267–289.
- Braun, D. C., Duvall, Jr., T. L., and Labonte, B. J. (1987). Acoustic absorption by sunspots. *ApJ*, 319:L27–L31.
- Braun, D. C., Duvall, Jr., T. L., and Labonte, B. J. (1988). The absorption of high-degree p-mode oscillations in and around sunspots. *ApJ*, 335:1015–1025.
- Braun, D. C., Labonte, B. J., and Duvall, Jr., T. L. (1990). The spatial distribution of p-mode absorption in active regions. *ApJ*, 354:372–381.
- Braun, D. C. and Lindsey, C. (1999). Helioseismic Images of an Active Region Complex. *ApJ*, 513:L79–L82.
- Braun, D. C. and Lindsey, C. (2000a). Helioseismic Holography of Active-Region Subphotospheres - (Invited Review). *Sol. Phys.*, 192:285–305.
- Braun, D. C. and Lindsey, C. (2000b). Phase-sensitive Holography of Solar Activity. *Sol. Phys.*, 192:307–319.
- Braun, D. C. and Lindsey, C. (2001). Seismic Imaging of the Far Hemisphere of the Sun. *ApJ*, 560:L189–L192.

- Braun, D. C., Lindsey, C., Fan, Y., and Fagan, M. (1998). Seismic Holography of Solar Activity. *ApJ*, 502:968–980.
- Braun, D. C., Lindsey, C., Fan, Y., and Jefferies, S. M. (1992). Local acoustic diagnostics of the solar interior. *ApJ*, 392:739–745.
- Brown, T. M., Bogdan, T. J., Lites, B. W., and Thomas, J. H. (1992). Localized sources of propagating acoustic waves in the solar photosphere. *ApJ*, 394:L65–L68.
- Cally, P. S. (2006). Dispersion relations, rays and ray splitting in magneto-helioseismology. *Royal Society of London Philosophical Transactions Series A*, 364:333–349.
- Cally, P. S. (2013). Near- and far-field response to compact acoustic sources in stratified convection zones. *ApJ*, 768:35.
- Cally, P. S. and Bogdan, T. J. (1993). Solar p-modes in a vertical magnetic field - trapped and damped pi-modes. *ApJ*, 402:721–732.
- Centeno, R., Schou, J., Hayashi, K., Norton, A., Hoeksema, J. T., Liu, Y., Leka, K. D., and Barnes, G. (2014). The Helioseismic and Magnetic Imager (HMI) Vector Magnetic Field Pipeline: Optimization of the Spectral Line Inversion Code. *Sol. Phys.*, 289:3531–3547.
- Chandrasekhar, S. and Lebovitz, N. R. (1962). On the Oscillations and the Stability of Rotating Gaseous Masses. *ApJ*, 135:248.
- Chang, H.-K., Chou, D.-Y., Labonte, B., and TON Team (1997). Ambient acoustic imaging in helioseismology. *Nature*, 389:825–827.
- Chen, H.-R., Chou, D.-Y., Chang, H.-K., Sun, M.-T., Yeh, S.-J., LaBonte, B., and Team, t. T. (1998). Probing the Subsurface Structure of Active Regions with the Phase Information in Acoustic Imaging. *ApJ*, 501:L139–L144.
- Chou, D.-Y., Liang, Z.-C., Yang, M.-H., and Sun, M.-T. (2009). Acoustic-Power Maps of Solar Active Regions with Direction Filters and Phase-Velocity Filters. *Sol. Phys.*, 255:39–51.
- Crouch, A. D. and Cally, P. S. (1999). The contribution by thin magnetic flux tubes to p-mode line widths. *ApJ*, 521:878–884.

-
- Daifallah, K. (2014). Simulation of f-mode propagation through a cluster of small identical magnetic flux tubes. *Sol. Phys.*, 289:745–758.
- Daifallah, K., Abdelatif, T., Bendib, A., Cameron, R., and Gizon, L. (2011). 3D Numerical Simulations of f-Mode Propagation Through Magnetic Flux Tubes. *Sol. Phys.*, 268:309–320.
- Donea, A. and Newington, M. (2011). Stochastic seismic emission from acoustic glories in solar active regions. *JPCS.*, 271(1):012004.
- Donea, A.-C., Lindsey, C., and Braun, D. (2000). Stochastic seismic emission from acoustic glories and the quiet sun. *Sol. Phys.*, 192:321–333.
- Duvall, Jr., T. L., Birch, A. C., and Gizon, L. (2006). Direct measurement of travel-time kernels for helioseismology. *ApJ*, 646:553–559.
- Elmhamdi, A., Kordi, A. S., Al-Trabulsy, H. A., El-Nawawy, M., Ibrahim, A. A., Ben Nessib, N., Abdel-Sabour, M. A., and Al-Mostafa, Z. A. (2013). Observations and analysis of NOAA AR 11429 at KSU-Astronomical Observatory. *New A*, 23:73–81.
- Evans, J. W. and Michard, R. (1962). Observational Study of Macroscopic Inhomogeneities in the Solar Atmosphere. III. Vertical Oscillatory Motions in the Solar Photosphere. *ApJ*, 136:493.
- Felipe, T., Braun, D., Crouch, A., and Birch, A. (2012). Scattering of the f-mode by small magnetic flux elements from observations and numerical simulations. *ApJ*, 757:148.
- Felipe, T., Crouch, A., and Birch, A. (2013). Numerical simulations of multiple scattering of the f-mode by flux tubes. *ApJ*, 775:74.
- Fleck, B., Couvidat, S., and Straus, T. (2011). On the Formation Height of the SDO/HMI Fe 6173 Å Doppler Signal. *Sol. Phys.*, 271:27–40.
- Fossum, A. and Carlsson, M. (2005). Response Functions of the Ultraviolet Filters of TRACE and the Detectability of High-Frequency Acoustic Waves. *ApJ*, 625:556–562.
- Gary, G. A. and Hagyard, M. J. (1990). Transformation of vector magnetograms and the problems associated with the effects of perspective and the azimuthal ambiguity. *Sol. Phys.*, 126:21–36.

- Gascoyne, A., Jain, R., and Hindman, B. W. (2014). Energy Loss of Solar p Modes due to the Excitation of Magnetic Sausage Tube Waves: Importance of Coupling the Upper Atmosphere. *ApJ*, 789:109.
- Gizon, L. and Birch, A. C. (2005). Local helioseismology. *LRSP.*, 2:6.
- Gizon, L., Hanasoge, S., and Birch, A. C. (2006). Scattering of acoustic waves by a magnetic cylinder: Accuracy of the born approximation. *ApJ*, 643:549–555.
- Goedbloed, J. P. H. and Poedts, S. (2004). *Principles of Magnetohydrodynamics*.
- Goldreich, P. and Keeley, D. A. (1977). Solar seismology. II - The stochastic excitation of the solar p-modes by turbulent convection. *ApJ*, 212:243–251.
- Goossens, M., Soler, R., Terradas, J., Doorselaere, T. V., and Verth, G. (2014). The transverse and rotational motions of magnetohydrodynamic kink waves in the solar atmosphere. *ApJ*, 788(1):9.
- Hale, G. E. (1908). On the Probable Existence of a Magnetic Field in Sun-Spots. *ApJ*, 28:315.
- Hanasoge, S. M. (2008). Seismic halos around active regions: a magnetohydrodynamic theory. *ApJ*, 680:1457–1466.
- Hanasoge, S. M. (2009). A wave scattering theory of solar seismic power haloes. *A&A*, 503:595–599.
- Hanasoge, S. M., Birch, A. C., Bogdan, T. J., and Gizon, L. (2008). f-mode interactions with thin flux tubes: The scattering matrix. *ApJ*, 680:774–780.
- Hanasoge, S. M. and Cally, P. S. (2009). Multiple scattering of waves by a pair of gravitationally stratified flux tubes. *ApJ*, 697:651–659.
- Hanson, C. S. and Cally, P. S. (2014). An analytical approach to scattering between two thin magnetic flux tubes in a stratified atmosphere. *ApJ*, 781:125.
- Hanson, C. S. and Cally, P. S. (2014). The scattering of f- and p-modes from ensembles of thin magnetic flux tubes: An analytical approach. *ApJ*, 791(2):129.

-
- Harvey, J. W. (1969). *Magnetic Fields Associated with Solar Active-Region Prominences*. PhD thesis, UNIVERSITY OF COLORADO AT BOULDER.
- Hasan, S. S. (1997). The Linear Response of a Magnetic Flux Tube to Buffeting by External p-Modes. I. *ApJ*, 480:803–816.
- Hasan, S. S. and Bogdan, T. J. (1996). The effect of p-modes on thin magnetic flux tubes. *Bulletin of the Astronomical Society of India*, 24:125.
- Hindman, B. and Jain, R. (2012). Axisymmetric scattering of p modes by thin magnetic tubes. *ApJ*, 746(66):15.
- Hindman, B. W. and Brown, T. M. (1998). Acoustic Power Maps of Solar Active Regions. *ApJ*, 504:1029–1034.
- Hoeksema, J. T., Liu, Y., Hayashi, K., Sun, X., Schou, J., Couvidat, S., Norton, A., Bobra, M., Centeno, R., Leka, K. D., Barnes, G., and Turmon, M. (2014). The Helioseismic and Magnetic Imager (HMI) Vector Magnetic Field Pipeline: Overview and Performance. *Sol. Phys.*, 289:3483–3530.
- Jacoutot, L., Kosovichev, A. G., Wray, A. A., and Mansour, N. N. (2008). Numerical Simulation of Excitation of Solar Oscillation Modes for Different Turbulent Models. *ApJ*, 682:1386–1391.
- Jain, R., Gascoyne, A., and Hindman, B. W. (2011a). Axisymmetric absorption of p modes by an ensemble of thin, magnetic-flux tubes. *Journal of Physics Conference Series*, 271(1):012016.
- Jain, R., Gascoyne, A., and Hindman, B. W. (2011b). Interaction of p modes with a collection of thin magnetic tubes. *MNRAS*, 415:1276–1279.
- Jain, R., Hindman, B. W., Braun, D. C., and Birch, A. C. (2009). Absorption of p modes by thin magnetic flux tubes. *ApJ*, 695:325–335.
- Jiménez, A., García, R. A., and Pallé, P. L. (2011). The Acoustic Cutoff Frequency of the Sun and the Solar Magnetic Activity Cycle. *ApJ*, 743:99.
- Kagemoto, H. and Yue, D. K. (1986). Interactions among multiple three-dimensional bodies in water waves: an exact algebraic method. *J. Fluid Mech.*, 166:189–209.
- Keppens, R., Bogdan, T. J., and Goossens, M. (1994). Multiple scattering and resonant absorption of p-modes by fibril sunspots. *ApJ*, 436:372–389.

- Khomenko, E. and Collados, M. (2009). Sunspot seismic halos generated by fast mhd wave refraction. *A&A*, 506:L5–L8.
- Kitiashvili, I. N., Kosovichev, A. G., Wray, A. A., and Mansour, N. N. (2010). Mechanism of Spontaneous Formation of Stable Magnetic Structures on the Sun. *ApJ*, 719:307–312.
- Kosovichev, A. G. (2011). Helioseismic Response to the X2.2 Solar Flare of 2011 February 15. *ApJ*, 734:L15.
- Kuridze, D., Zaqarashvili, T. V., Shergelashvili, B. M., and Poedts, S. (2008). Acoustic oscillations in a field-free cavity under solar small-scale bipolar magnetic canopy. *Annales Geophysicae*, 26:2983–2989.
- Lamb, H. C. (1945). *Hydrodynamics*. New York: Dover.
- Leighton, R. B. (1959). Observations of Solar Magnetic Fields in Plage Regions. *ApJ*, 130:366.
- Leighton, R. B. (1963). The Solar Granulation. *ARA&A*, 1:19.
- Leighton, R. B., Noyes, R. W., and Simon, G. W. (1962). Velocity Fields in the Solar Atmosphere. I. Preliminary Report. *ApJ*, 135:474.
- Leka, K. D., Barnes, G., Crouch, A. D., Metcalf, T. R., Gary, G. A., Jing, J., and Liu, Y. (2009). Resolving the 180 Degree Ambiguity in Solar Vector Magnetic Field Data: Evaluating the Effects of Noise, Spatial Resolution, and Method Assumptions. *Sol. Phys.*, 260:83–108.
- Lemen, J. R., Title, A. M., Akin, D. J., Boerner, P. F., Chou, C., Drake, J. F., Duncan, D. W., Edwards, C. G., Friedlaender, F. M., Heyman, G. F., Hurlburt, N. E., Katz, N. L., Kushner, G. D., Levay, M., Lindgren, R. W., Mathur, D. P., McFeaters, E. L., Mitchell, S., Rehse, R. A., Schrijver, C. J., Springer, L. A., Stern, R. A., Tarbell, T. D., Wuelser, J.-P., Wolfson, C. J., Yanari, C., Bookbinder, J. A., Cheimets, P. N., Caldwell, D., Deluca, E. E., Gates, R., Golub, L., Park, S., Podgorski, W. A., Bush, R. I., Scherrer, P. H., Gummin, M. A., Smith, P., Auken, G., Jerram, P., Pool, P., Soufli, R., Windt, D. L., Beardsley, S., Clapp, M., Lang, J., and Waltham, N. (2012). The Atmospheric Imaging Assembly (AIA) on the Solar Dynamics Observatory (SDO). *Sol. Phys.*, 275:17–40.
- Lindsey, C. and Braun, D. (1997). Helioseismic holography. *ApJ*, 485:895–903.

-
- Lindsey, C. and Braun, D. C. (1990). Helioseismic imaging of sunspots at their antipodes. *Sol. Phys.*, 126:101–115.
- Lindsey, C. and Braun, D. C. (1998a). Acoustic Signatures of Subphotospheric Structure Underlying Sunspots. *ApJ*, 509:L129–L132.
- Lindsey, C. and Braun, D. C. (1998b). The Acoustic Moat and Thermal Transport in the Neighborhoods of Sunspots. *ApJ*, 499:L99–L102.
- Lindsey, C. and Braun, D. C. (2000a). Basic principles of solar acoustic holography - (invited review). *Sol. Phys.*, 192:261–284.
- Lindsey, C. and Braun, D. C. (2000b). Seismic images of the far side of the sun. *Sci*, 287:1799–1801.
- Lindsey, C. and Braun, D. C. (2005). The acoustic showerglass. i. seismic diagnostics of photospheric magnetic fields. *The Astrophysical Journal*, 620(2):1107.
- Lindsey, C., Braun, D. C., Jefferies, S. M., Woodard, M. F., Fan, Y., Gu, Y., and Redfield, S. (1996). Doppler Acoustic Diagnostics of Subsurface Solar Magnetic Structure. *ApJ*, 470:636.
- Lindsey, C. and Donea, A.-C. (2008). Mechanics of Seismic Emission from Solar Flares. *Sol. Phys.*, 251:627–639.
- Maltby, P., Avrett, E. H., Carlsson, M., Kjeldseth-Moe, O., Kurucz, R. L., and Loeser, R. (1986). A new sunspot umbral model and its variation with the solar cycle. *ApJ*, 306:284–303.
- McIntosh, P. S. (1981). The birth and evolution of sunspots - Observations. In Cram, L. E. and Thomas, J. H., editors, *The Physics of Sunspots*, pages 7–54.
- Metcalf, T. R. (1994). Resolving the 180-degree ambiguity in vector magnetic field measurements: The 'minimum' energy solution. *Sol. Phys.*, 155:235–242.
- Muglach, K., Hofmann, A., and Staude, J. (2005). Dynamics of solar active regions. II. Oscillations observed with MDI and their relation to the magnetic field topology. *A&A*, 437:1055–1060.

- Rajaguru, S. P., Couvidat, S., Sun, X., Hayashi, K., and Schunker, H. (2013). Properties of High-Frequency Wave Power Halos Around Active Regions: An Analysis of Multi-height Data from HMI and AIA Onboard SDO. *Sol. Phys.*, 287:107–127.
- Rijs, C., Moradi, H., Przybylski, D., and Cally, P. S. (2015). MHD wave refraction and the acoustic halo effect around solar active regions - a 3D study. *ApJ*, In Press.
- Ryutova, M. and Priest, E. (1993a). The propagation of sound waves in a randomly magnetized medium i. general considerations. *ApJ*, 419:349–370.
- Ryutova, M. and Priest, E. (1993b). The propagation of sound waves in a randomly magnetized medium ii. the interaction of an unsteady wave packet with an ensemble of magnetic flux tubes. *ApJ*, 419:371–381.
- Schou, J., Borrero, J. M., Norton, A. A., Tomczyk, S., Elmore, D., and Card, G. L. (2012a). Polarization Calibration of the Helioseismic and Magnetic Imager (HMI) onboard the Solar Dynamics Observatory (SDO). *Sol. Phys.*, 275:327–355.
- Schou, J., Scherrer, P. H., Bush, R. I., Wachter, R., Couvidat, S., Rabello-Soares, M. C., Bogart, R. S., Hoeksema, J. T., Liu, Y., Duvall, T. L., Akin, D. J., Allard, B. A., Miles, J. W., Rairden, R., Shine, R. A., Tarbell, T. D., Title, A. M., Wolfson, C. J., Elmore, D. F., Norton, A. A., and Tomczyk, S. (2012b). Design and Ground Calibration of the Helioseismic and Magnetic Imager (HMI) Instrument on the Solar Dynamics Observatory (SDO). *Sol. Phys.*, 275:229–259.
- Schunker, H. and Braun, D. C. (2011). Newly identified properties of surface acoustic power. *Sol. Phys.*, 268:349–362.
- Simon, G. W. and Leighton, R. B. (1964). Velocity Fields in the Solar Atmosphere. III. Large-Scale Motions, the Chromospheric Network, and Magnetic Fields. *ApJ*, 140:1120.
- Solanki, S. K. (2003). Sunspots: An overview. *A&A Rev.*, 11:153–286.
- Tirry, W. J. (2000). Absorption and scattering of trapped sound waves by nontrapped sausage and kink modes on slender magnetic flux tubes. *ApJ*, 528:493–508.

-
- Tobias, S. M. (2002). The solar dynamo. *Royal Society of London Philosophical Transactions Series A*, 360:2741–2756.
- Toner, C. G. and Labonte, B. J. (1993). Direct Mapping of Solar Acoustic Power. *ApJ*, 415:847.
- Turmon, M., Hoeksema, J. T., and Bobra, M. (2014). Tracked Active Region Patches for MDI and HMI. In *American Astronomical Society Meeting Abstracts 224*, volume 224 of *American Astronomical Society Meeting Abstracts*, page 123.52.
- Unno, W., Osaki, Y., Ando, H., Saio, H., and Shibahashi, H. (1989). *Non-radial oscillations of stars*.
- Weiss, N. O. and Tobias, S. M. (2000). Physical Causes of Solar Activity. *Space Sci. Rev.*, 94:99–112.
- Wiegelmann, T., Lagg, A., Solanki, S. K., Inhester, B., and Woch, J. (2005). Comparing magnetic field extrapolations with measurements of magnetic loops. *A&A*, 433:701–705.
- Woods, T. N., Eparvier, F. G., Hock, R., Jones, A. R., Woodraska, D., Judge, D., Didkovsky, L., Lean, J., Mariska, J., Warren, H., McMullin, D., Chamberlin, P., Berthiaume, G., Bailey, S., Fuller-Rowell, T., Sojka, J., Tobiska, W. K., and Viereck, R. (2012). Extreme Ultraviolet Variability Experiment (EVE) on the Solar Dynamics Observatory (SDO): Overview of Science Objectives, Instrument Design, Data Products, and Model Developments. *Sol. Phys.*, 275:115–143.
- Zhao, H. and Chou, D.-Y. (2013). Mode conversion between different radial orders for solar acoustic waves scattered by sunspots. *ApJ*, 778:4.
- Zharkov, S., Green, L. M., Matthews, S. A., and Zharkova, V. V. (2011). 2011 February 15: Sunquakes Produced by Flux Rope Eruption. *ApJ*, 741:L35.
- Zharkov, S., Shelyag, S., Fedun, V., Erdélyi, R., and Thompson, M. J. (2013). Photospheric high-frequency acoustic power excess in sunspot umbra: signature of magneto-acoustic modes. *Annales Geophysicae*, 31:1357–1364.
- Zwaan, C. (1978). On the Appearance of Magnetic Flux in the Solar Photosphere. *Sol. Phys.*, 60:213–240.